Chapter 1

Introduction

The Earth is one of the magnetized planets. In the absence of any external drivers, the geomagnetic field can be approximated by a dipole field with an axis tilted about 11 degrees from the rotation axis. The forcing by the solar wind is able to modify this field, creating a cavity called the magnetosphere. This cavity shelters the surface of the planet from the high energy particles of the solar wind. The outer boundary of the magnetosphere is called the magnetopause. In front of the dayside magnetopause a shock is produced as the supersonic solar wind encounters the Earth as an obstacle hits flow. This shock is called the bow shock, and the region between the bow shock and the magnetopause is called the magnetosheath. These regions are depicted in Figure 1-1. The processes by which energy and momentum are transferred from the solar wind into the Earth's magnetosphere are still one of the most important subjects of investigations in space plasma physics.

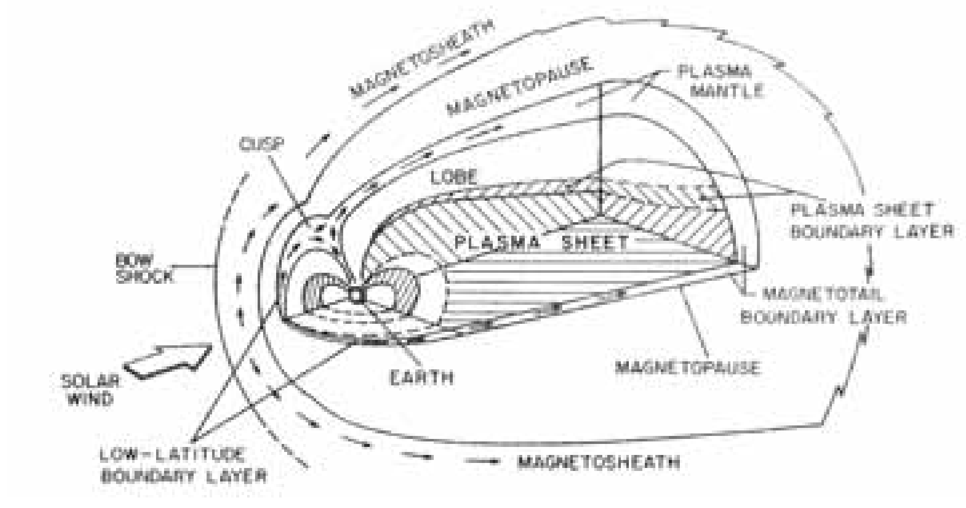

Figure 1-1. The Earth's magnetosphere [from *Eastman et al.*,1984].

1.1 Magnetic impulse events (MIEs)

The interaction of the solar wind plasma with the Earth's magnetic field causes different types of geomagnetic field variations. Among them, magnetic impulse events (MIEs), with amplitudes ranging from several tens to several hundreds of nT and durations ranging from 5 to 20 min, are prominent signatures of ground-based magnetometers in dayside cusp latitude [e.g., *Lanzerotti et al.*, 1991]. An example of MIEs is shown in Figure 1-2. MIEs have been considered as a product from the transient response of the magnetosphere to various kinds of solar wind variations. However, the generation mechanism of MIEs is still in controversy.

Two important early studies of the MIEs are those by *Lanzerotti et al.* [1986] and *Friis-Christensen et al.* [1988]. *Lanzerotti et al.* [1986] showed that MIEs could be interpreted as a possible ground signature of flux transfer events (FTEs) produced by bursty merging at the magnetopause [*Russel and Elphic*, 1978]. Since FTEs have been invoked to explain the vast majority of the solar wind-magnetosphere interaction, this was the pioneering suggestion for investigating MIEs with great importance. Subsequently, using dense arrays of ground-based magnetometers, *Friis-Christensen et al.* [1988] showed that some MIEs could be interpreted in terms of traveling convection vortices (TCVs) moving anti-sunward from the midday sector (cf., Figure 1-3). The propagation velocity and the scale size of TCVs were shown to be inconsistent with the prediction of FTEs and probably caused by sudden changes in the solar wind pressure and/or the interplanetary magnetic field (IMF). The conception of TCVs has become essential to understand the latitudinal and longitudinal extension of MIEs. Actually, many of MIEs are accompanied by the TCVs.

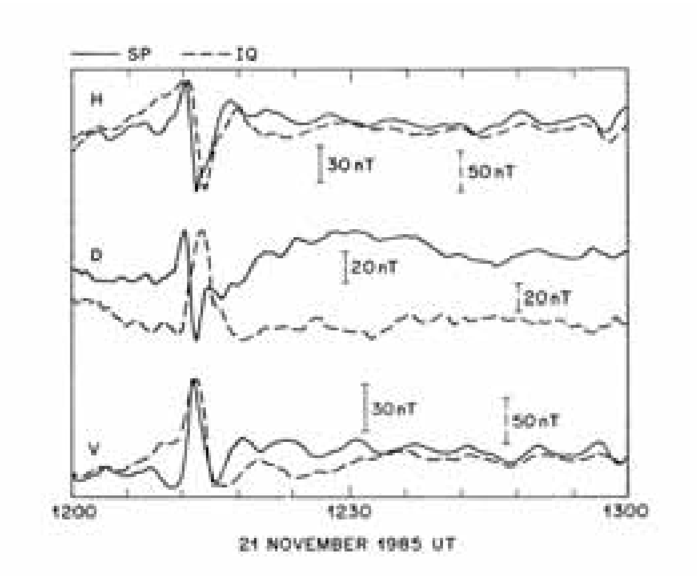

Figure 1-2. Example of magnetic impulse events (MIEs) measured at Iqualuit and South Pole [from *Lanzerotti et al.*, 1991].

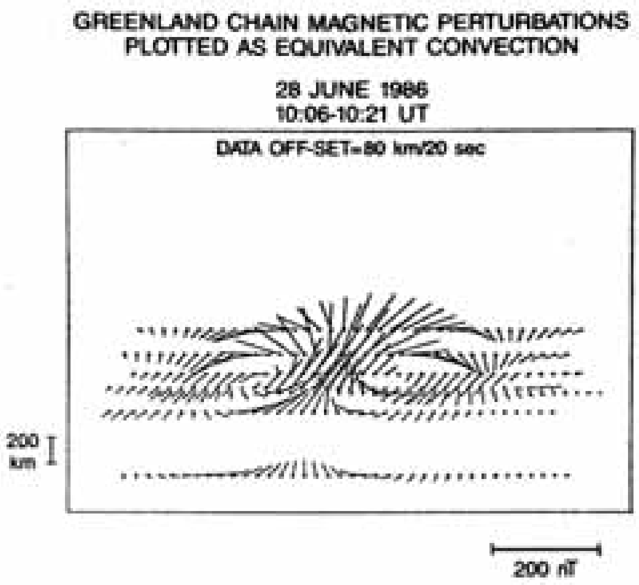

Figure 1-3. Example of TCVs observed at Greenland magnetometer chain stations. Total horizontal magnetic perturbation vectors have been rotated by 90° counterclockwise and are plotted every 20 seconds during interval from 1006 to 1021 UT [from *Friis-Christensen et al.*, 1988].

Thereafter, case and statistical studies suggested a wide variety of possible causes for the MIEs, including conventional models such as variations in the solar wind dynamic pressure [*Tamao*, 1964], bursty merging at the magnetopause [*Glassmeier et al.*, 1984], Kelvin-Helmholtz instability [*McHenry et al.*, 1988], and impulsive solar wind plasma penetration [*Heikkila et al.*, 1989]. Recently, more complicated models have been proposed: reconnection induced by Kelvin-Helmholtz instability [*Konik et al.*, 1994], modulation of the solar wind pressure by changes in the IMF orientation [*Sibeck and Korotova*, 1996], and gross deformation of the magnetopause due to hot flow anomaly produced by solar wind discontinuity [*Sitar et al.*, 1998].

Pressure Pulse

Abrupt variations in the solar wind dynamic pressure applied to the dayside magnetopause can generate impulsive events in the outer dayside magnetopause. MIEs are often observed as twin convection vortex patterns elongated in the east-west direction with scales of about 1000 km in the ionosphere. These events could be interpreted as movement of a pair of field-aligned currents [*Glassmeier et al.*, 1989]. Figure 1-4 shows an illustration explaining the twin vortex current system produced by the pressure pulse mechanism. The velocity and the scale size of these TCVs could be explained with the localized surface wave on the magnetopause caused by sudden solar wind dynamic pressure variations [e.g., *Sibeck*, 1990].

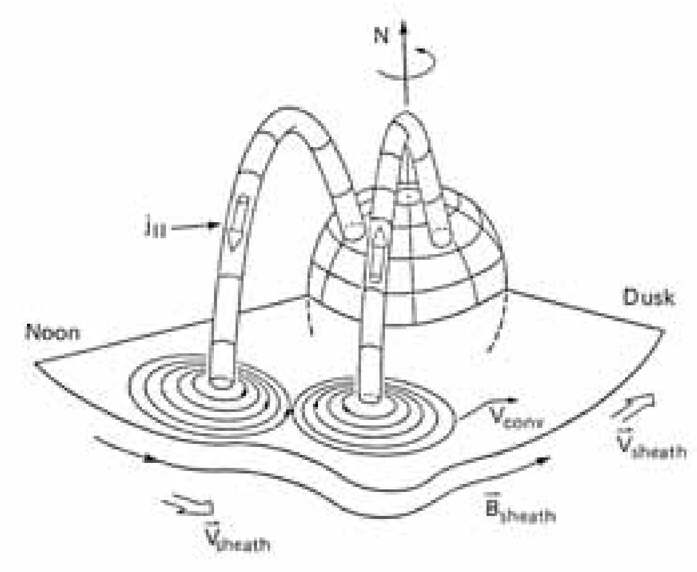

Figure 1-4. Twin vortex convection pattern at the magnetopause caused by the solar wind pressure pulse and its connection to a pair of antiparallel field-aligned currents. The entire pattern moves antisunward with magnetosheath flow velocities [from *Sibeck*, 1990].

However, statistical approaches indicated that most MIEs occur in the absence of any significant changes (dP/P > 1) in the solar wind dynamic pressure [e.g. *Bering et al.*, 1990; *Lin et al.*, 1995; *Konik et al.*, 1995; *Sibeck and Korotova*, 1996; *Vorobjev et al.*, 1999]. It is speculated that the pressure pulse mechanism is not the dominant generation mechanism of MIEs.

Bursty merging

From the theoretical approach, it was shown that bursty merging along one or more merging lines on the dayside magnetopause could produce impulsive magnetic features in the outer dayside magnetosphere [e.g., *Lee and Fu*, 1985]. Since the direction of the magnetic field at the low latitude magnetopause is points northward, the impulsive events would occur mostly during periods of southward IMF orientation [e.g*.,* *Le et al.*, 1993]. *Lockwood et al.* [1989] suggested that southward IMF turnings may trigger bursty merging. *Bering et al.* [1990] and *Lin et al.* [1995] used an event selection for MIEs with much smaller magnetic amplitudes than was used by *Lanzerotti et al.* [1991], and found a tendency for MIEs to occur during periods of southward IMF. *Konik et al.* [1995] concluded that the nonconjugate trends are consistent with the effect expected from the magnetic tension of reconnected field lines. Nevertheless, many MIEs were found to occur during periods of northward IMF [e.g., *Friis-Christensen et al.*, 1988; *Bering et al.*, 1990; *Lin et al.*, 1995; *Konik et al.*, 1995; *Sibeck and Korotova*, 1996; *Vorobjev et al.* 1999]. In addition the bursty merging theory has other critical problems. For example, most of the TCVs move antisunward with speeds in a range of 3-6 km/sec. This velocity is much higher than that expected for FTEs with velocities of 0.5-1.0 km/sec mapped on the ionosphere. Since FTEs should be associated with mass motion at the ionospheric foot point of the reconnected flux tube, their velocities should not exceed the ionospheric sound speed [*Farrugia et al.*, 1989].

Kelvin-Helmholtz instability

Large velocity shears perpendicular to the magnetosheath magnetic field favor the Kelvin-Helmholtz instability at the magnetopause [e.g., *Southwood*, 1968]. This condition is most likely met on the flanks of the magnetosphere during periods of high solar wind velocity and strongly northward or southward IMF orientation. During periods of strongly southward IMF orientation, the low latitude boundary layer (LLBL) becomes thin and flow in this region is accelerated by reconnection process. Therefore the Kelvin-Helmholtz instability becomes more likely during periods of southward IMF orientation [e.g. *Sibeck*, 1994]. The interpretation in terms of Kelvin-Helmholtz instability is inconsistent with statistical characteristics, showing no tendency of MIEs to occur during periods of strongly southward IMF orientation or enhanced solar wind velocities [*Konik et al.*, 1995; *Sibeck and Korotova*, 1996; *Vorobjev et al.*, 1999]. *McHenry et al.* [1990a, 1990b] suggested that the multiple convection vortex system related to Pc 5 pulsations is likely to be generated by the Kelvin-Helmholtz instability in the LLBL. Today, these events are considered to be different events as 'continuous TCVs' from the MIE-related TCVs as 'impulsive TCVs' though many features of both types of TCVs seem to be very similar.

Impulsive penetration

Impulsive solar wind plasma penetration is posited based upon the existence of filamentary solar wind structures with scale sizes of the order of 1 Re that reach, and penetrate, the magnetopause with enhanced momentum [*Lemaire*, 1977]. Figure 1-5 shows a schematic view of the impulsive penetration model and its comparison with the FTE model [*Heikkila et al.*, 1989]. *Woch and Lundin*, [1992] showed that the plasma penetration events have same MLT dependence on the dawnside magnetosphere as for MIEs. Moreover, the proposed connection of injection events to plasma clouds in the boundary layer offers a straightforward explanation for the double vortex structure of the MIE, attributed to traveling pairs of oppositely directed field-aligned currents [*Woch and Lundin*, 1992]. Even if the event characteristics may be consistent with those models of the impulsive penetration, we must reserve judgment concerning its ability to produce the observed events because there is no observational backing that indicates solar wind scale lengths as small as 1 Re yet.

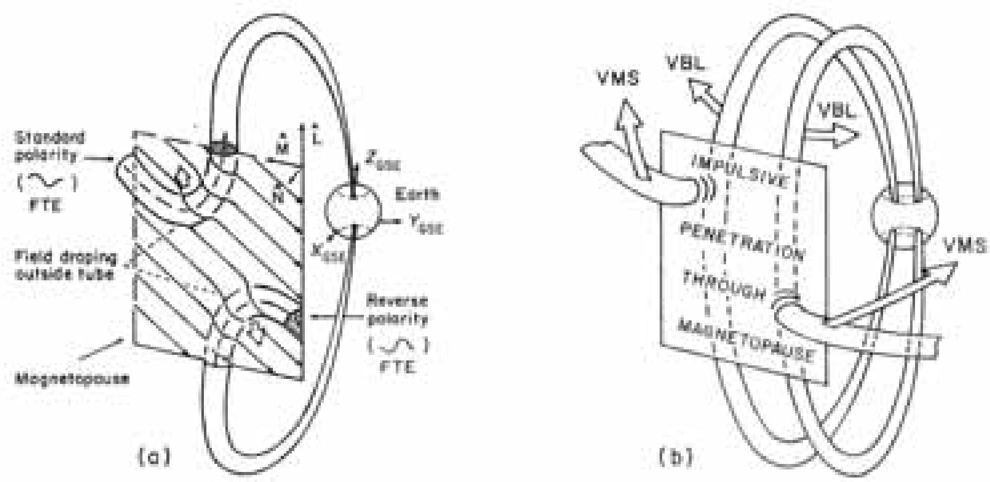

Figure 1-5. Schematic view of the FTE model (a) and the impulsive penetration model (b) [from *Heikkila et al.*, 1989]. (a) With a localized burst of recconection at the magnetopause the reconnected flux tubes (north as well as south) map to the equatorward edge of open field lines in the polar caps, corresponding to an equatorward bulge in the boundary between open and closed field line. (b). With impulsive penetration of solar wind plasma through the magnetopause onto closed field lines, two separate disturbances result on closed field lines on the morning side as well as on the afternoon side.

Other models

Konik et al. [1994] suggested that the Kelvin-Helmholtz instability may mediate the process by which sporadic reconnection produces MIEs. The hints for this idea are the fact that magnetic reconnection is likely responsible for generating a minimum of 50%-70% to a maximum of 90% of the events and that he local time dependence of unipolar deflections in the vertical component could be explained by postulating that the MIEs are associated with vortices generated by Kelvin-Helmholtz instability in the LLBL. Although theoretical support for this mechanism exists [*Uberoi et al.*, 1996, 1999], there are no critical event studies for confirming this mechanism.

Sibeck and Korotova [1996] suggested an interpretation of MIEs in terms of a model in which changes in the IMF orientation modulate the fraction of the solar wind pressure applied to the magnetopause. For example, MHD and hybrid simulations by *Lin et al.* [1996] showed that the interaction between the bow shock and interplanetary rotational discontinuity, Alfvén wave pulse, or Alfvén wave could produce the pressure pulse in the down stream of the bow shock (cf., Figure 1-6). *Vorobjev et al.* [1999] also concluded from their statistical study that MIEs were caused generally by solar wind dynamic pressure variations with increases in amplitude from 20 to 140% because those pressure impulses may be amplified by a factor of 2 by the simultaneous change of the foreshock geometry caused by abrupt IMF cone angle changes from <30° to >30°.

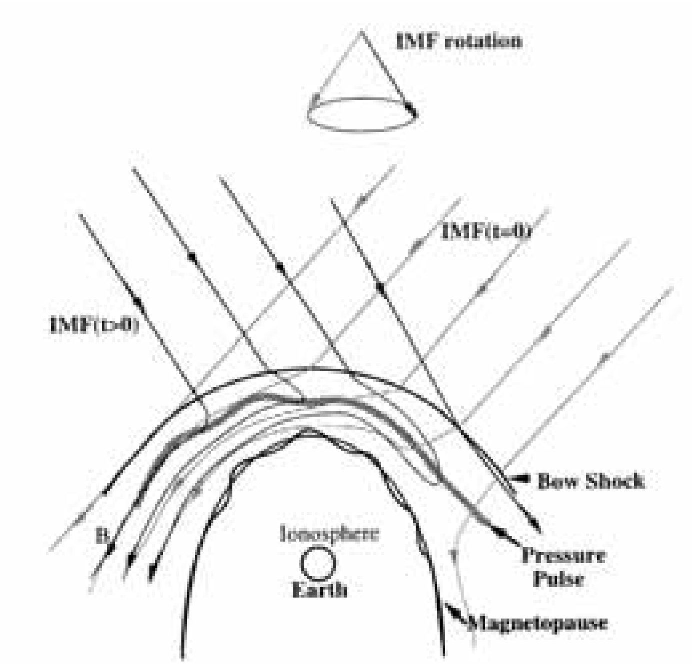

Figure 1-6. A schematic sketch for the generation of a dynamic pressure pulse in the magnetosheath by a variation of the interplanetary magnetic field (IMF) orientation. Note that the dynamic pressure pulse (shaded area) is a transient phenomenon [from *Lin et al.*, 1996].

More recently, the three-dimensional global magnetohydrodynamic simulation by *Chen et al.* [2000] showed that a fast mode wave and a transmitted tangential discontinuity produce TCVs. These pressure pulses are generated in the magnetosheath by the interaction between the interplanetary tangential discontinuity and the bow shock.

It has also been suggested that a hot flow anomalies (HFAs), produced by the interaction of certain tangential discontinuities with the bow shock, are the mechanism through which IMF discontinuities can produce MIEs [*Sitar et al.,* 1998; *Sibeck et al.*, 1998, 1999]. Numerical simulations of HFAs were also carried out [*Lin,* 1997; *Cable and Lin*, 1998]. However, *Sitar and Clauer* [1999] showed that the occurrences of ground signatures appear to be weakly related to the conditions necessary to produce HFAs [*Sitar and Clauer*, 1999].

As mentioned above, there are many proposed mechanism of the MIEs but none of them are conclusive, although the connection of MIEs to the solar wind-magnetosphere interaction processes is undoubted. The investigations of the transient phenomena in the magnetosphere and ionosphere have become important more and more in last decade to the transient phenomena in the magnetosphere and ionosphere. If we succeed in illuminating the generation mechanisms of MIEs, we will be able to use high-latitude ground magnetometer data for remote sensing of the solar wind-magnetosphere interaction processes.

1.2 Purpose of this thesis

As described in the previous section, the investigation of MIEs is one of the most important topics in the last decade in the study of the transient response of the magnetosphere to solar wind variations. The purpose of this thesis is to reveal the generation mechanisms of MIEs by analyzing the omnivorous data sets from space and ground based observations, particularly using the data obtained from the Automatic Geophysical Observatory (AGO) network covering the cusp, LLBL, and polar cap region in Antarctica. The AGO network consists of six vacant geophysical sites coded as P1, P2, P3, P4, P5, and P6. At each AGO site a suite of six instruments (optical aurora imager, imaging riometer, fluxgate and search-coil magnetometers, narrow- and wide-band ELF-VLF receiver, and HF receiver) are installed [*Rosenberg*, 1995]. This thesis is focused on the investigations of the dynamic behaviors of MIEs in the northern and southern polar regions and related auroral activity. Since 1995, numerous magnetometers have been installed in the northern and the southern polar region, including AGOs. However, the dynamical relationship between MIEs in the northern and southern polar regions is still unknown. The study on the conjugacy of MIEs would provide a clue to the generation mechanisms of MIEs. Further, optical signature of MIEs. Since optical signatures provide detailed spatial and temporal evolution of the particle precipitation and current system related to MIEs. The characteristic optical signatures related to MIEs have been investigated using ground based all-sky imagers [e.g., *Fukunishi and Lanzerotti*, 1989; *Mende et al.*, 1990; *Vorobjev et al*, 1994; *Lühr et al*, 1996; *Weatherwax et al*, 1999; *Sitar et al.*, 1998]. However, MIEs propagate over a long distance, at least more than 1000 km which is the limit of a field-of-view of one all-sky imager. The all-sky imager network of AGOs makes it possible to trace the propagation of MIE-related aurora over such a long distance.

Chapter 2 describes the system description of AGO network and procedures of the magnetic field, all-sky image, and interplanetary data analysis. A case study of a MIE on June 6, 1997 is shown in Chapter 3. The result of conjugate analysis using magnetometer network data in northern and southern high latitudes was reported for the first time in this thesis. The analysis of simultaneous observation data of aurora, CNA, and HF backscatter was also performed at first as to the motion of traveling convection vortex (TCV) accompanied by the MIE. A multi event analysis of MIEs is executed in Chapter 4. The conjugacy, related auroral activities, and solar wind sources of MIEs are discussed. Finally, summary and conclusions of this thesis are presented in Chapter 5.

Chapter 2

Instrumentations and data analysis

2.1 Automatic geophysical observatories (AGOs)

In order to reveal the mechanisms through which solar wind energy transfers into the magnetosphere, it is necessary to investigate the phenomena associated with dayside polar magnetospheric regions such as the cusp, low latitude boundary layer, and plasma mantle. These regions are mapped in very high (more than 70°) geomagnetic latitudes. Since the region above 80° geomagnetic latitude in the northern hemisphere lies mostly in the Arctic Ocean, it is practical only in Antarctica to set up multiple ground-based facilities that provide the whole coverage of the polar upper atmosphere at such high latitudes. It is essential to know the electrodynamics of the high latitude region and the key roles which play in coupling the solar wind with the Earth's magnetosphere, ionosphere, and thermosphere in order to make progresses in understanding the Sun's influence on the structure and dynamics of the Earth's upper atmosphere. Measurements that are central to understanding it include the electric field convection pattern across the polar cap and knowledge of the response of the atmosphere to the many forms of high-latitude wave and particle energy inputs during both geomagnetically quiet and disturbed situations [*Rosenberg*, 1995].

Automatic Geophysical Observatories (AGOs) are the first large-scale network stations in Antarctica. The overall objective of AGOs is to relate these measurements to relevant physical processes, to the source regions that produce the observed phenomena, and to the responsible drivers [*Rosenberg*, 1995]. There are six unmanned stations named P1, P2, P3, P4, P5, and P6 in the AGO network. A suite of nearly identical instruments (optical aurora imager, imaging riometer, fluxgate and search-coil magnetometers, narrow- and wide-band ELF-VLF receiver, and HF receiver) was installed at each station. These instruments and the science teams are listed in Table 2-1. The locations of AGOs and several key stations are shown in Figure 2-1. Figure 2-2 shows the HF radar coverage and the conjugate projection of sites in Greenland and Canada to Antarctica using the *Gustafsson et al.*, [1992] corrected geomagnetic coordinate system. Table 2-2 gives the coordinates of AGO network and manned SP, MM stations. The AGO sites are chosen to form two arrays along geomagnetic meridian. The first array (P2, SP, P1, P5, and P6) including manned South Pole station stretches from the slightly lower latitude of the nominal polar cusp through the pole of the dipole magnetic field between P5 and P6. The second meridional array (P3, P4, P5, and P6) is suited about 1.6 hours earlier in magnetic local time to allow comparative observations between temporal and spatial effects in the polar cap. The AGOs at P1 and P4, together with manned stations McMurdo station provide a longitudinally spaced array at 80° geomagnetic latitude to give the coverage over an extended range of magnetic local time. In this study, we used data obtained from observations of imaging riometers, fluxgate magnetometers, search-coil magnetometers, and all-sky auroral imagers.

Table 2-1. AGOs science team.

Instrument	Institution	Investigators
Imaging Riometer	University of Maryland at College Park	T. J. Rosenberg
		A. T. Weatherwax
Fluxgate Magnetometer	Bell Laboratories, Lucent Technologies	L. J. Lanzerotti
		C. G. Maclennan
Search-coil Magnetometer	Tohoku University	H. Fukunishi
	Augsburg College	M. J. Engebretson
	University of New Hampshire	R. L. Arnoldy
All-sky Auroral Imager	University of Carifornia at Berkeley	S. B. Mende
		H. U. Frey
	Lockeed Martin Advanced Technology Center	J. H. Doolittle
ELF/VLF Radio Receiver	Stanford University	U. S. Inan
LF/HF Radio Receiver	Dartmouth College	J. LaBelle

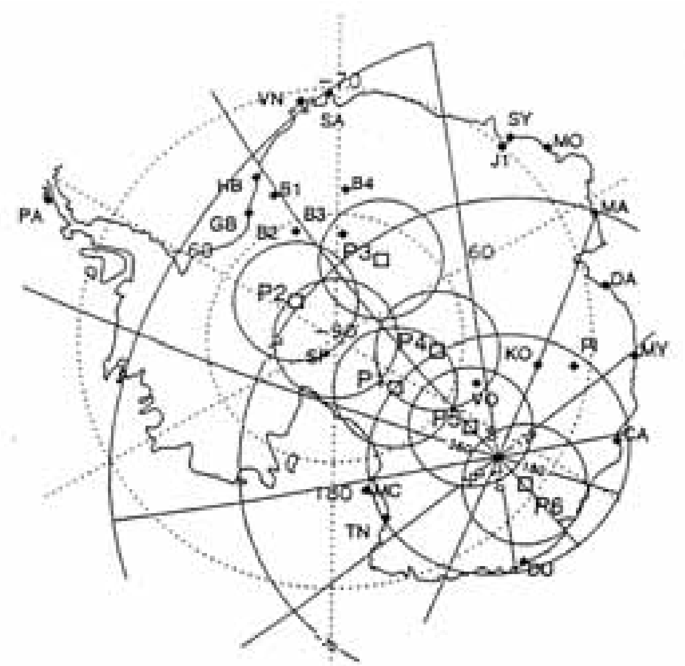

Figure 2-1. Antarctic observation sites. Geographic (geomagnetic) coordinates are given by the dotted (solid) lines. The 500-km radius circles around the AGO sites P1-P6 and South Pole (SP) approximate the field of view at 200 km altitude of a 630 nm auroral imager. [from *Rosenberg*, 1995].

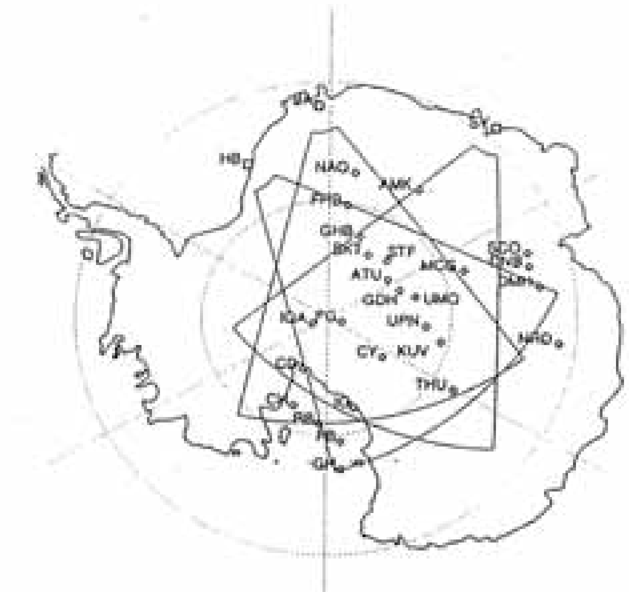

Figure 2-2. Conjugate mapping of northern hemisphere sites in Greenland and Canada. The overlapping fields of view of HF radars at Halley (HB), Sanae (SA), and Syowa (SY) are also shown [from *Rosenberg*, 1995].

Table 2-2. AGO sites and manned Antarctic stations. Corrected geomagnetic (CGM) coordinates at 100 km altitude was calculated for year 1997. CGM south pole located at (S 74.15, E 126.14).

Station	Geographic		Corrected Geomagnetic		UT-MLT
	Latitude	Longitude	Latitude	Longitude	
P1 (Jan 1994)	S 83.86	E 129.61	S 80.14	E 16.87	3:44
P2 (Dec 1992)	S 85.67	E 313.62	S 69.84	E 19.33	3:29
P3 (Jan 1995)	S 82.75	E 28.59	S 71.80	E 40.25	2:02
P4 (Jan 1994)	S 82.01	E 96.76	S 80.00	E 41.64	1:59
P5 (Jan 1996)	S 77.24	E 123.52	S 86.74	E 29.46	2:52
P6 (Jan 1997)	S 69.51	E 130.03	S 84.92	E 215.39	14:26
South Pole	S 90.00	E 000.00	S 74.02	E 18.35	3:35
McMurdo	S 77.85	E 166.67	S 79.94	E 326.97	6:57

Imaging riometer

A riometer (Relative ionospheric opacity meter) is an instrument that measures the opacity of the earth's atmosphere to cosmic radio noise, which is used as a monitor of cosmic noise absorption (CNA) related to small changes in the electron density of the ionosphere. The University of Maryland has provided 38.2 MHz imaging riometers for each AGO. Each instrument incorporates a 16-beam phased array antenna similar to the 49 beam array described in *Detrik and Rosenberg* [1990]. Auroral precipitation events of most interest to riometer observation have electron energies in the few tens of keV, so that the most significant CNA effects occur near 90 km altitude, so called the ionospheric D region.

Although zenith-viewing riometers were originally used, the use of antenna arrays producing multiple narrow beams is necessary in order to examine the spatial scale of regions of energetic electron precipitation, and to resolve time development from spatial motion. The imaging riometer provides good spatial and temporal resolution for examining auroral precipitation events. The imaging riometer can be operated year-round since it is not affected by sunlight and cloud cover and therefore it supplements the all-sky camera data. The lower spatial resolution permits it to operate with higher time resolution than the all-sky camera without taxing the data recording capability of the AGO. The imaging riometer system employs two riometers for redundancy and to double the rate of data recording. The 12-bit analog-to-digital converter produces 24 bytes of data for one complete scan (in 12 sec) of the 16 beams for each riometer, resulting in a complete riometer image of the radio sky every 6 sec.

Fluxgate magnetometer

Bell Laboratories of Lucent Technologies has provided a fluxgate magnetometer for each AGO. Each instrument measures and records the three DC vector components of the geomagnetic field at 1-sec intervals. Each of the H, D, and Z components has positive northward, eastward, and upward respectively in the local geomagnetic coordinate system. Each component of this system has a noise level of typically 0.01 nT rms between 0 and 1 Hz. Similar magnetometers are deployed at South Pole station and McMurdo, Antarctica with 1 Hz sampling. Magnetic field values and variations are considered some of the most basic of diagnostics for ground-based observations of ionospheric and magnetospheric processes. They remain a basic and necessary component of most studies of these phenomena.

Search-coil magnetometer

Tohoku University has provided a search-coil magnetometer for each AGO. Variations in magnetic fields are measured in the three orthogonal components (N-S, E-W, and vertical in local geomagnetic coordinate system) by individual search-coils which are buried at a depth of 1 m from the snow surface with a distance of at least 5 m between to sensors. Each search coil has a linear frequency response from ~0.001 Hz to 2 Hz, and is equipped with a low pass filter with a cutoff frequency of 2 Hz. The output signals of each coil are sampled simultaneously at 0.5-s intervals and are digitized using a 12-bit A/D converter, providing a dynamic range of +/- 1.6 pT to +/- 3.2 nT at 1 Hz and +/- 160 pT to +/- 320 nT at 0.01 Hz. The search-coil magnetometer is suitable for measuring short-period geomagnetic pulsations such as Pc 1 and Pc 3. On the other hand, the fluxgate magnetometer is suitable for measurement of long-period magnetic pulsations such as Pc 5. Using these two magnetometers it becomes possible to observe the ULF signatures of MIEs a wide frequency range from 0.01 to 1 Hz.

All-sky auroral imager

From early April to late August during the Antarctic winter the dark sky above the stations permits optical observations of auroras for 24 hours a day. Lockheed Palo Alto Research Laboratories has developed special purpose low light level auroral all sky imagers for use in the AGOs. Each imager, which incorporates a two-channel all-sky intensified CCD camera with a single all-sky optical channel and a single detector, is capable of acquiring images in two different wavelengths (630.0 +/- 3.0 nm and 427.8 +/- 5.0 nm) simultaneously, and is optically identical to the imager installed at South Pole station. Long (30 sec) and short (2 sec) exposures are taken alternately to improve the dynamic range coverage, and an image set is taken every 2 min. Imager data have 10 km geographic resolution over most of the field of view, ranging to 30 km at the edges. Imager sensitivity is 20 Rayleighs in an 8-s exposure and dynamic range varies from 20 Rayleighs to 10,000 Rayleighs.

2.2 Magnetic field data processing

2.2.1 Spectral analysis

MIE-related geomagnetic pulsations in the frequency range of Pc 1 (0.2-5 Hz) to Pc 3 (0.02-0.1 Hz) were investigated using search-coil magnetometers installed at AGOs. The actual method for spectral estimation is based on the fast Fourier transform (FFT), but is more sophisticated than usual application which can basically be described as first windowing the time domain data, then performing the FFT. Our interest is in finding signals that are, most of the time, quiet faint with respect to the background spectrum. We have chosen the method developed by *Thomson* [1982]. This gives a smoother spectrum and is free from loss of information or any bias problems. Thomson's algorithm is developed along the following general outline. The discrete Fourier transform is written in time-centered form as

$$y(f) = \sum_{t=0}^{N-1} e^{-i2\pi f\left[t-\frac{N-1}{2}\right]} \cdot x(t). \tag{2-1}$$

The time series x(t) is assumed to be a stationary zero-mean process. Therefore, it can be described by the spectral representation of *Cramer* [1940], and is given by

$$x(t) = \int_{-1/2}^{+1/2} e^{i2\pi f' t} dZ(f'), \tag{2-2}$$

where dZ(f') is a random orthogonal-increments measure which is also a function of frequency f'. As a result

$$y(f) = \int_{-1/2}^{+1/2} \left[\sum_{t=0}^{N-1} e^{-i2\pi (f'-f)\left[t-\frac{N-1}{2}\right]} \right] dZ(f'), \tag{2-3}$$

which reduces to

$$y(f) = \int_{-1/2}^{+1/2} \frac{\sin[N\pi(f-f')]}{\sin[\pi(f-f')]} dZ(f'). \tag{2-4}$$

Equation (2-4) can be treated as a linear Fredholm integral equation of the first kind [*Thomson*, 1982]. Generally, these equations are convolutions

$$y = K * z, \tag{2-5}$$

where $y \equiv y(f)$, $K \equiv \sin(N\pi f)/\sin(\pi f)$, and $z \equiv dZ(\nu)$. The function K obeys an integral eigenvalue equation

$$\lambda_m \psi_m = K * \psi_m, \tag{2-6}$$

which is closely related to the solution of (2-5).

$$z = \sum_m \frac{1}{\lambda_m} y_m \psi_m, \tag{2-7}$$

with the coefficients y_m derivable from the Fourier-Bessel formula

$$y_m = \frac{1}{\lambda_m} \int y \psi_m, \tag{2-8}$$

where λ_m are eigenvalues of (2-6). The eigenfunctions are known and are referred to as prolate spheroidal wavefunctions [*Slepian*, 1978]

$$\psi_m \equiv U_m(N,W;f), \tag{2-9}$$

governed by the integral eigenvalue equation

$$\lambda_m(N,W) \cdot U_m(N,W;f) = \int_{-W}^{+W} \frac{\sin[N\pi(f-f')]}{\sin[\pi(f-f')]} U_m(N,W;f')df', \tag{2-10}$$

with W being the local frequency bandwidth about f, such that f-W<ν<f+W. Note that U_m(N, W;f) drops to zero outside this range. Using this result, one can determine the eigencoefficients

$$y_m(f) = \frac{1}{\lambda_m(N,W)} \int_{-W}^{+W} U_m(N,W;f')y(f+f')df'. \tag{2-11}$$

The function y(f+ν) can be replaced with its discrete Fourier transform giving

$$y_m(f) = \sum_{t=0}^{N-1} x(t)\varepsilon_m V_m(N,W;t)e^{-i2\pi f\left[t-\frac{N-1}{2}\right]}, \tag{2-12}$$

where ε_m = +1 (-1) for m-even (-odd), and

$$V_m(N,W;t) = \frac{1}{\varepsilon_m \lambda_m(N,W)} \int_{-W}^{+W} U_m(N,W;f) e^{-i2\pi ft} df \qquad (2\text{-}13)$$

is the time domain representation of the prolate spheroidal wave functions. Thus, $V_m(N,W;t)$ is known as the mth discrete prolate spheroidal sequence[*Slepian*, 1978].

Then the resulting spectrum for the kth order is given as a sum of the first kth spectra, weighted by weighting functions, dk, to minimize the bias

$$\overline{S}(f) = \sum_{m=0}^{K-1} \left| d_k(f) \cdot y_k(f) \right|^2 . \qquad (2\text{-}14)$$

For details and justifications of the calculation of weight factors see *Thomson* [1982].

2.2.2 Convection pattern analysis

Geomagnetic variations were studied in the context of equivalent convection patterns in the ionosphere. It is well known that for a uniform ionospheric conductance distribution the equivalent current distribution is solely due to ionospheric Hall currents [cf. *McHenry and Clauer*, 1987; *Glassmeier et al.*, 1989; *Glassmeier and Heppner*, 1992]. Thus the ionospheric plasma drift direction that is opposite to the Hall current direction can be obtained by rotating the horizontal magnetic perturbation vector by 90° counterclockwise. When a global network of magnetometer is available, we can get snapshots of equivalent ionospheric convection pattern by this method. To extract the signal of interest, which has a period much shorter than the slow changes of the large-scale ionospheric current system, a 30 min running average was used in this analysis. The data values 15 min before and after the specific time are averaged and subtracted from each geomagnetic field component. This is equivalent to high-pass filtering the magnetometer data with a 30-min frequency cutoff.

Each station is distributed in the geomagnetic polar plot centered in the corrected geomagnetic (CGM) pole. All the magnetic field vectors are also rotated into CGM coordinates from the local geomagnetic coordinates at first. In order to convert into CGM following scheme is used

$$\begin{pmatrix} X \\ Y \end{pmatrix} = \begin{pmatrix} \cos(\varphi_{dec} - \varphi_{oval}) & -\sin(\varphi_{dec} - \varphi_{oval}) \\ \sin(\varphi_{dec} - \varphi_{oval}) & \cos(\varphi_{dec} - \varphi_{oval}) \end{pmatrix} \begin{pmatrix} H \\ D \end{pmatrix} \qquad (2\text{-}15)$$

where, X and Y and the northward and eastward magnetic field components in the CGM system, φ_{dec} is the IGRF declination, φ_{oval} is the CGM oval angle, and H, D are the magnetic field northward and eastward components in local magnetic coordinates respectively.

The CGM coordinates have proven to be excellent tools in organizing geophysical phenomena controlled by the Earth's magnetic field, like auroral boundaries, high and middle latitude ionospheric currents, etc. By definition, the CGM coordinates (latitude, longitude) of a point in space are computed by tracing the Definite/International Geomagnetic Reference Field (DGRF/IGRF) magnetic field line through the specified point to the dipole geomagnetic equator, then returning to the same altitude along the dipole field line and assigning the obtained dipole latitude and longitude as the CGM coordinates to the starting point. The GEO-CGM code (version 9.9) provided by National Space Science Data Center at the Goddard Space Flight Center was used to compute the CGM coordinates and several other main geomagnetic field parameters for specified points at the Earth's surface (geographic coordinates) or in near-Earth space.

2.3 All-sky imager data processing

All-sky imagers (ASIs) at South Pole, Arrival Height, and AGO sites are used in this study. Particularly, image data from the ASI at South Pole station of National Institute of Polar Research, Japan (NIPR-ASI) were analyzed in detail. This ASI was installed in the 1996-1997 austral summer season. The NIPR-ASI consists of a high sensitive (monochromatic and panchromatic) optical lens, CCD camera, and data-taking workstation. The NIPR-ASI is equipped with interference filters of $N2^{+}$ 427.8 nm, OI 557.7 nm, OI 630.0 nm, and OH 730.0 nm. The image sensor is a back-illuminated air-cooled CCD camera with 512 × 512 pixels.

In order to obtain correct distributions of auroral intensity and to facilitate comparisons of the results with those of other instruments, the raw image data obtained with the NIPR-ASI are processed in a sequence as follows: 1) correction for non-uniformity of sensitivity over the image, 2) Correction for the van Rijin effect and the atmospheric extinction, and 3) coordinates transformation.

2.3.1 Calibration data processing

The first step to process raw image data is the corrections for non-uniformity of sensitivity over an image plane. Non-uniformity calibration data contains the count number N(x, y) in the four directions (left, right, up, down) from the center of a image at the interval of 10 degrees in zenith angle. First, the count number $N(x,y)$ is normalized by the count number $N(x_C, y_C)$ at the zenith of the image. These calibration data are interpolated with minimum curvature surface (a thin-plate-spline surface). In this way, a flat sensitivity image data $S_{flat}(x, y)$ for the raw image data $S(x, y)$ is obtained as

$$S_{flat}(x,y) = \frac{N(x_C, y_C)}{N(x,y)} S(x,y). \tag{2-16}$$

To represent the intensity of aurora with the Rayleigh unit, the sensitivity coefficient K for each filter and the exposure time T of the optical observation are used. That is, the radiance I is calculated as

$$I = S_{flat}(x,y) \cdot K \cdot T. \tag{2-17}$$

2.3.2 Corrections for van Rhijin effect and atmospheric extinction

Let us now consider an emission layer at an altitude h from the ground. If the thickness of the emission layer is negligible compared to the earth radius R, the ratio of the intensity at zenith angle θ to that at the zenith is proportional to the length of the line of sight in the emission layer. The intensity at zenith angle θ, $I(\theta)$ is given by

$$I(\theta) = I(0) \cdot V(h, \theta), \tag{2-18}$$

$$V(h,\theta) = \left[1 - \left(\frac{R}{R+h} \right)^2 \sin^2\theta \right]^{-\frac{1}{2}}, \tag{2-19}$$

where $I(0)$ is the intensity at the zenith and $V(h, \theta)$ is called the van Rijin function. The correction for van Rijin effect is made with assuming that the emission heights of $N2^+$ 427.8 nm, OI 557.7 nm, OI 630.0 nm, and OH 730.0 nm are 110 km, 110 km, 200 km, and 110 km respectively. The geometry of all-sky auroral imaging is depicted in Figure 2-3.

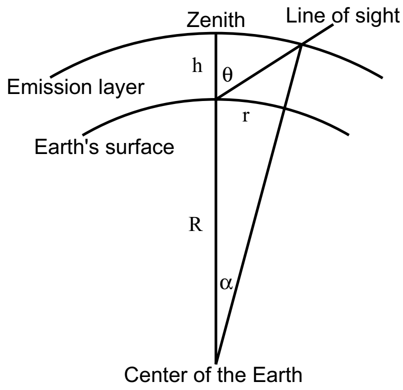

Figure 2-3. Geometry of all-sky auroral imaging.

Auroral intensities observed at the ground are also affected by atmospheric extinction. A relation of the apparent auroral intensity $I(\theta)$ at the ground to the true auroral intensity $I_{true}(\theta)$ at the emission layer is given by

$$I(\theta) = I_{true}(\theta) \cdot 10^{-0.4aF(\theta)} \tag{2-20}$$

and

$$F(\theta) = \frac{1}{\cos(\theta) + 0.15(93.885 - \theta)^{-1.253}}, \tag{2-21}$$

where $F(\theta)$ is an empirical equation which shows air mass at zenith angle θ [*Kasten*, 1966], and a is the atmospheric extinction coefficient. For simplicity and variable conditions, we assumed the value a as 0.3, 0.15, 0.07, and 0.05, for 427.8 nm, 557.7 nm, 630.0 nm, and 730.0 nm respectively for all observation data. In order to reject the data with large ambiguity, the coverage in the field of view in the range of $\theta > 75°$ is not used for the data correction.

2.3.3 Transformation of coordinates

The raw data is fish eye images in which the distance from the center of the images is proportional to the zenith angle. We call this as fish eye coordinates. Since an image in the fish eye coordinates is inconvenient to discuss the distribution of auroral intensity, it is necessary to transform an image from the fish eye coordinate to the geographic or geomagnetic coordinates. The relation between the zenith angle θ and the geographical distance r from an observation site is given by

$$r = R\alpha, \tag{2-22}$$

$$\alpha = \theta - \sin^{-1}\left(\frac{R\sin\theta}{R+h}\right). \tag{2-23}$$

Since the direction of auroral emission and the geographic coordinates of the observation point are known, the geographic coordinates of the emission can be calculated using spherical trigonometry. In this way, the auroral distribution in the fish eye coordinates is converted into geographic coordinates. Once the geographic position was determined, we can calculate the CGM position, which is useful rather than geographical information to discuss the electrodynamics in the polar region by the GEO-CGM code (see section 2.2.2).

By executing these kinds of coordinate transformations, it becomes easier to discuss the distribution of auroral intensity, direction and speed of the motion of the auroral structure, and also to compare auroral image data with data obtained by other instruments within the imaging coverage.

2.4 Interplanetary data processing

Magnetohydrodynamic (MHD) discontinuities and shock waves are often observed in the solar wind. Among them, tangential discontinuities (TDs) and rotational discontinuities (RDs) are most frequently seen. At a tangential discontinuity, the normal component of magnetic field is zero, and the normal flow velocity relative to the discontinuity also vanishes. The total pressure is balanced, while the tangential magnetic field and flow may change arbitrarily across the tangential discontinuity. On the other hand, a rotational discontinuity has a finite normal component of magnetic field. In the ideal MHD, the field strength and plasma density are constant across a rotational discontinuity. It is needed to calculate the normal vector of the discontinuity plane not only for distinguish these two discontinuities but also deduce the propagation time delay of the signal observed at a satellite located in the solar wind. Once the normal vector is determined, the propagation time from the satellite to the magnetosphere is calculated by the relation

$$t = \frac{\mathbf{n}\cdot(\mathbf{P}-\mathbf{S})}{\mathbf{n}\cdot\mathbf{V}}. \tag{2-24}$$

Where **V** is the solar wind speed, **S** is the location of the satellite, and **P** is the contact point of the discontinuity. Basically, we could determined the normal vector if the same discontinuity observed by the three satellites assuming that the solar wind speed is constant. The normal vector is determined by the plane that has three points

$$(t_1 - t_i)\mathbf{V} + \mathbf{S}_i, \qquad i = 1, 2, 3 \tag{2-25}$$

where t_i is the time when the satellites observe the discontinuity, $\mathbf{S}_i$ is the position of each satellite.

On the other hand, the minimum variance analysis (MVA) is known as a classical method which determines the normal vector from only one satellite magnetic field observation [e.g. *Sonnerup and Cahill*, 1967]. Since the magnetic induction field **B** is divergence free, its normal component must be continuous across any infinitely thin interface. Therefore, the normal vector is chosen so that the standard deviation of the individual products $\mathbf{B}^i\cdot\mathbf{n}$ from the average value $\overline{\mathbf{B}}\cdot\mathbf{n}$ becomes a minimum. Here $\mathbf{B}^i$ represents an individual field measurement, and $\overline{\mathbf{B}}$ is the average of the N field measurements used in the calculation

$$\sigma^2 = \frac{1}{N}\sum_{i=1}^{N}(\mathbf{B}^i\cdot\mathbf{n} - \overline{\mathbf{B}}\cdot\mathbf{n})^2. \tag{2-26}$$

It is well known that the minimization of (2-26) is equivalent to finding the smallest eigenvalue of the covariant matrix

$$M_{\alpha\beta} = (\overline{B_\alpha B_\beta} - \overline{B}_\alpha \overline{B}_\beta), \qquad \alpha,\ \beta = 1,\ 2,\ 3 \tag{2-27}$$

where B_α and B_β are the Cartesian components of an individual measured field vector and the overhead bar denotes an average over all measurement used in the calculation. The normal vector is the eigenvector of (2-27) corresponding its smallest eigenvalue. Equivalenntly, the normal vector coincides with the shortest principal axis if the variance ellipsoid defined by the quadratic form (2-26). When the two smallest eigenvalues of $M_{\alpha\beta}$ are almost equal, the determination of **n** becomes inaccurate. Only cases where the ratio of the intermediate to the smallest eigenvalue exceeds 8.0 are contained in this study.

Chapter 3

A case study of a MIE on June 6, 1997

3.1 The magnetic impulse event

The magnetic impulse event analyzed herein is shown in Figure 3-1. In this figure are plotted the local geomagnetic south-north, west-east, and vertical (H, D, and Z respectively) component magnetic field traces for the interval 1530 – 1630 UT on June 6, 1997, for ten Antarctic stations. (See next section for further definitions of the stations and the definition of coordinates.) These traces are plotted from 10 sec averaged data after subtracting the median value of each component during the one hour interval. The geomagnetic signature at the near-cusp station SP (South Pole) is a classic MIE signature according to the criteria in *Konik et al.* [1994] (see also *Lanzerotti et al.* [1991]).

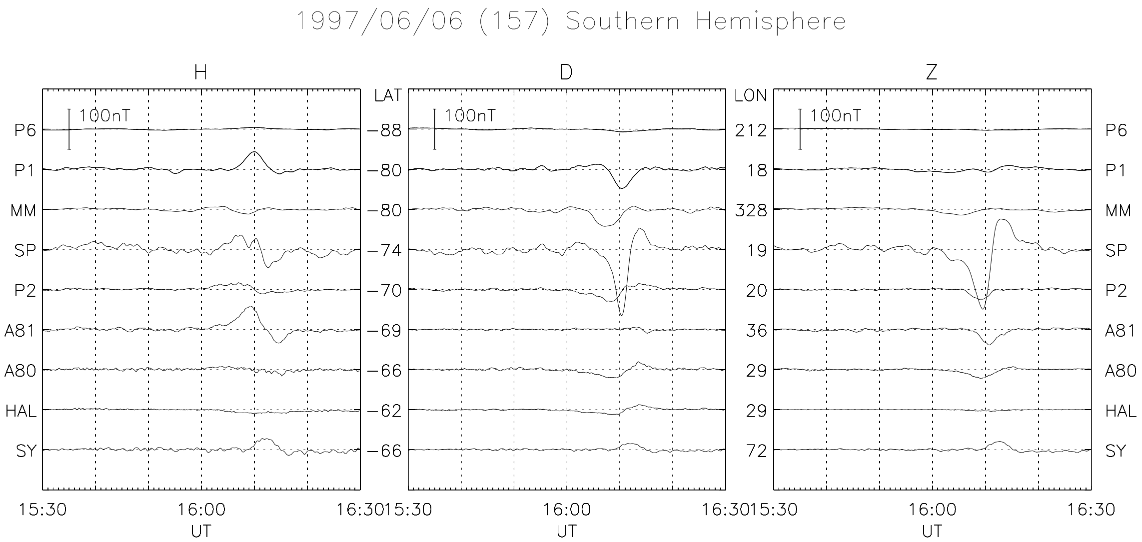

Figure 3-1. Three components of ground-based geomagnetic field data obtained at nine sites in the Antarctic between 1530 - 1630 UT on June 6, 1997. A magnetic impulse event (MIE) is most evident at South Pole Station with amplitudes of 150 and 160 nT in the Z and D components, respectively.

Out of a rather quiet background a sudden impulse appears at ~ 1610 UT in the Z-component magnetic field with an amplitude ~ 150 nT. The amplitude in the D-component is also large, ~ 160 nT, while the H-component is much smaller. The H trace appears to be composed of two components: a pulse train and a soliton, the soliton being of similar (but inverted) character to the 'event' identified for D and Z components. This interval was geomagnetically quiet, with Kp=1+ and Σ Kp = 13 for the previous 24 hours. The principal reason why we selected this event for a detailed case study is that auroral image data from multiple optical sites covering the dayside cusp, LLBL and polar cap region are available. Some researches on MIEs have already made use of optical data, generally from single locations, to examine the particle precipitation that can accompany the events [*Fukunishi and Lanzerotti*, 1989; *Mende et al.*, 1990; *Sandholt et al.*, 1990; *Vorobjev*, 1994; *Lühr et al.*, 1996]. These results provide evidence that the events appear to coincide with the structured field aligned electrical currents out of the ionosphere. If multiple optical sites were available during a MIE, the data would provide important additional information on the energy content, motion, and current structure of the MIE. Since this event occurred almost at the southern winter solstice, optical data were available in the southern hemisphere.

3.2 Data sets

An extensive set of ground- and space-based data were examined, consulted, and used in this investigation in order to provide as much information and insight as possible on the initiation and evolution of the magnetic impulse event of June 6, 1997 (Figure 3-1). By examining in detail as much relevant geophysical data as can be assembled, we provide in this paper the first exhaustive description of the generation, motion, scale size, and end-of-life of a MIE accompanied by a TCV. The geophysical coordinates of all of ground observatories are provided in Table 3-1.

Table 3-1. Geographic and geomagnetic coordinates of the observatories.

CODE		GLAT	GLON	MLAT	MLON	UT-MLT
		CANOPUS magnetometer chain				
SIM	Fort Simpson	61.8	238.8	67.6	291.9	9:04
CON	Contwoyto Lake	65.8	248.8	73.4	301.9	8:23
SMI	Fort Smith	60.0	248.1	67.8	304.6	8:13
MCM	Fort Mcmurray	56.7	248.8	64.7	307.2	8:04
RAB	Rabbit Lake	58.2	256.3	67.5	317.1	7:27
TAL	Taloyoak	69.5	266.5	79.2	328.3	6:46
RAN	Rankin Inlet	62.8	267.9	73.1	334.3	6:27
ESK	Eskimo Point	61.1	266.0	71.4	331.4	6:37
CHU	Fort Churchill	58.8	265.9	69.2	331.9	6:35
ISL	Island Lake	53.9	265.3	64.4	331.9	6:35
PIN	Pinawa	50.2	264.0	60.7	330.3	6:40
		MACCS				
IG	Igloolik	69.3	278.2	79.2	352.5	5:25
RB	Repulse Bay	66.5	273.8	76.7	344.1	5:54
CH	Coral Harbour	64.1	276.8	74.5	349.9	5:34
CD	Cape Dorset	64.2	283.4	74.3	1.6	4:54
IQ	Iqualuit (*Bell Labs)	63.8	291.5	73.1	15.0	4:06
		GREENLAND magnetometers				
THL	Thule	77.5	290.8	85.5	33.9	2:53
KUV	Kullorsuaq	74.6	302.8	81.3	44.8	2:04
UPN	Upernavik	72.8	303.9	79.6	42.2	2:15
UMQ	Umanaq	70.7	307.9	77.0	44.1	2:06
GDH	Godhavn	69.3	306.5	75.9	40.5	2:22
ATU	Attu	67.9	306.4	74.7	39.1	2:28
STF	Sondre Stromfjord	67.0	309.3	73.3	41.8	2:16
SKT	Sukkertoppen	65.4	307.1	72.1	38.0	2:34
GHB	Godthab	64.2	308.3	70.7	38.6	2:31
FHB	Frederikshab	62.0	310.3	68.1	39.7	2:26
NAQ	Narsarsuaq	61.2	314.6	66.4	43.9	2:06
NRD	Nord	81.6	343.3	80.9	106.3	21:14
DMH	Danmarkshavn	76.8	341.4	77.3	87.4	22:36
DNB	Daneborg	74.3	339.8	75.2	80.7	23:07
SCO	Scoresbysund	70.5	338.0	71.7	73.4	23:42
AMK	Ammassalik	65.6	322.4	69.4	54.7	1:15
TJ	Tjornes (*NIPR)	66.2	342.9	66.5	73.0	23:41

Table 3-1. continued.

CODE		GLAT	GLON	MLAT	MLON	UT-MLT
		IMAGE magnetometer network				
NAL	Ny Alesund	78.9	12.0	76.1	112.2	20:47
LYR	Longyearbyen	78.2	15.8	75.1	113.0	20:44
HOR	Hornsund	77.0	15.6	74.0	110.4	20:53
HOP	Hopen Island	76.5	25.0	72.9	115.8	20:31
BJN	Bear Island	74.5	19.2	71.3	108.8	20:58
SOR	Soroya	70.5	22.2	67.2	106.8	21:06
KEV	Kevo	69.8	27.0	66.2	109.8	20:53
TRO	Tromso	69.7	18.9	66.5	103.5	21:19
MAS	Masi	69.5	23.7	66.1	107.0	21:05
AND	Andenes	69.3	16.0	66.4	101.0	21:30
KIL	Kilpisjarvi	69.0	20.8	65.8	104.3	21:15
MUO	Muonio	68.0	23.5	64.6	105.7	21:09
LOZ	Lovozero	68.0	35.1	64.1	114.9	20:33
KIR	Kiruna	67.8	20.4	64.6	103.2	21:20
SOD	Sodankyla	67.4	26.6	63.8	107.7	21:01
PEL	Pello	66.9	24.1	63.5	105.4	21:11
OUJ	Oulujarvi	64.5	27.2	60.9	106.6	21:06
HAN	Hankasalmi	62.3	26.7	58.6	105.0	21:12
NUR	Nurmijarvi	60.5	24.7	56.8	102.5	21:22
		Southern hemisphere magnetometers				
P6	US-AGO P6	-72.1	127.9	-87.8	212.2	14:41
P1	US-AGO P1	-83.9	129.6	-80.1	17.6	3:43
MM	Mcmurdo	-77.9	166.7	-80.0	327.7	6:55
SP	South Pole	-90.0	0.0	-74.0	18.9	3:35
P2	US-AGO P2	-85.7	313.6	-69.8	19.7	3:28
A81	BAS-AGO A80	-81.5	3.0	-68.5	36.3	2:18
A80	BAS-AGO A81	-80.8	339.6	-66.2	29.3	2:46
HB	Halley	-75.6	333.6	-61.5	29.3	2:43
SY	Syowa	-69.0	39.6	-66.1	71.9	23:56

Ground-based geomagnetic data

Throughout this paper, the H, D, and Z components are used to designate local geomagnetic coordinate directions: H for south-north (magnetic field increase northward), D for west-east (field increase eastward), and Z for vertical (increases in field corresponding to changes downward in the northern hemisphere and upward in the southern hemisphere). The geomagnetic data from the Antarctic that provided the first evidence of the MIE (Figure 3-1) were acquired from the set of two independent Automatic Geophysical Observatories (AGOs) U. S. AGOs and U. K. AGOs, and the two year-round stations South Pole (SP), McMurdo (MM), and Halley (HB). The locations of the Antarctic observations used in this study are shown in Figure 3-2a in both geomagnetic (solid lines) and geographic (dashed lines) coordinates.

During this event, geomagnetic data from U. S. AGOs P1, P2, and P6 were available. The British AGOs that provided data to the study are identified A80 and A81. Also shown are the locations of the Japanese station at Syowa (SY), whose data were consulted. The intersecting fields of view of HF backscatter radars located at Halley and South Africa Sanae station are indicated. The over-all instrumentation and objectives of the U.S. AGO program are provided in *Rosenberg and Doolittle* [1994]. The design, instrumentation, and deployment of the British AGOs are discussed in detail in *Dudeney et al.* [1998].

Geomagnetic data in the hemisphere conjugate to the Antarctic were acquired with wide local time coverage. Five sites associated with the MACCS array (solid squares) in Canada [*Hughes and Engebretson*, 1997], CD, CH, RB, IG, and CY, are illustrated on a geomagnetic (solid lines) and geographic (dotted lines) map in Figure 3-2b. Also shown in Figure 3-2b are the locations of the Canadian Space Agency CANOPUS sites (solid triangles), magnetometers of the Danish Meteorological Institute (DMI) in Greenland (solid diamonds), the Scandinavian IMAGE magnetometer network (solid circle) [*Lühr et al.*, 1998], and two conjugate stations IQ (SP conjugate point) of Bell Laboratories and TJ (SY conjugate point) of NIPR, whose data have been used to further illustrate the characteristics of the MIE. The GEO-CGM code provided by the NSSDC at NASA Goddard Space Flight Center was used to compute the geomagnetic parameters (http://nssdc.gsfc.nasa.gov/space/cgm/cgm.html). The open circles show the CGM conjugate points to the Antarctic observatories in order to provide geomagnetic references for the discussions below.

Antarctic-based optical data

Optical all sky imager data were available in the Antarctic at MM, SP, and P1 at the time of the MIE. Unfortunately, cloud cover at P1 prevented good seeing during several hours around the MIE. The optical instrumentation is outlined in *Rosenberg and Doolittle* [1994] for the AGOs. The MM data are from instrumentation provided by the University of Newcastle, Australia. At both SP and MM, two wavelengths are recorded simultaneously, 427.8 nm and 630.0 nm. One image is obtained at 1 min (2 min) intervals at SP (MM).

Ground-based riometer data

All sky imaging riometer data were available in the Antarctic at MM, SP, P1, and P2, and at the locations STF and IQ (cf. Figure 3-2b) in Greenland and Canada, respectively. The Antarctic all sky riometer system has been outlined in *Rosenberg and Doolittle* [1992] while the imaging riometer technique has been described in *Detrick and Rosenberg* [1990].

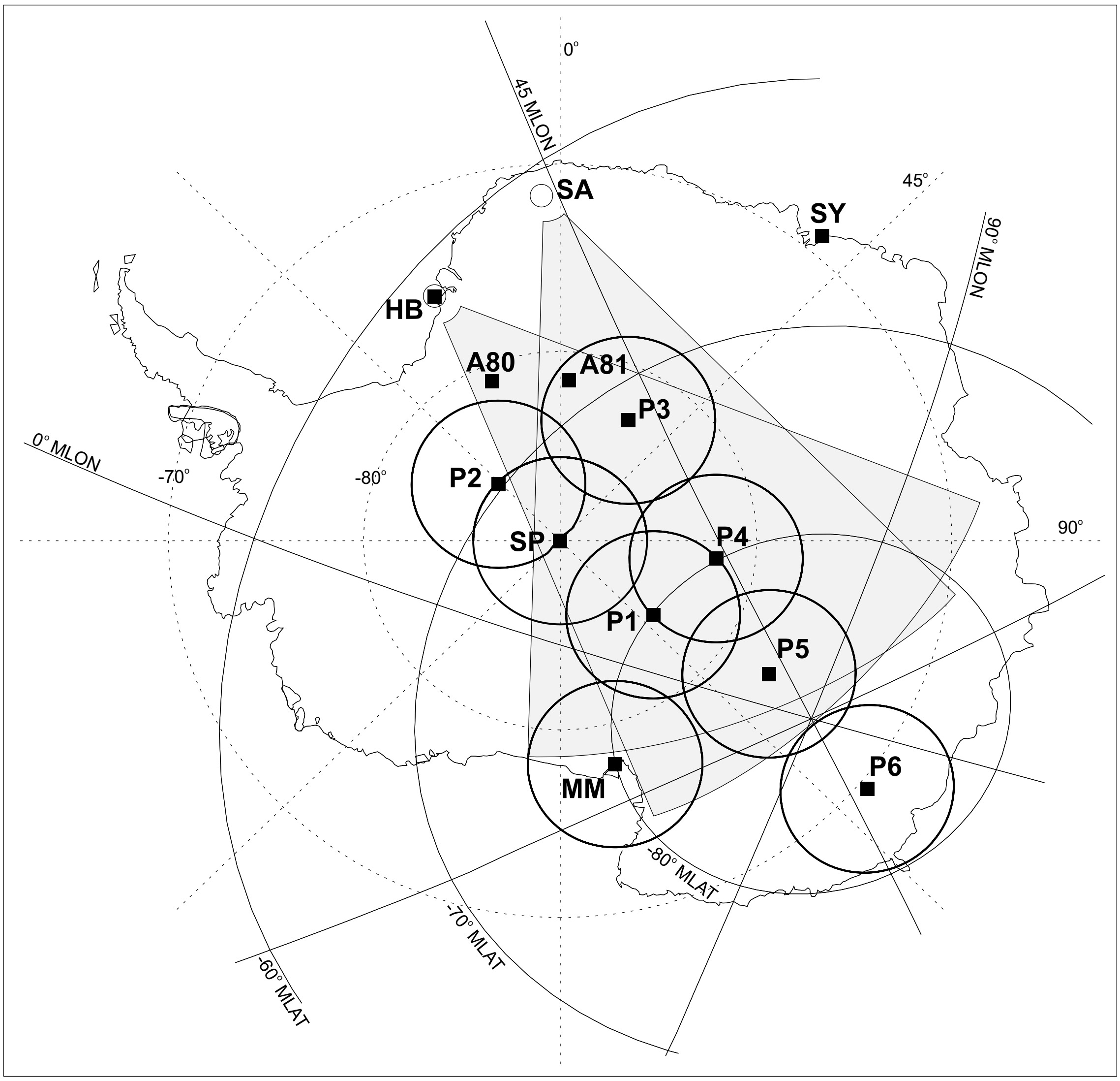

Figure 3-2a. Locations of the Antarctic observatories in geomagnetic (solid lines) and geographic (dashed lines) coordinates. The approximate size of the field of view for optical observation of each station is illustrated assuming that the altitude of the aurora is 200 km, which is typical for 630.0 nm emission. The gray zone delineates the area proved by HF radars that were used in this study.

Ground-based HF radar data

The SuperDARN coherent HF radars [*Greenwald et al.*, 1995] are designed to employ backscatter from high-latitude field-aligned ionospheric plasma density irregularities as tracers of the bulk plasma motion under the influence of the convection electric field. During the interval of this MIE, significant backscatter was observed only at the twin radars at Sanae (SA) and Halley (HB) (cf. Figure 3-2a) in Antarctica.

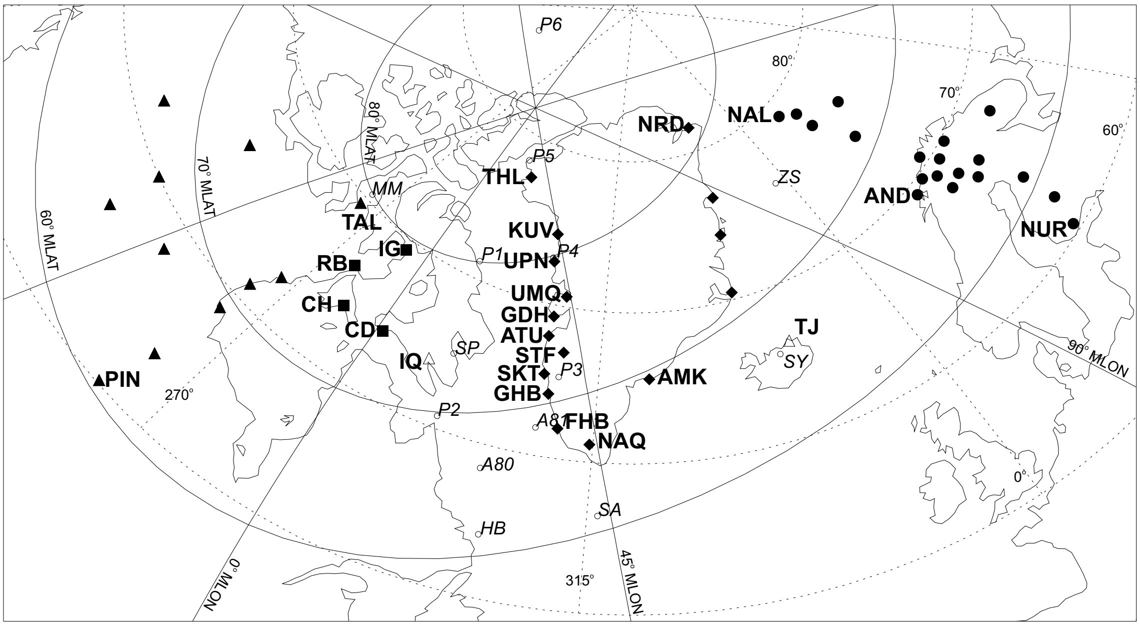

Figure 3-2b. Locations of the MACCS-array (black squares) and Greenland-chain (black diamonds) geomagnetic stations used in this study, plotted in both geomagnetic (solid lines) and geographic (dashed lines) coordinates. Also shown are the CANOPUS stations (black triangles) and IMAGE magnetometer chain (black circles). The conjugate locations for several Antarctic sites are shown as the open circles.

Space-based data

With the advent of the International Solar Terrestrial Physics (ISTP) program, data from a number of space-based missions were available that could be utilized to investigate the interplanetary conditions that prevailed at the time of the MIE and to examine the effects in the magnetosphere itself. Interplanetary data from the Wind, IMP8, Geotail, and Interball-Tail spacecraft have been consulted in order to provide information on the interplanetary magnetic field (IMF), solar wind velocity, and plasma number density. The locations of the spacecraft with respect to the locations of the model bow shock (from *Fairfield* [1971]) and magnetopause (from *Roelof and Sibeck* [1993] for solar wind conditions of B_Z = 2.5 nT and P = 2 nPa) are shown in Figure 3-2c.

Data in the magnetosphere at geosynchronous orbit were also available from magnetometer observations on the two NOAA satellites, GOES-8 and GOES-9. The locations of the two GOES are also shown in Figure 3-2c. Data from the low altitude polar orbiting DMSP F11 and F12 spacecraft were used to define the high latitude magnetosphere regions and boundaries prior to and during the MIE. These data, with information on the boundaries as provided by analyses and interpretations of the satellites' particle measurements are available at JHU/APL's Auroral Particles and Imagery Page (http://sd-www.jhuapl.edu/aurora/index.html).

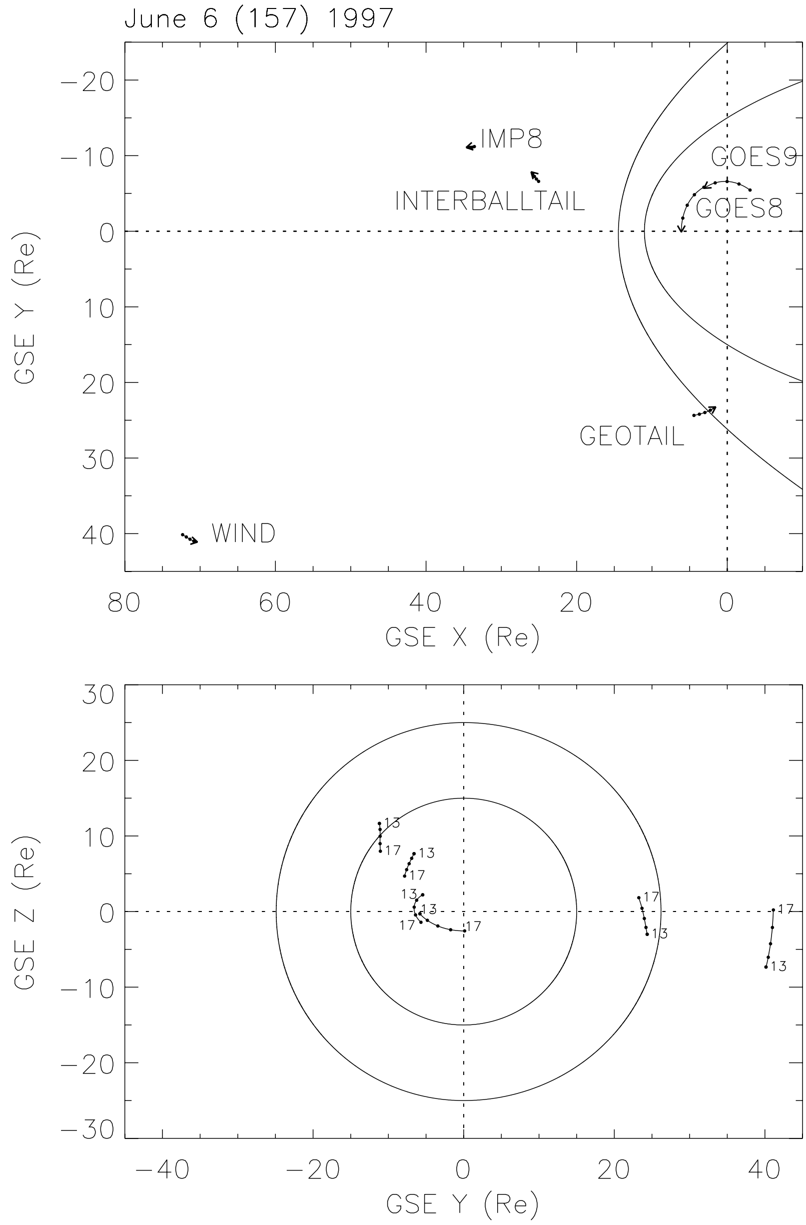

Figure 3-2c. Locations of the spacecraft during the interval 1300 - 1700 UT on June 6, 1997.

3.3 Geomagnetic data analysis

Ground magnetic variations

Time-intensity traces of all three components of the magnetic field at the northern hemisphere (CANOPUS, MACCS and Greenland) locations are shown in Figure 3-3 for the hours 1530 - 1630 UT, June 6. As for Figure 3-1, the traces are all plotted after subtracting the respective median values for the one-hour period. All of the data are averaged in 20 sec, which is the lowest sampling interval for the Greenland data.

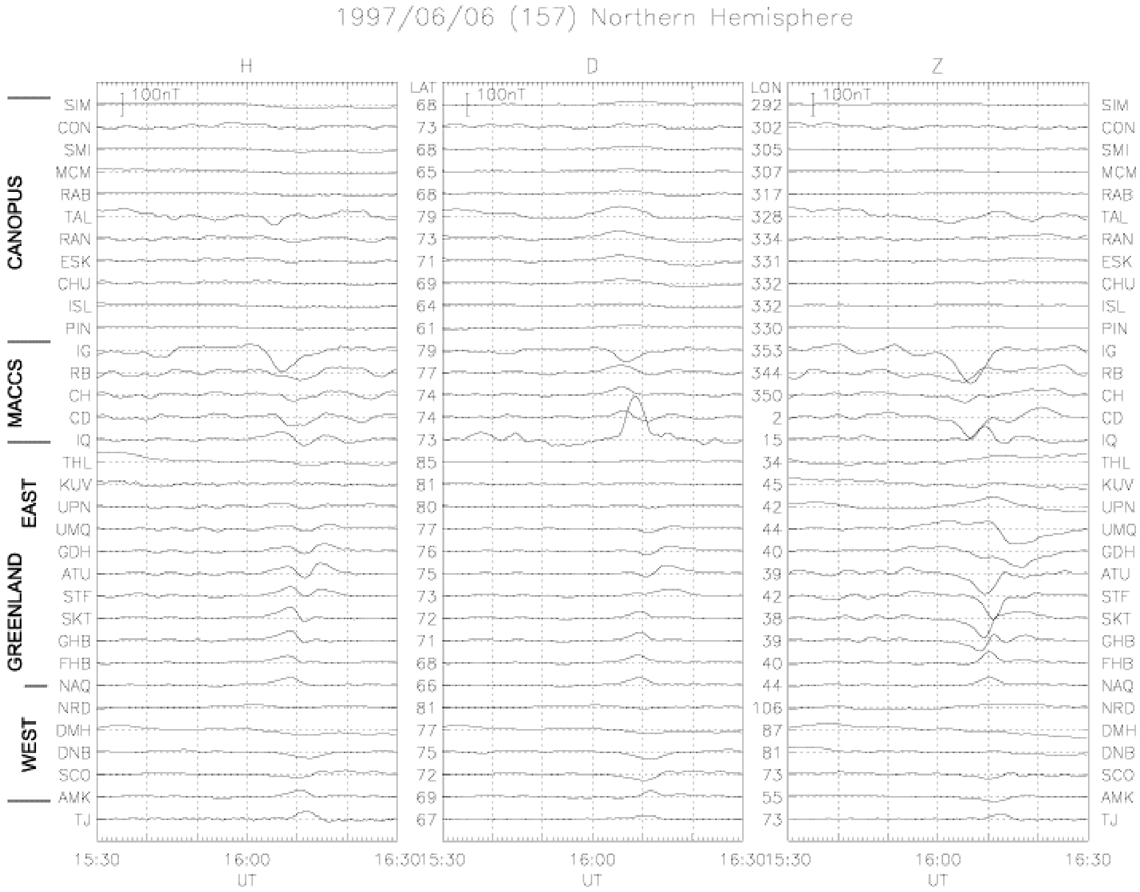

Figure 3-3. Time-intensity traces for all three magnetic field components measured at northern hemisphere magnetometer locations for the hour interval (1530 - 1630 UT) around the time of the MIE on June 6, 1997.

The CANOPUS stations are the upper 11 traces in Figure 3-3; the first five traces are the western-most locations; the next six CANOPUS traces are the eastern-most stations. Both sets of CANOPUS locations are plotted in approximately decreasing geomagnetic latitude. The MACCS stations are contained in traces 12-16 from the top, also plotted approximately in decreasing latitude. The west coast of Greenland locations are traces 17-27 from the top (or 6-16 from the bottom) plotted in order of decreasing latitude. The stations on the east coast of Greenland are plotted in order of decreasing latitude in traces 28-32 from the top (or 2-6 from the bottom). The bottom station TJ is a conjugate station of SY. The Z-component signals in Figure 3-3 at a number of the northern hemisphere stations satisfy the MIE identification criterion (absolute amplitude; amplitude above background; duration) established in *Konik et al.* [1994] (see also *Lanzerotti et al.* [1991]). Very clear and large impulsive Z-component signals appear suddenly at ~ 1610 UT above the much smaller fluctuations of the background geomagnetic field. The MIE signals are also large in the other two components in general.

Spectral features

Dynamic spectra of magnetic variations in the frequency band 0 - 0.1 Hz in the Antarctic in the time interval 0800 - 2000 UT on June 6, 1997 are shown as dynamic power spectra in Figure 3-4a for the local geomagnetic eastward component. The power spectra are plotted in order of descending geomagnetic latitude beginning from top to bottom. Search-coil magnetometer data were averaged over the 1 sec. Then power spectra were calculated with a data window of 10 min at every 2 min. over successive 10 min intervals. Each time interval differed from the preceding interval by 2 min. Here, each spectrum was calculated by applying five orthogonal prolate spheroidal data windows [*Thomson*, 1982] to the data set before fast Fourier transform (FFT) calculation.

Dynamic spectra in Figure 3-4b show that there were Pc3 activity enhancements in the power at 20-40 mHz in the interval 1500-1700 UT at four low latitude sites in the southern hemisphere. The frequency band shows slow drift to lower values during this two-hour interval. In addition, wideband enhancements were also observed at the MIE onset (~1600 UT) at the low latitude stations. Inspection of similar spectra for D- and Z-component variations (not shown) shows the same bands of enhancements and bursts at all of lower four stations.

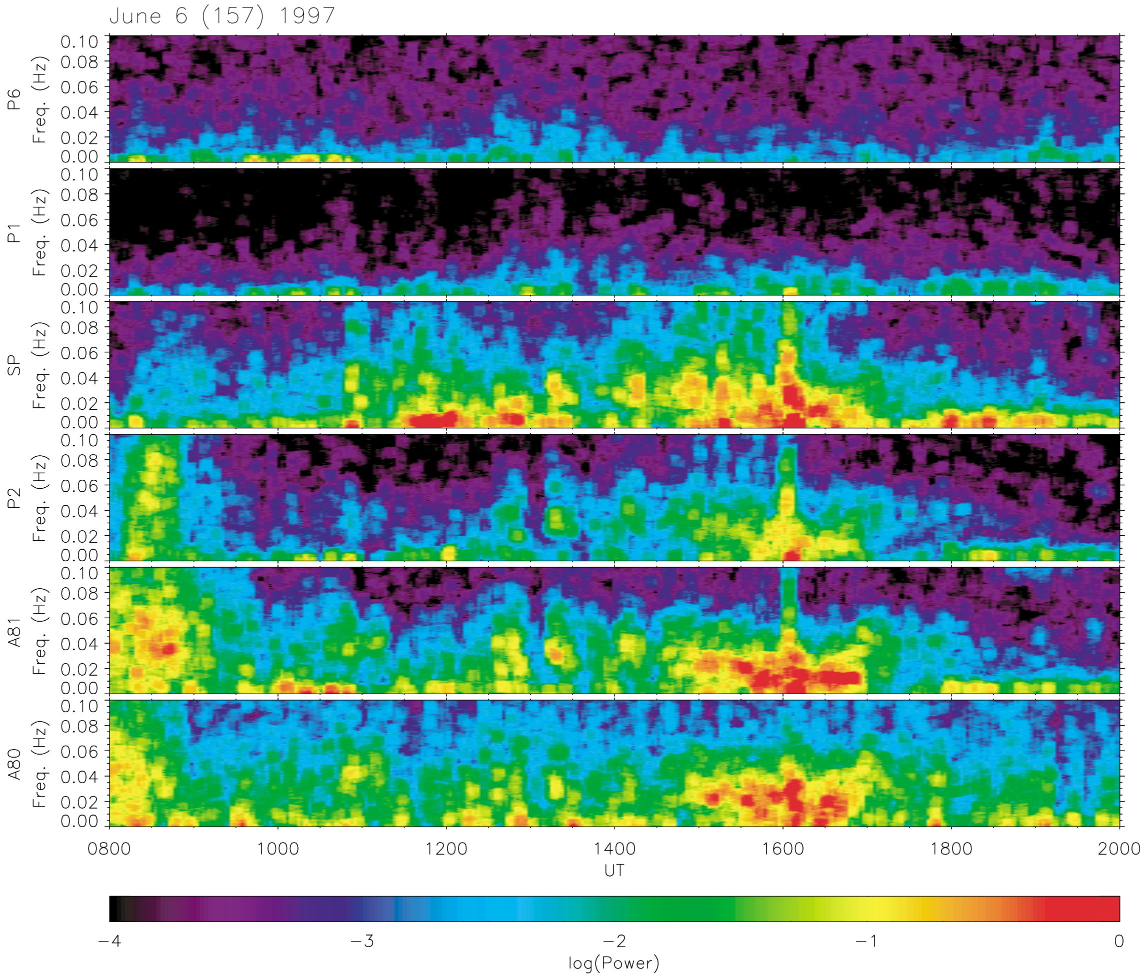

Figure 3-4a. Sliding dynamic spectra (0-0.1 Hz) from the D-component search-coil magnetometer data from top to bottom at six Antarctic stations in the interval 0800-2000 UT. The spectra are plotted from top to bottom in order of decreasing geomagnetic latitude.

Higher frequency (0-1.0 Hz) geomagnetic variations as measured by the Antarctic search-coil magnetometers were also investigated. Figure 4b shows the D-component dynamic spectra for each station in Antarctica. Using 0.5 sec sampling data, dynamic spectra in the frequency range 0-1.0 Hz were calculated with a data window of 1 min at every 15 sec. It is found that Pc 1 bursts occurred at 1606 UT at SP, P2, and A81. Since other stations did not observe such a burst signature, there is a finite extent in the latitudinal distribution of the Pc 1 bursts. The narrowband spectral peaks in the frequency range 0.2-0.3 Hz enable us to distinguish them from broadband Pi 1 pulsations. The spectra were mostly enhanced in the horizontal components.

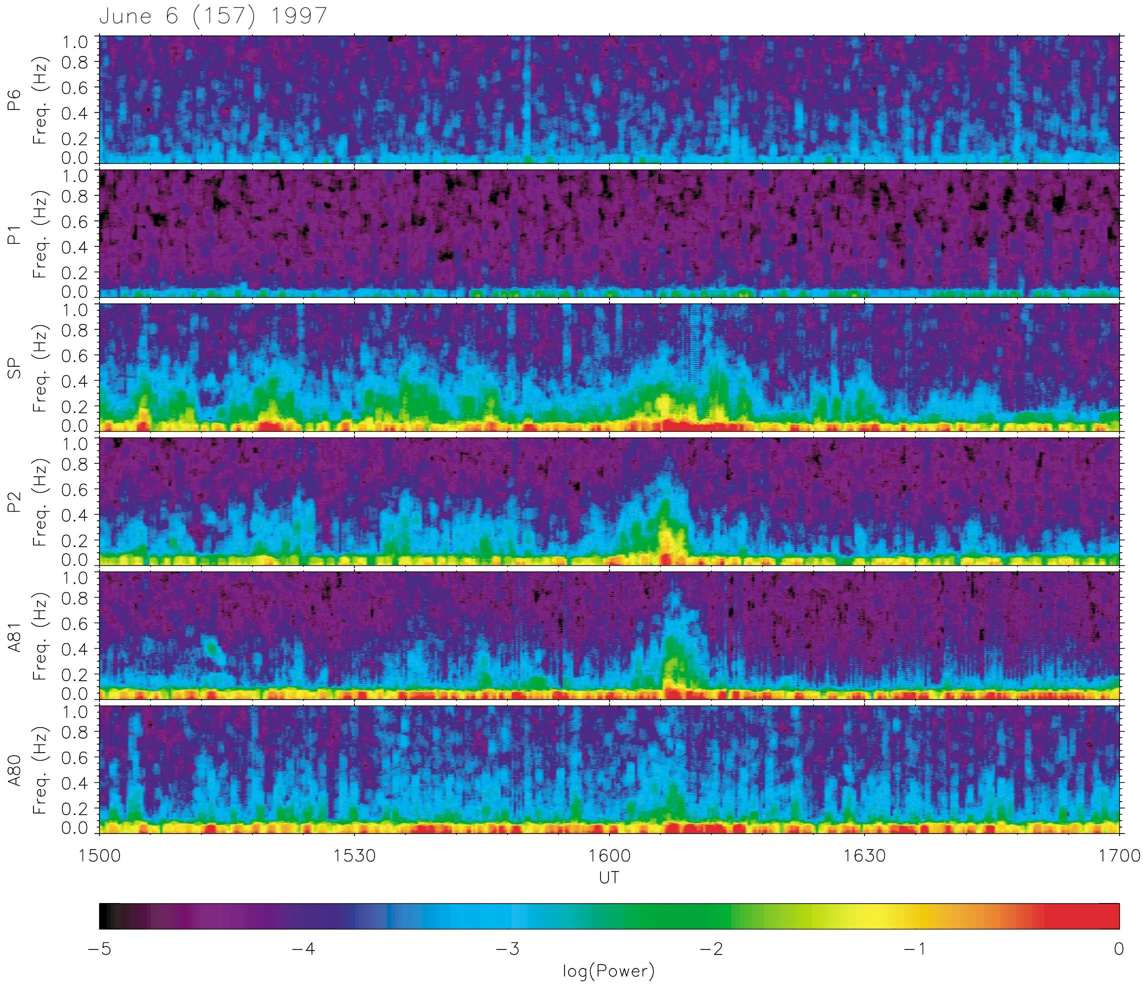

Figure 3-4b. Dynamic spectra (0-1.0 Hz) from D-component search-coil magnetometer data at six Antarctic stations in the time interval 1500 - 1700 UT.

Convection patterns

Geomagnetic variations were studied in the context of equivalent convection patterns in the ionosphere. To extract the signal of interest, which has a period much shorter than the slow changes of the large-scale ionospheric current system, a 30 min running average was used. The data values 15 min before and after the specific time are averaged and subtracted from each geomagnetic field component. This is equivalent to high-pass filtering the magnetometer data with a 30-min frequency cutoff. The magnetic field data used in Figure 3-5 have been high pass filtered as described above. It is well known that the direction of F-region ionospheric plasma drifts is rotated roughly by 90° counter clockwise from the direction of observed horizontal ground magnetic perturbations.

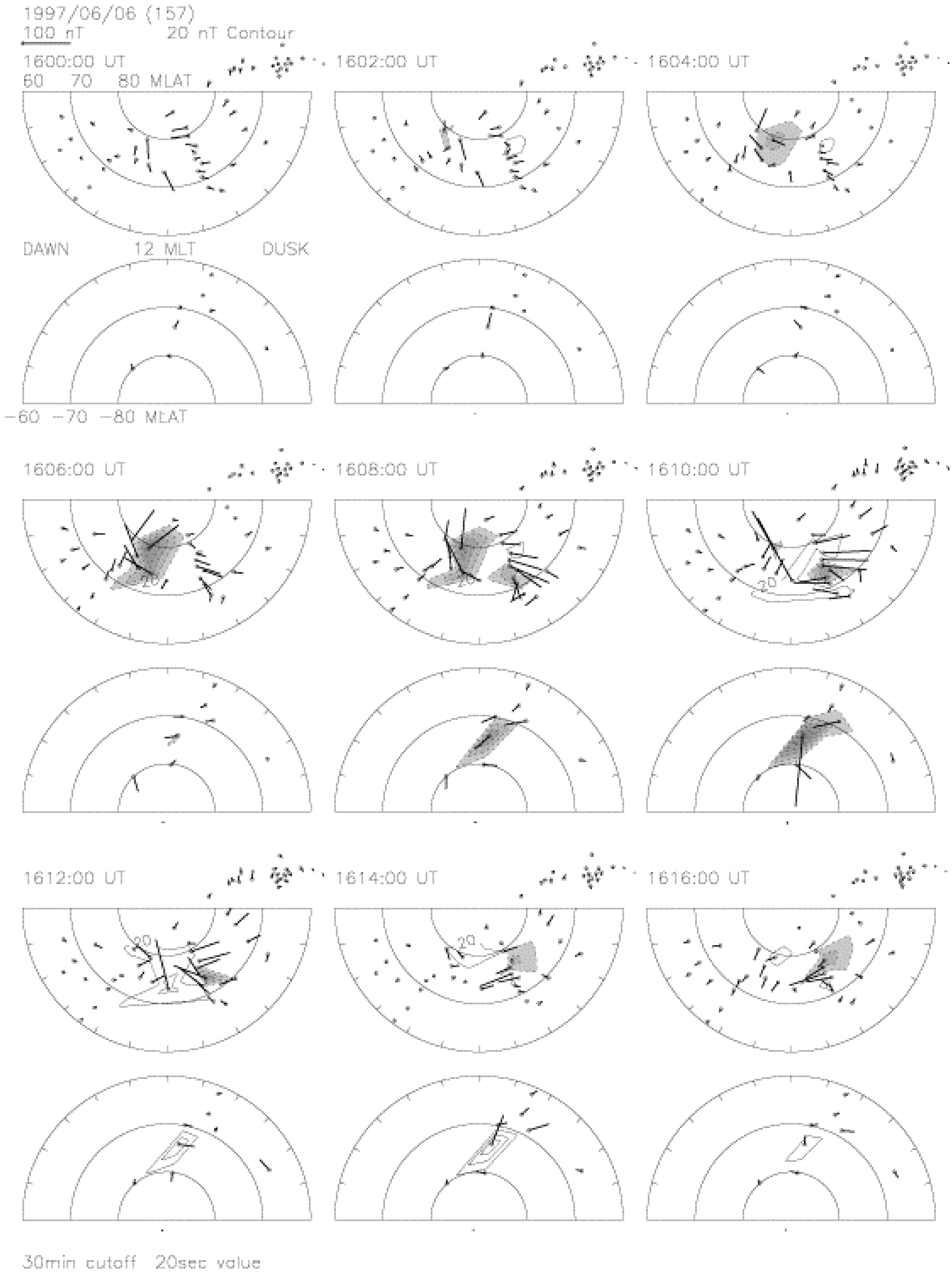

Figure 3-5. Equivalent convection plots for all magnetometer stations at 2 min intervals beginning at 1600 UT. A pair of downward and upward semicircles shows the patterns for the northern and southern hemisphere, respectively. The magnitude and direction of change of the Z component are also plotted by superposed contour.

The two dimensional convection patterns at 2 min intervals (shown looking down, onto the ionosphere, in both hemispheres) are shown in Figure 3-5 in CGM coordinates. The lengths of the convection arrows are expressed in nT (as that is the unit measured, even though the geomagnetic vectors in the horizontal plane have been rotated by 90° to provide the convection directions) but are proportional to the convection velocities. The vertical component variations at each minute are indicated by the superposed contour. A standard Delaunay triangulation and bilinear interpolation (IDL Software Package, Research Systems, Inc., Boulder, Colorado, 1995) of the very unevenly distributed data set is performed before making these contour plots. Negative contours are shaded to make them more conspicuous. The contour interval is 20 nT and zero line is removed. Convection patterns are shown at 2 min intervals from 1600 UT to 1616 UT during which the largest amplitude of the MIE was observed.

Beginning at 1602 UT in the northern hemisphere and at 1604 UT in the southern hemisphere, the convection arrows become large enough to indicate a tendency for clockwise rotation in the north and a tendency for counter-clockwise rotation in the south, respectively. At the same time, there is a slight movement of the patterns toward the east in both hemispheres. The vertical component is negative in both hemispheres over the MACCS and the southern stations (as is also shown in Figure 3-3). This negative Z component together with the clockwise rotations in the north and counterclockwise rotations in the south are consistent with field aligned currents out of the ionosphere in both hemispheres (e.g., *Lanzerotti et al.* [1991]).

3.4 Aurora and CNA data analysis

Available optical data acquired in the Antarctic near the dayside auroral oval were investigated. Optical data (630.0 nm and 427.8 nm) were available from MM (Arrival Heights installation by the University of Newcastle, Australia) and at South Pole. The atmosphere over the only operating AGO all-sky imager at P1 was clouded out. Shown in Figure 3-6 are 630.0 nm all sky images in geomagnetic coordinates of MM and SP for the interval 1556 UT (top left) to 1624 UT (bottom right). The images are shown at two minute interval from top to bottom and left to right.

An aurora aligned in the geomagnetic east-west direction was observed in the MM image at 1556 UT. This aurora began to move westward at 1558 UT. The auroral intensity suddenly enhanced at the MIE onset at 1600 UT and then the aurora was split at 1602 UT. The portion of the aurora moved westward (see MM image at 1604 UT), while the eastern portion moved eastward and disappeared from the MM image at 1606 UT. Instead of it, the SP image shows auroral brightening after 1606 UT. This aurora moved eastward with a speed of 1-3 km/sec until the aurora became diffuse at 1614 UT. At 1616 UT an arc structure aligned in the longitudinal direction detached from the bulk of the aurora and moved equatorward. The formation of an arc structure is more evident in background subtracted images (not shown here). The auroral arc stopped around -74° MLAT and brightened at 1619 UT, and then decayed. The discrete arc observed at 1606 UT may indicate that the MIE vortex is strongly related to the LLBL rather than the CPS. There was little signal at 427.8 nm at either of these sites indicating precipitation of low energy electrons.

The precipitation of low energy electrons is further confirmed by an investigation of the imaging riometer data from MM, P1, P2, and SP. If there is a sufficient flux of higher energy electron precipitation, the D-region ionization will be enhanced inducing strong cosmic noise absorption (CNA) in riometer signals. There was no significant CNA at MM, P1, and P2 during the MIE. Data obtained from the imaging riometer at SP are shown in Figure 3-7.

Although the absorption maximum is very small (< 0.13 dB), the CNA data show evidence for clear eastward movement of the signal beginning at ~1609 UT. This motion is essentially consistent with the movement of the 630.0 nm emissions seen in Figure 3-6.

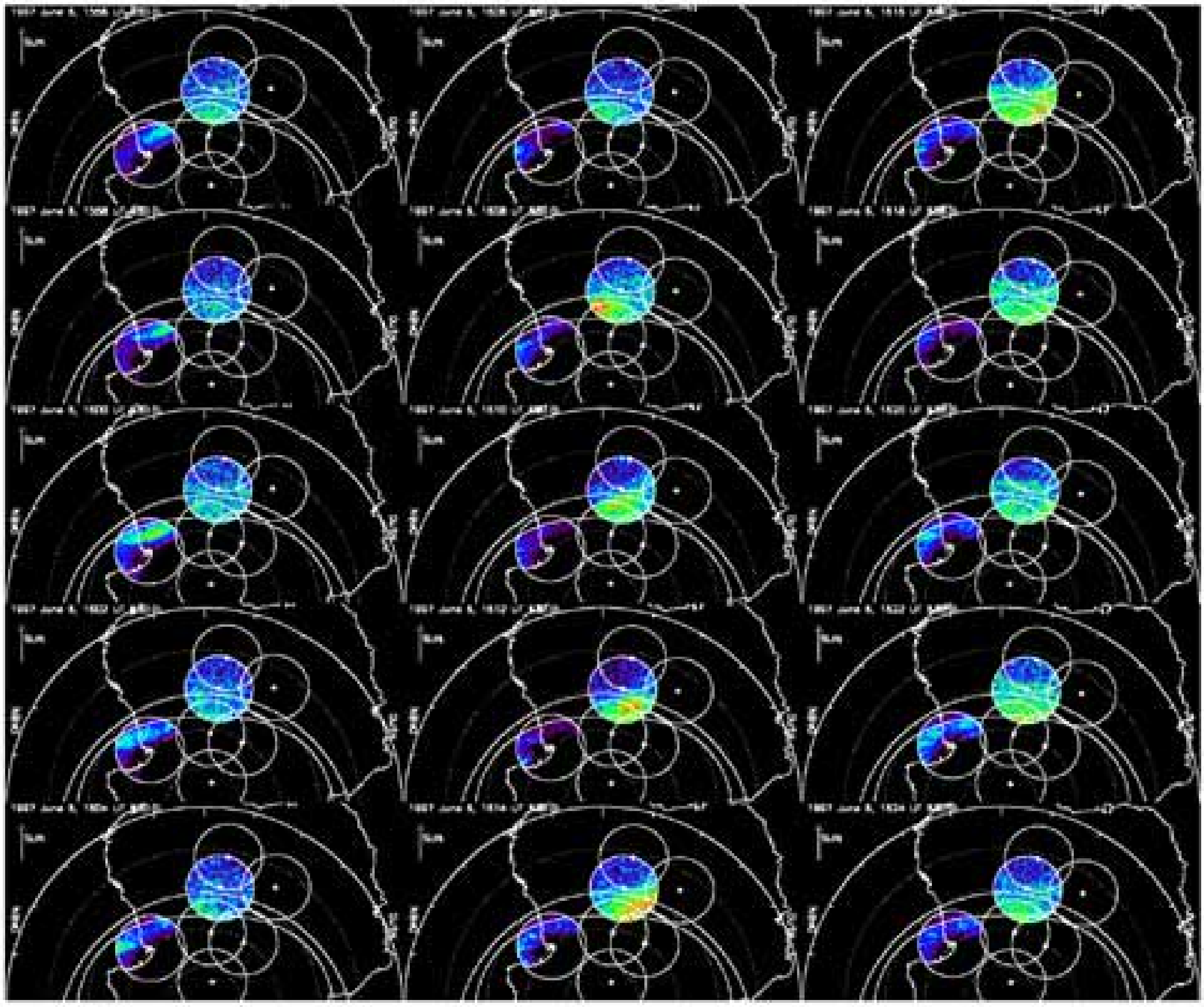

Figure 3-6. All sky images (geomagnetic coordinates) of the 630.0 nm emissions seen overhead at MM and SP at two min intervals from 1556 UT (top left images) to 1624 UT (bottom right image). The fields of view of all stations are shown, as is an outline of a portion of the Antarctic continent. Local noon is at the top of all panels: west is left and east is right in this view looking down onto the Earth.

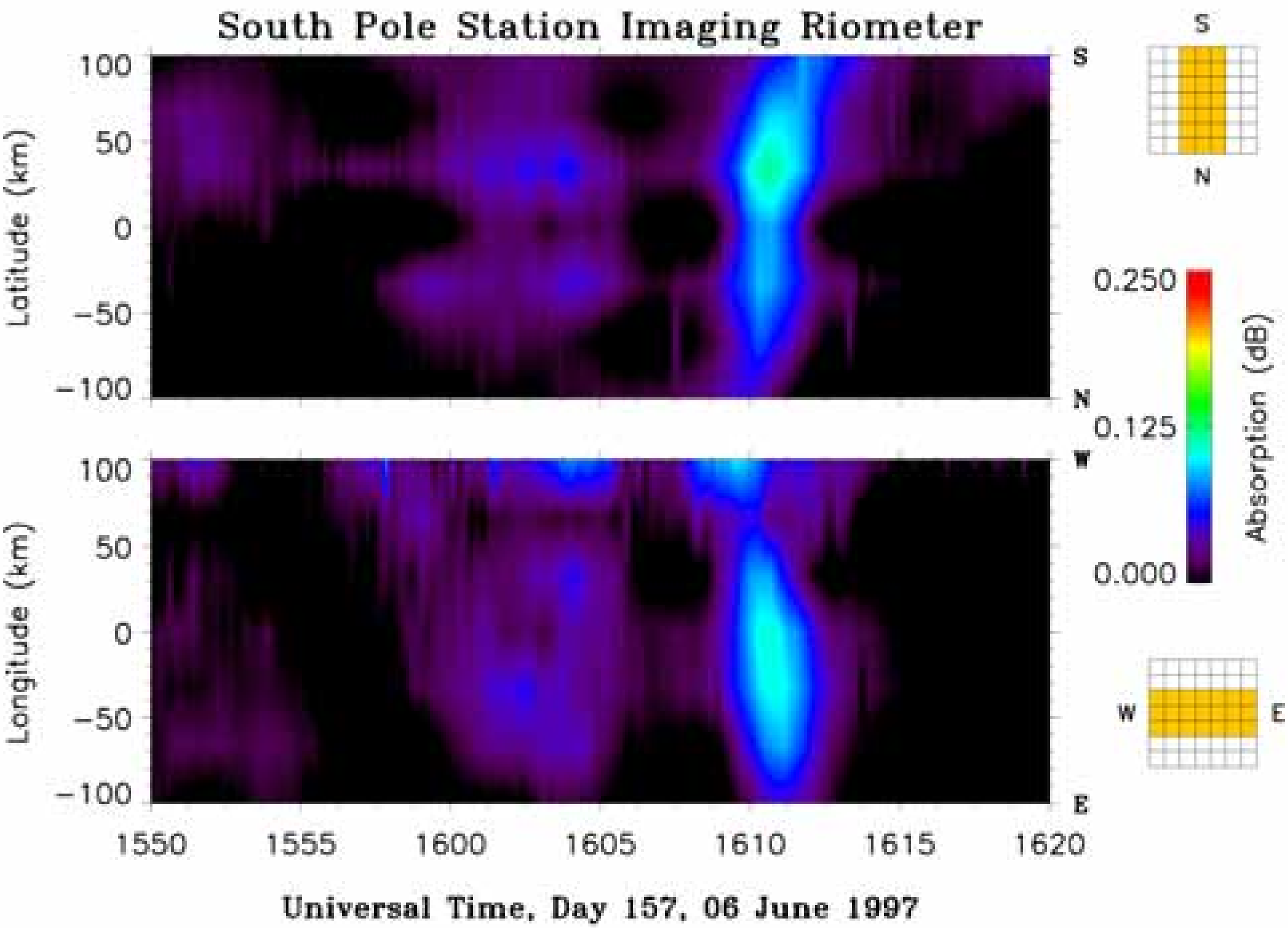

Figure 3-7. Display of riometer absorption in the geomagnetic south-north (upper panel) and east-west (lower panel) directions from the 49 element imaging riometer at SP in the time interval 1550–1620 UT on June 6, 1997.

3.5 HF radar data analysis

The Super DARN radars observed almost no backscatter corresponding to this event in either the north or the south, except for a preexisting stable region of irregularity depicted in grayscale area in Figure 3-8. Pre-existing radar scatter was seen in the Sanae and Halley radar fields-of-view. At the time of the MIE, the backscattered power in the pre-existing HF radar scatter region was intensified, suggesting that the MIE current system more intense ionospheric irregularities.

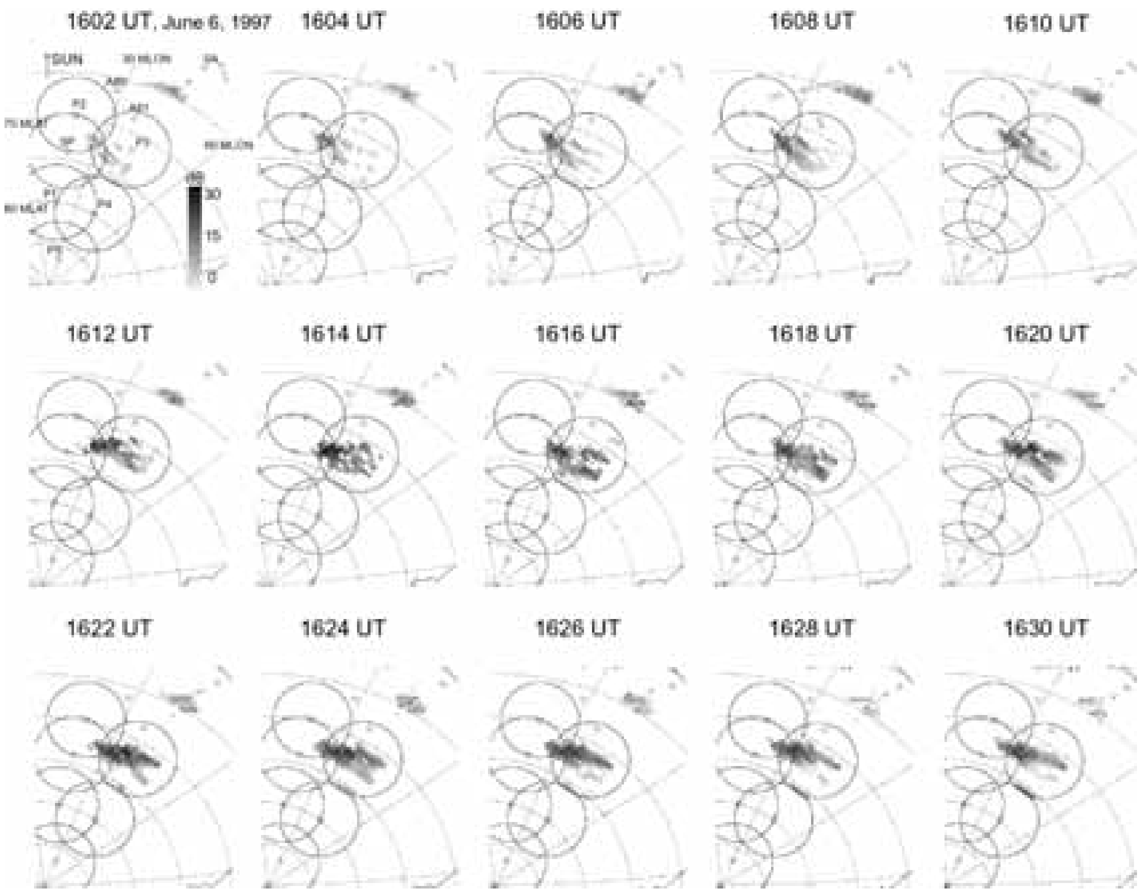

Figure 3-8. HF radar backscatter power observed at Sanae in Antarctica for the interval 1602-1630 UT on June 6, 1997. The fields-of-view of all-sky cameras are also depicted.

Figure 3-8 shows the spectral power of backscatter observed by the Sanae (SA) radar at two min intervals. The grayscale area is mapped onto the 300 km altitude (typical altitude for F region backscatter). Circles are the fields-of-view of the all-sky imagers (same as Figure 3-6) and are shown as a guide for the relative locations.

The backscatter power was enhanced when the MIE approached the backscatter region and passed through it. At 1614 UT, when the MIE-related aurora reached the backscatter region, the peak power was measured at the western edge of the backscatter. The enhancement of the irregularity gradually faded out, lasting until ~1700 UT. The Halley (HB) radar also observed backscatter similar to that of the Sanae radar.

The Sanae radar data shows a very pronounced increase in the Doppler spectral width (the full width of the Doppler spectra at half power) as the vortex passes though the irregularity region (Figure 3-9). The Doppler spectral width is a measure of the variation of the electric field in both the spatial domain (the radar sampling cell, typically 45 km by 100 km in dimension) and the time domain (variations occurring during the radar integration time, which was 7 sec). A large increase of the spectral width indices that the electric field is varying rapidly in one or both of these two domains.

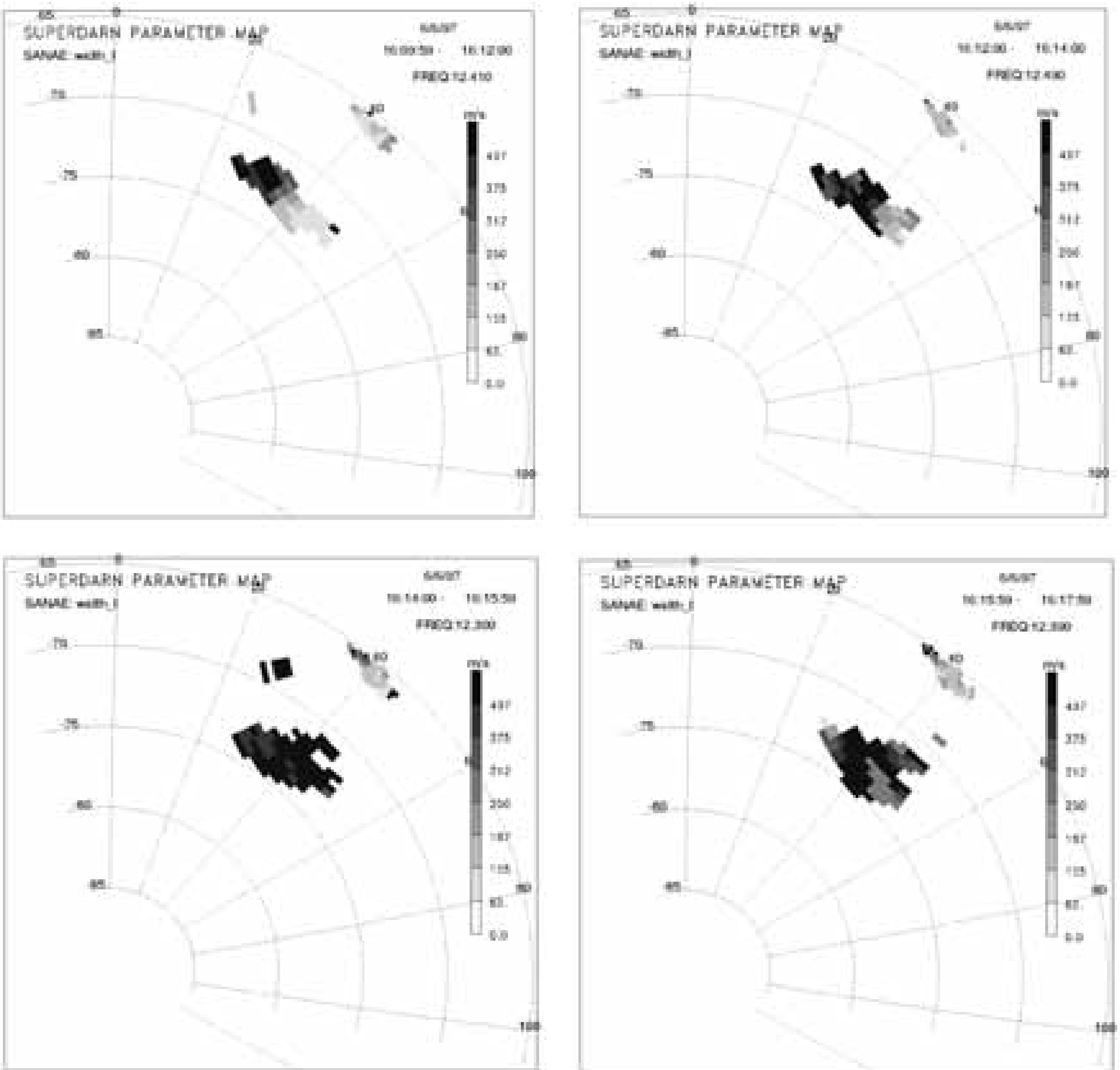

Figure 3-9. Variation of the Doppler spectral width observed at Sanae between 1610 and 1618 UT on June 6, 1997.

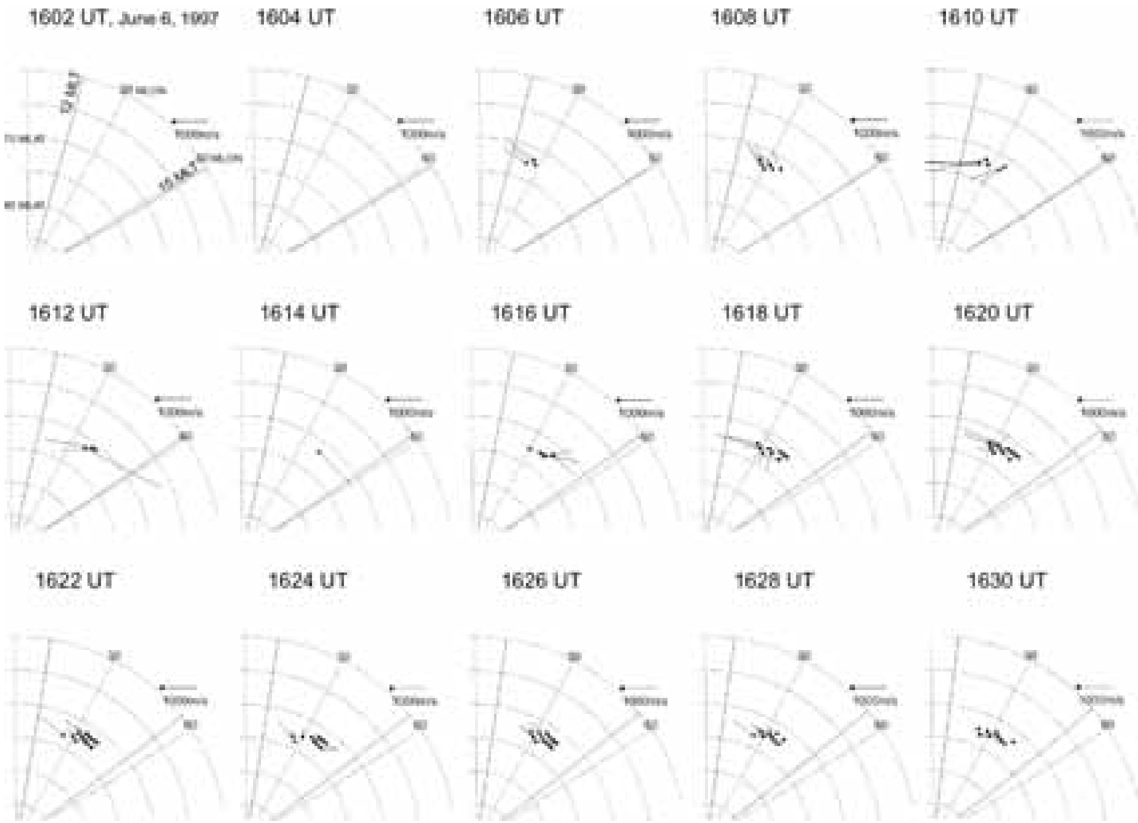

Figure 3-10. Two dimensional convection velocities derived from the merging method of line-of-sight Doppler velocities observed by twin radars, SA and HB, for the interval from 1602 to 1630 UT on June 6, 1997.

The convection patterns derived from the radar data for the time interval 1602 UT to 1630 UT at 2 min intervals are shown in Figure 3-10. The two-dimensional convection velocities are calculated by the vector addition of two line-of-sight Doppler velocities in the overlapped backscatter region. A strict threshold is used in order to provide reliable vector velocities: Minimum power is 3.0 dB, minimum velocity is 25 m/sec, maximum velocity is 3000 m/sec, and maximum error on velocity is 100 m/s.

The convection velocities in Figure 3-10 show that the characteristic change of the convection velocity began at ~1606 UT. No merged vectors were available in the field-of-view for the previous two panels at 1602 and 1604 UT. The plasma flows showed a similar rotation as the convection arrows at SP in Figure 3-5. However, there is ~2 min time lag between the SP geomagnetic signature and the HF radar signature. The convection arrows obtained from the HF radar data are located approximately two degrees equatorward and 10-15 degrees eastward of SP station. The merged region moved eastward across the 30° geomagnetic meridian line. The convection velocity was enhanced to ~2400 m/sec at 1612 UT. All of these signatures are consistent with the passage of the low-latitude portion of the MIE.

3.6 Interplanetary data analysis

Shown in Figure 3-11 are the solar wind velocity, dynamic pressure, and interplanetary magnetic field (GSM coordinates) as measured on IMP-8 (see Figure 3-2c) for the interval, 1300-1700 UT around the MIE. The magnetic field data and its variations as measured on Interball-Tail are also shown in Figure 3-11 by dotted lines. The IMF values are ~1 min values for IMP-8 and 2 min average for Interball. The solar wind data in the bottom lower three panels are displayed at ~90 sec resolution.

There are several ways to estimate a period of time for which the interplanetary magnetic feature propagates from the position of the satellite to the bow shock or the magnetopause. The most straightforward estimate is to assume that the magnetic feature is contained in a plane oriented parallel to the Y-axis. Using the solar wind velocity and the spacecraft x position, a simple estimate of the propagation time can be determined. Assuming that the subsolar bow shock and magnetopause are located at 14.5 R_E and 11.0 R_E, respectively, as depicted in Figure 3-2c, and the solar wind velocity Vsw is 400 km/sec, this estimation results in a 13 min delay from IMP-8 to the subsolar magnetopause and a 11 min delay from Interball-Tail to the magnetopause. Here we assumed that the propagation velocity in the magnetosheath Vsh = Vsw/8. Note that this implies that the propagation time from IMP-8 to Interball-Tail is about 2 min, a time somewhat shorter than the observed time delay in Figure 3-11. Therefore, this simple estimation method should be improved.

The above method is not valid when the satellites are substantially off the sun-earth line and the orientation of the interplanetary structure is not perpendicular to the solar wind flow direction. For this MIE, since the vector from IMP-8 to Interball-Tail points near the bow shock nose and two satellites observed almost identical signatures, we could estimate the propagation time from the satellites to the bow shock more accurately. There are two distinguished discontinuities which have a possibility of triggering the MIE, i.e., a large cone angle change at 1508 UT on IMP-8 and a rapid southward turning at 1516 UT on IMP-8. The locations of IMP-8 and Interball-Tail were GSE (x, y, z) = (34.2, -10.9, 10.0) and GSE (x, y, z) = (25.6, -7.2, 6.4) at 1510 UT, respectively.

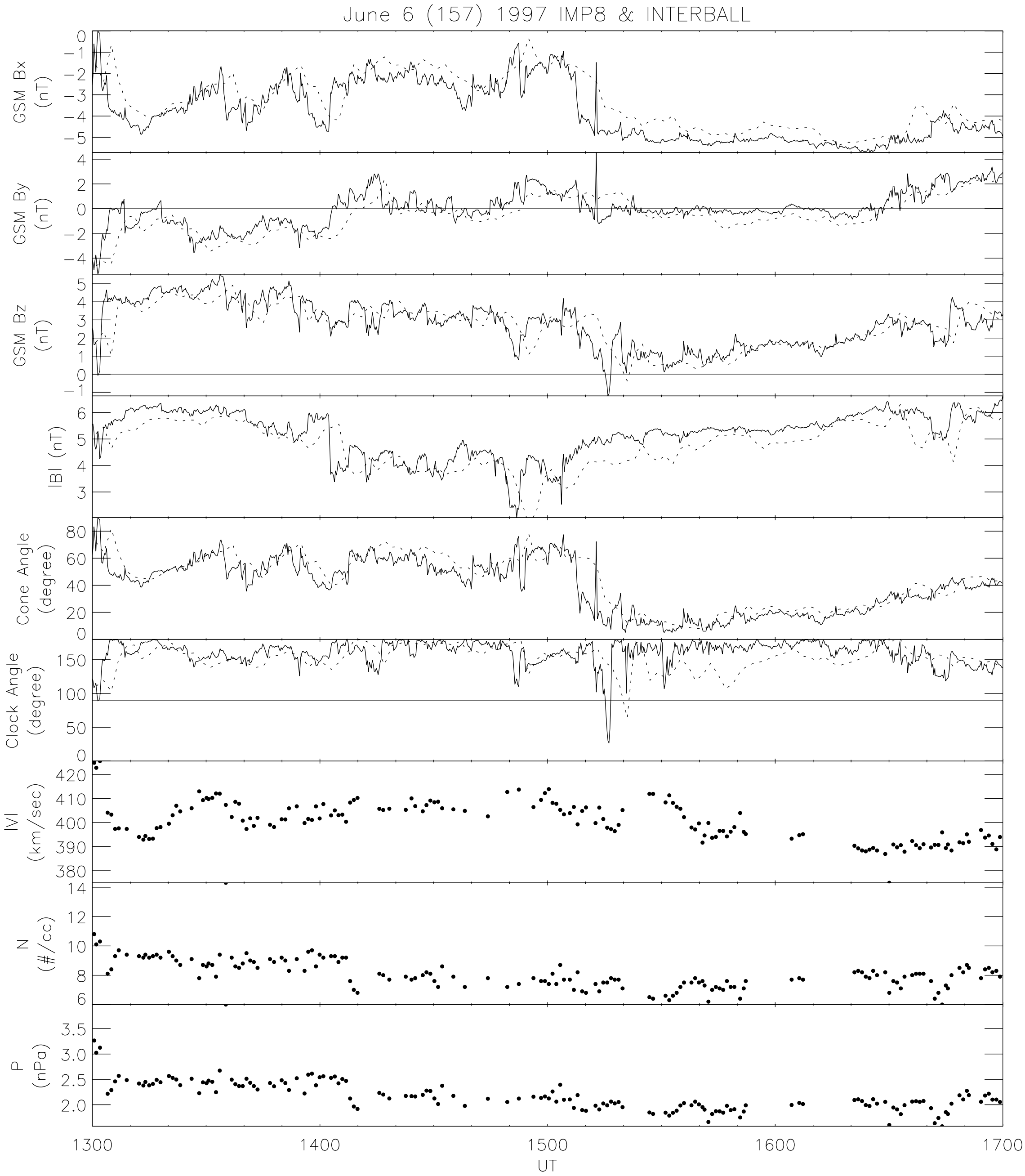

Figure 3-11. Interplanetary data from the IMP-8 and Interball-Tail spacecraft for the interval 1300-1700 UT on June 6, 1997. From the top panel to the bottom panel, the figure contains the interplanetary magnetic field (IMF) B_X, B_Y, and B_Z component magnitudes (in nT and GSM coordinates), the total field strength B (nT), the cone angle and the clock angle of IMF (in degrees), the solar wind speed |V| (km/sec), plasma ion number density n (/cc), and dynamic pressure P (nPa). The Interball-Tail magnetic field data are shown by dotted lines in the top six panels.

Since the time lag between IMP-8 and Interball-Tail was ~7 min for the cone angle change, it takes ~9 min to propagate from Interball-Tail to GSE (x, y, z) = (15.0, -2.6, 2.0), near the nose point of the bow shock along the line from IMP8 to Interball-Tail. In the same way, since the time lag between IMP-8 and Interball-Tail was ~5 min for the southward turning, it takes ~6 min propagation time from Interball-Tail to the point GSE (x, y, z) = (15.0, -2.6, 2.0). If we consider the transmission time from the bow shock to the magnetopause to be as ~6 min, these discontinuities reached near the magnetopause nose at the time from 1524 to 1527 UT. Thus it is concluded that these discontinuities are not the direct trigger of the beginning of the MIE at ~1600 UT. After the passing of these two discontinuities, probably including the MIE interval, the IMF had a large X-component (~ -4 to -5 nT), almost zero Y-component and a small positive Z-component. Thus, the IMF was nearly radially aligned during this time with a cone angle of less than 20° (see the fifth panel from the top in Figure 3-11). There were only small fluctuations in the solar wind velocity (which was low, ~400 km/s) and in the dynamic pressure throughout the four hour interval shown in Figure 3-11. The data from Wind and Geotail satellites are not shown here because these satellites located on the far duskside apart from the sun-earth line, which is not appropriate to the discussion of the MIE generation mechanism. In summary, the solar wind data obtained from the IMP-8 and Interball-Tail spacecraft do not show any signatures on the direct triggering of the MIE.

3.7 Discussions

In sections 3.1-3.5, we have shown the ground signatures of the MIE on June 6, 1997 using the data on geomagnetic variation, aurora, particle precipitation, cosmic noise absorption, and HF radar backscatter. The geomagnetic data obtained from magnetometer networks covering the major part of both northern and southern polar regions showed that electrical currents directed out of both south and north ionospheres. The MIE was initiated in the prenoon local time region in both hemispheres as shown in Figure 3-12. The optical data in the Antarctic, as well as the geomagnetic data, showed that the MIE then moved eastward and equatorward across magnetic local noon. Investigation of the conditions in the interplanetary medium both near the Earth as well as further upstream showed that there were no significant changes in the dynamic pressure preceding or accompanying the event. The IMF was directed strongly radially outward from the sun and had a slightly positive (~1-2 nT) northward orientation in the GSE coordinate.

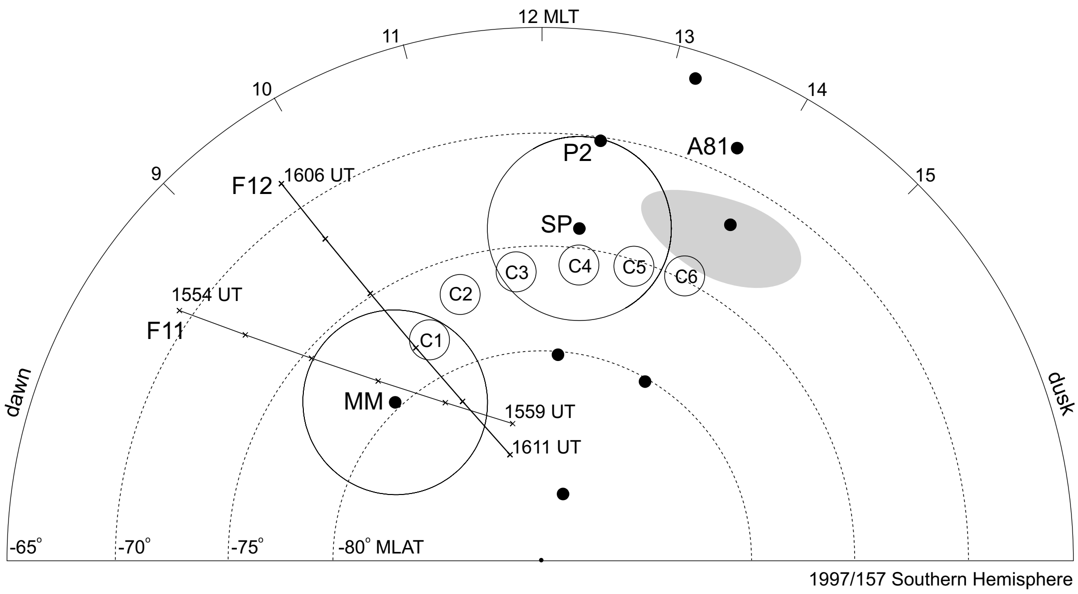

Figure 3-12. Schematic illustration of the MIE occurrence region and its movement on the geomagnetic polar map. The guiding centers of TCV derived from the horizontal perturbations are plotted as C1 to C6. The gray hatch indicate approximate backscatter region observed by twin HF radars in Antarctica. The tracks of DMSP F11 and F12 spacecraft across the southern hemisphere around the beginning and end of the MIE are also depicted.

A summary of the MIE accompanying a TCV is shown in Figure 3-12 as a polar map of the southern hemisphere. The symbols C1 to C6 in Figure 3-12 are the approximate guiding centers of the TCV at 2 min intervals from 1602 UT to 1612 UT. The approximate location of each center is inferred from the equivalent convection arrows in Figure 3-5. Although this method for the determination of the TCV center may not be as rigorous as using a model, we are simply interested in examining and comparing the gross features for the motion of the vortex. In this manner, the center is at first determined for the northern vortex; the center is then projected to the CGM conjugate points in the southern hemisphere. Since these conjugate points are also consistent with the location of the vortex observed in the southern hemisphere, it is concluded that there is a conjugacy in CGM coordinates in terms of the guiding center of the vortex.

The scale size and motion of the MIE/TCV can be further delineated by examining the timing and the amplitude of the vertical (Z) component observed in both hemispheres. The optical aurora data also provide information on the scale size and the motion of MIE.

The MIE had its earliest (~1607 UT), and approximately largest, Z-component amplitude (~150 nT) at IG (see Figure 3-3). A minute or two prior to this there was a small vertical deflection at MM (see Figure 3-1). Vertical variations were seen at almost the same time at RB and CH of the MACCS array. In the CANOPUS magnetometer chain located further west of the MACCS array, there were no vertical variations; the D-component variations that might be associated with the MIE were seen at the four most northern and eastern CANOPUS locations, CHU, ESK, RAN, and TAL. Some two minutes after the event at the western edge of the MACCS array, the largest vertical components were seen over SP at ~1609 UT in the Antarctica and at ATU and SKT on the western edge of Greenland. About one to two minutes later (~1611 UT), a large Z amplitude was seen over STF with riometer absorption in the region equatorward of STF. The MIE basically ended at about this time at ~1612 UT. Thus, the overall timing of the largest amplitude in the Z-component intensities followed but was ~3 min behind the timing of the guiding center motion that is depicted in Figure 3-12.

The motion and the current system of the MIE can be described overall by making reference to the all-sky imager, riometer, and HF radar data. A 630.0 nm auroral brightening at 1600 UT and subsequent splitting into the western and eastern portions at ~ -78° MLAT were observed in the prenoon sector (~10 MLT) and the eastward moving aurora decayed at about -75° MLAT in the afternoon sector (~14 MLT). The split indicate that there was strong shear in the convection pattern at the initiation of MIE. This may imply that the MIE had its origin near the convection reversal boundary. The MIE-related 630.0 nm aurora had a peak luminosity around C3 when the center of TCV was located near C4 at 1608 UT (cf. Figure 3-6). At 1610 UT, the all-sky imager at SP observed the brightest aurora just poleward of SP near C4, while the center of the vortex was located at C5 at this time. The 2 min time lag may indicate that the shape of the convection vortex was strongly deformed from the simple Hall current loop pattern with the filament of the upward field aligned current in the center of the loop.

The imaging riometer at SP observed CNA associated with this MIE. The eastward motion is clear in Figure 3-7. It almost corresponds to the motion of the 630.0 nm aurora. The absorption level is very low (< 0.13 dB) but still larger than the noise level (~0.05 dB) of the instrument. This CNA can not be considered as the effect of hard electron precipitation because there were no blue aurora in the wavelength of 427.8 nm at SP, which is caused by hard electron precipitation. The weak CNA without hard electron precipitation is interpreted by two mechanisms: heating of the electron temperature in the E region [cf. *Stauning*, 1984] and enhanced ionization in the F region patches [cf. *Rosenberg et al.*, 1993]. The F region ionization scenario might be more consistent with the 630.0 nm optical observations which show an enhancement at the time of the MIE not accompanied by a corresponding enhancement in 427.8 nm. The 630.0 nm aurora is usually emitted at F region altitudes. Although the aurora related to the June 6, 1997 MIE would not be a patch in the same sense as in the cases of *Rosenberg et al.* [1993], a different mechanism, perhaps related to local soft electron precipitation, would have to form the F-region electron density enhancement.

Pc 1 bursts were observed almost simultaneously at 1606 UT (Figure 3-4b) at three stations (SP, P2, A81) located near the low-latitude edge of the vortex when the center of the vortex was at local magnetic noon. The Pc 1 bursts have distinct peaks at around 0.2-0.3 Hz and are distinguished from Pi 1 bursts that are likely to be produced by strong particle precipitation. There are two possibilities of the generation mechanisms of Pc 1 emission.

At the onset of the Pc 1 burst ~ 1606 UT, AGO P2 in the Antarctic began to observe the sharp negative deflection of Z component (Figure 3-1). The footprint of P2 mapped to the equatorial plane in the magnetosphere with the T96_01 geomagnetic field model [*Tsyganenko and Stern*, 1996] is ~6 R_E near the sun-earth line. Considering that the sub-solar point is the point where the ring current region is closest to the magnetopause, the compression waves induced by MIE vortex might propagate into the dayside ring-current region (L ~ 6) and cause a burst of ion-cyclotron wave. On the other hand, it is also possible that the source region of the ion-cyclotron wave located in more high-latitude magnetospheric boundary region, such as LLBL. The field-aligned ducting of ion-cyclotron waves would not be complete and thus these waves might be measured at ground stations with some extended horizontal distribution, as observed at both SP and P2. Recently, *Fukunishi et al.*, [submitted to Advanced Space Research, 2000] reported the latter kind of MIE-related Pc 1 emission generated in the LLBL at the timing of a hot flow anomaly event on July 24, 1996. The abrupt deformation of the magnetopause could result in this kind of Pc1 generation.

The particle data of the low altitude DMSP spacecraft passing over the southern hemisphere were examined to determine the locations of various high latitude features. During the time closest to the MIE, most passes were over the southern hemisphere and are therefore the most relevant to this discussion. In particular, the passes of DMSP F11 and F12 over the Antarctic are the closest in time to the MIE. Figure 3-13a shows that DMSP F11 observed low latitude boundary layer (LLBL) precipitation from -77° to -80° MLAT as it passed over the 630.0 nm aurora seen in the MM image in the interval of 1557 to 1558 UT. Since the particle signature does not have a clear LLBL/mantle boundary, we could not specify the precise poleward boundary of the LLBL. However, considering the drop off of the highest energy ions and the sharp drop in the ion fluxes at lower energies (although they briefly recovered), the boundary is possibly at ~ -80° MLAT. The ion and electron energies and flux intensities in the region beyond -80° MLAT are consistent with the characteristics of the mantle. The 630.0 nm optical data from MM (see Figure 3-6) also shows a sharp boundary of the emissions at ~ -80° MLAT.

DMSP F12 (see Figure 3-13b) observed a clear mantle/LLBL boundary; i.e., open/close boundary, at ~ -79° MLAT and ~9.7 MLT at ~1609:30 UT. It is apparent from Figure 3-6 that this open/close boundary also corresponded to the poleward boundary of the 630.0 nm aurora. Actually, the auroral emission region moved slightly equatorward as the event moved eastward. From the discussion above and making reference to Figure 3-12, it is concluded that the MIE was initiated in the LLBL.

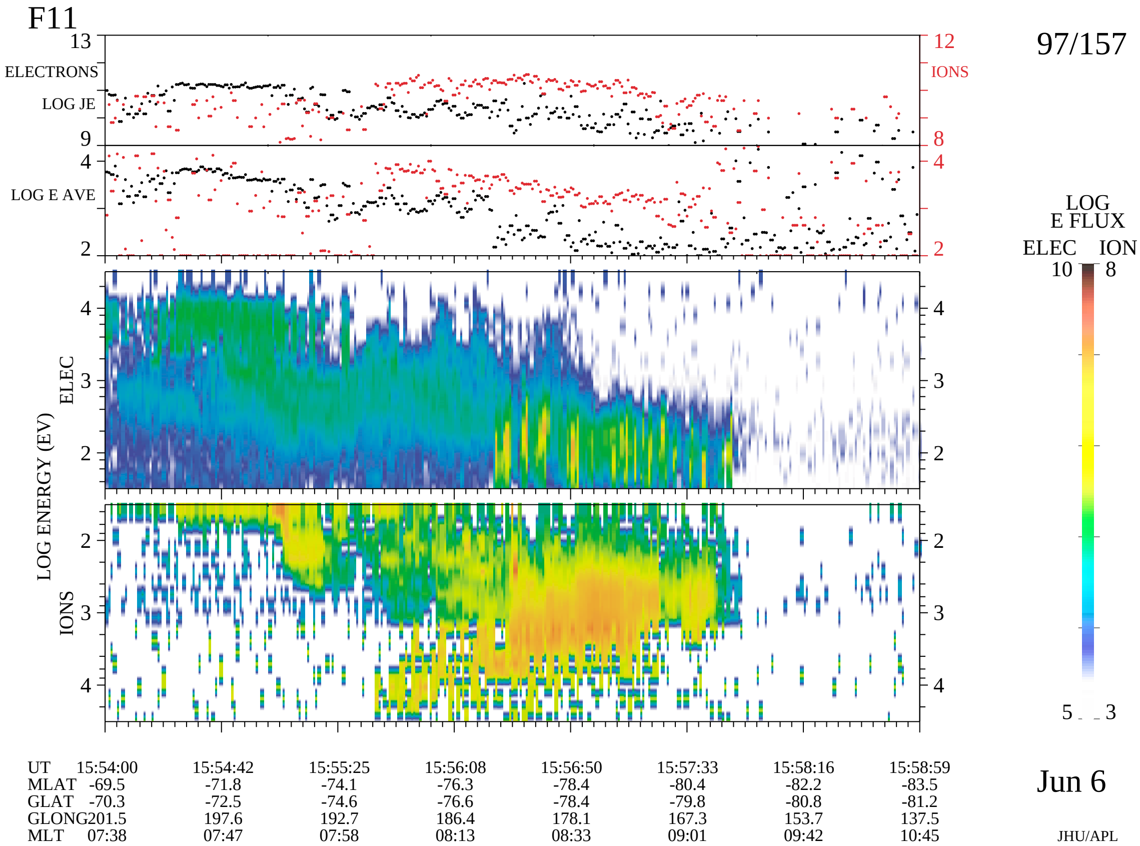

Figure 3-13a. DMSP F11 energy-time spectrograms for the interval from 1554 UT to 1559 UT. The spectrograms show differential energy fluxes of electrons (middle) and ions (bottom) from 32 eV to 30 keV in units of eV/(cm^2·s·sr·eV). The top two panels show the total energy flux (eV/cm^2·s·sr) and the average energy (eV) of electrons (black dots) and ions (red dots). Note that the ion energy scale is inverted.

A further magnetospheric manifestation was studied by examining magnetic field signals measured at geosynchronous (GEO) orbit on two GOES satellites that were in the western hemisphere sector. Shown in Figure 3-14 is the geosynchronous magnetic field measured at GOES-8 and GOES-9. The locations of these spacecraft are shown in Figure 3-2c for 1300 UT to 1700 UT on June 6, 1997. Magnetic field fluctuations with several nT amplitudes are evident at both GOES locations throughout the interval plotted. A nearly 4 nT excursion at GOES-8 (the spacecraft closest to the SP at 12.5 MLT) occurs at approximately the same time as the MIE. It is reasonable to hypothesize that this signal was a magnetospheric manifestation of the MIE that was measured at the geosynchronous orbit. A similar excursion was measured in the GOES-9 field, ~5min earlier than at GOES-8. This earlier perturbation of the GOES-9 magnetic field may be associated with the initiation of the MIE. If so, then the MIE would have originated closer to the dawn flank of the magnetosphere.

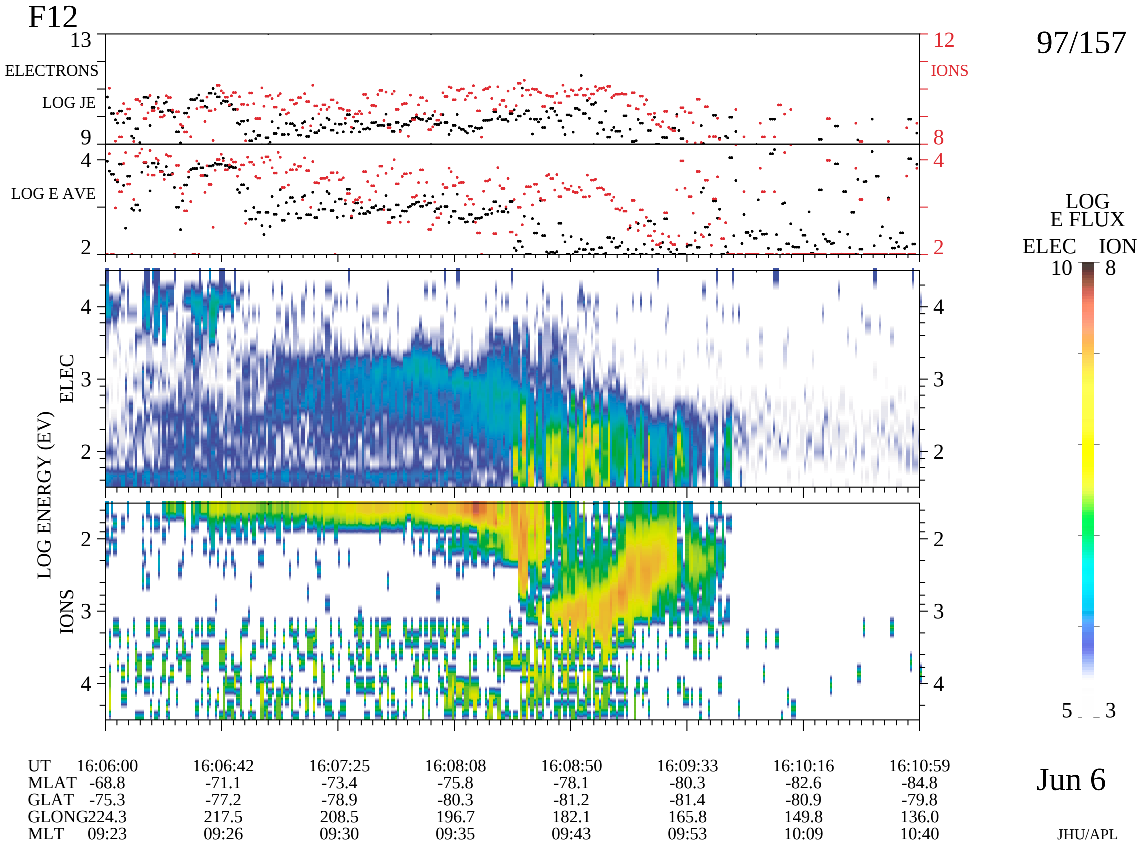

Figure 3-13b. DMSP F12 energy-time spectrograms for the interval from 1606 UT to 1611 UT. Notation is the same as Figure 3-13a.

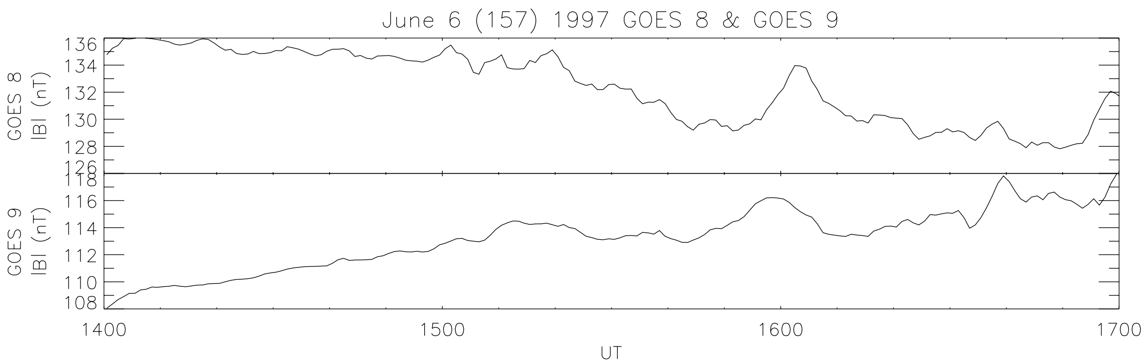

Figure 3-14. Geomagnetic field variations observed at GOES-8 (upper panel) and GOES-9 (lower panel) on June 6, 1997.

There is no evidence in the interplanetary data (Figure 3-11) for abrupt changes in the solar wind dynamic pressure or in the IMF that might be a trigger of the MIE. The IMF was directed strongly outward from the sun (B_X = -5 nT) and had a slightly positive (1-2 nT) B_Z orientation and nearly zero B_Y in the GSM coordinates. There are significant pieces of evidence against the classical model of dayside reconnection, pressure pulse, impulsive penetration, and Kelvin-Helmholtz instability. For example, positive IMF B_Z condition excludes the dayside reconnection model. The eastward (toward dusk) motion of TCVs is clearly opposite direction to the predicted propagation direction from impulsive penetration or Kelvin-Helmholtz instability. No abrupt changes in the solar wind dynamic pressure exclude the pressure pulse mechanism.

The interaction between the bow shock and the solar wind may be the point. Some pressure variations incident on the magnetopause could be generated in the foreshock region. The nearly radial IMF direction makes quasi-parallel shock (QPS) structure. In such QPS condition, since the foreshock region expands into the large area, it is reasonable to hypothesize that the pressure pulses may be produced in the expanded foreshock region via the interaction between the solar wind and upstream ions. Strong Pc3 geomagnetic activity at the MIE interval may be also related to the QPS condition. It is known that the magnetosheath enters a very disturbed state during QPS conditions [e.g., *Schwartz and Burgess*, 1991] and there could be rapid pressure variations in the magnetosheath.

Therefore, it is speculated that the abrupt cone angle change from 60° to 20° may be the indirect trigger of the MIE on June 6, 1997 via the rapid change of the foreshock geometry 20-30 min in advance the MIE onset timing. *Lin et al.* [1996] presented a two dimensional simulation of the interaction of the IMF orientation changes with the bow shock and found that pressure pulses that propagate inside the magnetosheath toward the magnetopause are generated from this interaction. However, even by such pressure pulse mechanism, it seems still unclear how to explain the eastward motion of TCVs across the noon meridian. The sunward motion should be basically opposite direction to the predicted direction from the pressure pulse models. Furthermore, it still remains the extrinsic question; how the clearly impulsive, no continuous, and no turbulent characteristics of the MIE phenomena produced in such turbulent conditions? It seems that there are still no models that can readily explain all of the discussed MIE signatures in a unified fashion.

Chapter 4

A multi event study of MIEs

4.1 Selection of MIEs

A multi event study of MIEs is executed by the methods similar to those used in Chapter 3. Austral winter periods from April to August in 1998 and 1999 were selected for the multi event study. There are several reasons why these periods were selected. The austral winter season from April to August is suitable because one of the targets of this thesis is to investigate the dayside auroral activity related to MIEs. The period from 1998 to 1999 has also some advantages in making a collection of other data. The most important advantage is the ACE solar wind data are available during this period. The ACE spacecraft was launched on August 25, 1997. From its orbit around the Sun-Earth libration point ~1.5 million km (~235 Re) sunward of the Earth, ACE has provided continuous real-time solar wind measurements. ACE as well as Wind, IMP-8, Interball-Tail, and/or Geotail observations make it possible to determine the more accurate propagation time of the solar wind feature by calculating the discontinuity plane which seems to be one of the triggering sources of MIEs. The all-sky imager of National Institute of Polar Research (NIPR-ASI) at SP is also available from the 1997 austral winter season. The simultaneous optical observations of NIPR-ASI and the AGO all-sky imager network including SP and MM imagers make it possible to investigate the further detailed structures of auroral response to MIEs.

The LJL91 criteria of *Lanzerotti et al.* [1991] was first used to identify MIEs automatically using geomagnetic data at SP in the 1998/1999 austral winter. The LJL91 criteria select the events which satisfy the amplitude criteria ($\Delta V > 50$ nT; ΔH, $\Delta D > 40$ nT) and the duration criteria (their V deflections are greater by a factor of two than any other vertical deflection occurring in the 8 min preceding and succeeding data window).

Secondary, events with large amplitudes more than approximately 100 nT in the vertical magnetic component were selected by visual inspection. Events that could never be distinguished with background oscillations and/or Pc 5 pulsations were rejected by this inspection. Investigations of large amplitude events are useful since these events are not influenced by more complicated contaminations due to various origins. The vertical component data were used for this selection because the vertical component variations are more closely related to localized MIEs. For example, Alfvén wave activities would manifest themselves as continued activities in the horizontal component and the impulsive signatures would be reflected more directly in the vertical component. There is, however, a valid argument against it at least for the Greenland data. The Greenland magnetometer stations are all located close to the coast, which means that they are subject to the coastal induction effect. While we know from the case study on June 6, 1997 in the previous section, the vertical component is actually useful for mapping the vortex or field aligned current motion.

Finally, events were selected under two other conditions that solar wind abrupt changes occurred around the MIE timing considering the location of satellites and the solar wind velocity, and almost comprehensive ground- and space-based data sets are available. Now we know that MIEs are caused by various kinds of solar wind changes. The first step in order to understand and clarify the generation mechanism and evolution of MIEs is the investigation of MIEs which have clear origins in the solar wind.

Only nine events fulfilled all above conditions during the austral winter seasons in 1998 and 1999. Two more MIEs investigated by *Sibeck et al*. [1999] and *Mende et al*. [submitted to Journal of Geophysical Research, 2000] are also analyzed in the same way for references. These events are known as important examples in terms of the optical and CNA signature of MIEs. The final list of the MIEs is shown in Table 4-1. The set of MIEs are put in order of magnetic local time from morning toward evening. The Universal Time (UT) in Table 4-1 is basically the time automatically identified by the LJL91 criteria. Magnetic local noon at SP is 1535 UT. Three events out of the selected nine MIEs are actually caused by storm sudden commencement (SSC). The list of the SSC were obtained from Geo Forschungs Zentrum Potsdam website (http://www.gfz-potsdam.de/).

Table 4-1. Selected MIEs for the analysis of a multi event study.

Year	Date	UT	MLT at SP	Category
1996	July 24 (206)	1130	7.9	Dawn
1999	May 25 (145)	1223	8.8	Dawn
1996	May 22 (143)	1310	9.6	Dawn
1999	July 03 (184)	1550	12.2	Noon
1998	May 27 (147)	1609	12.6	Noon
1999	May 16 (136)	1721	13.8	Dusk
1999	May 25 (145)	1813	14.6	Dusk
1998	July 30 (211)	1902	15.4	Dusk
1999	July 06 (187)	1509	11.6	SSC
1998	May 03 (123)	1747	14.2	SSC
1998	June 13 (164)	1932	16.0	SSC

In the following four sections, the characteristics of MIEs are shown in detail for each of four convenience categories: 1) MIEs in the dawn sector (~8 - 10 MLT), 2) MIEs in the noon sector (~11 - 13 MLT), 3) MIEs in the dusk sector (~ 14 – 16 MLT), and 4) MIEs related to SSCs.

Summary plots of SP observation of each selected MIE in 1998 and 1999 are shown in Figure 4-1 and Figure 4-2, respectively. Solar wind parameters observed by WIND and/or ACE for six hours around the MIE interval are shown for all the listed events in Appendix. Key parameter data from the CDA web (http://cdaweb.gsfc.nasa.gov/) were used to make plots from numerous satellites such as Geotail, IMP-8, Interball-Tail, Wind, and ACE.

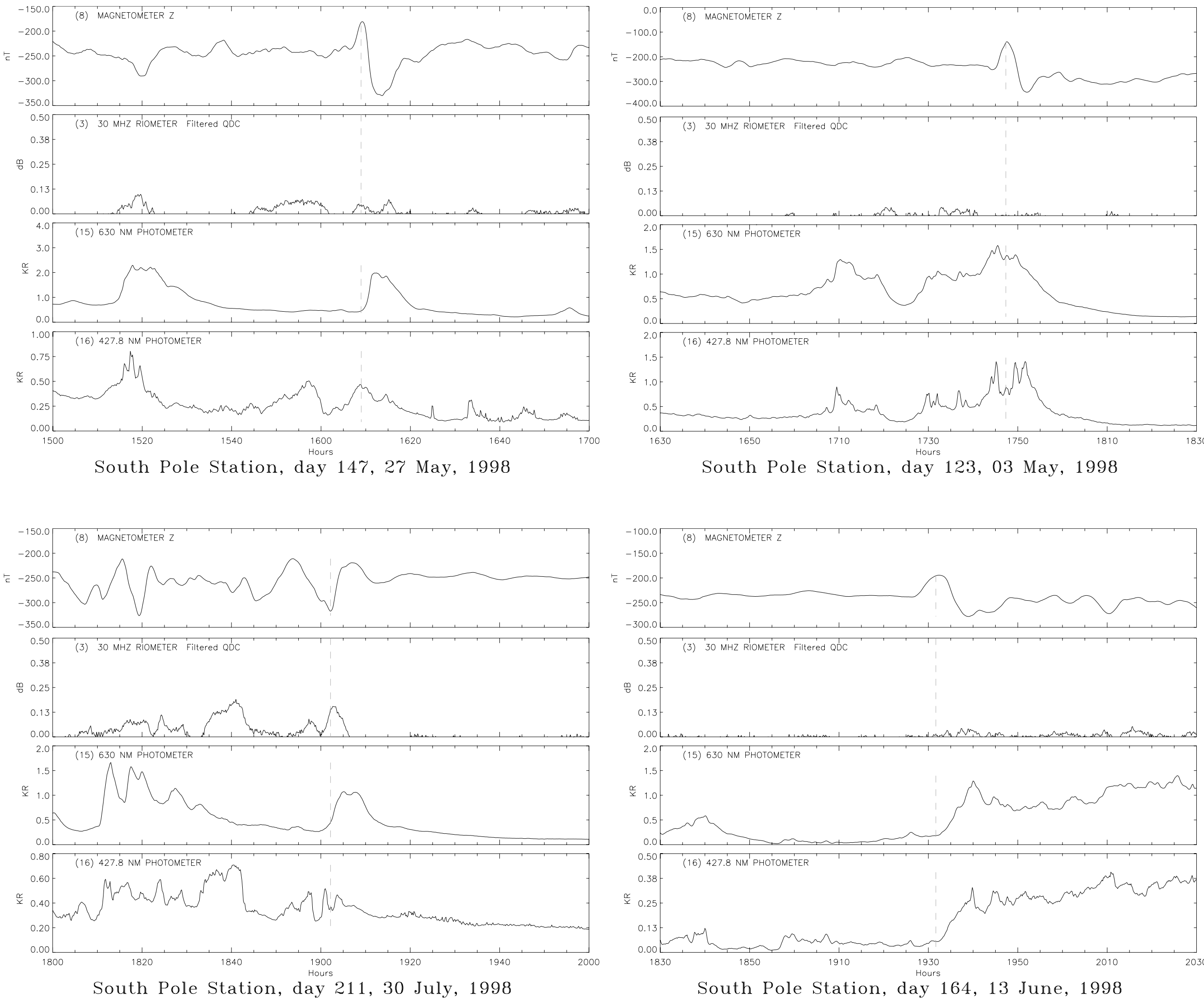

Figure 4-1. Summary plots of South Pole data for selected MIEs in 1998. From top to bottom, for each event, the figure contains the Z component magnitude in nT, cosmic noise absorption at 30 MHz, and emission intensities in the wavelength of 630.0 nm and 427.8 nm. The right two panels (May 3 and June 13, 1998) show the MIEs related to SSC.

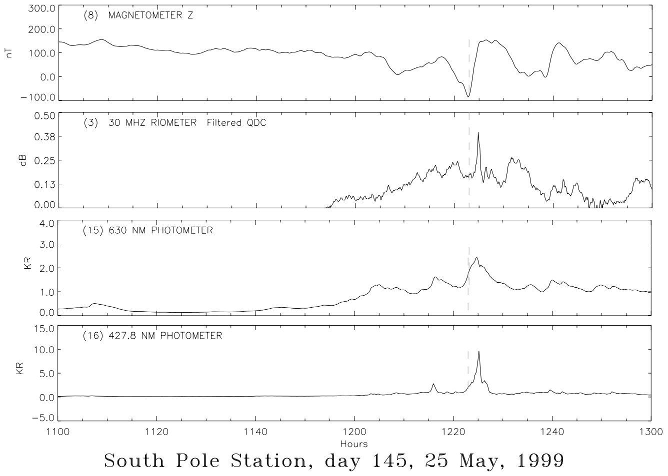

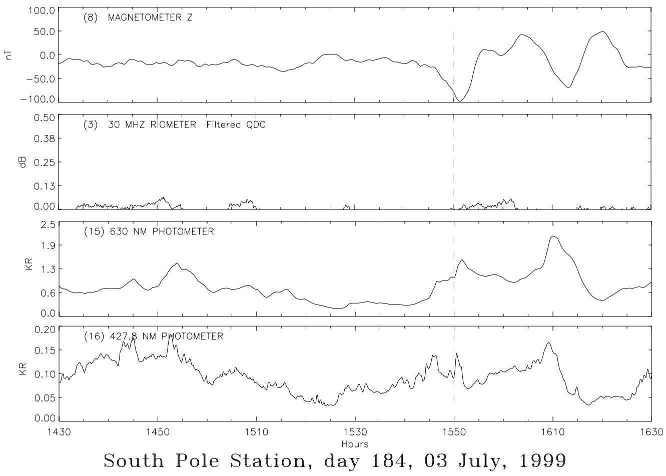

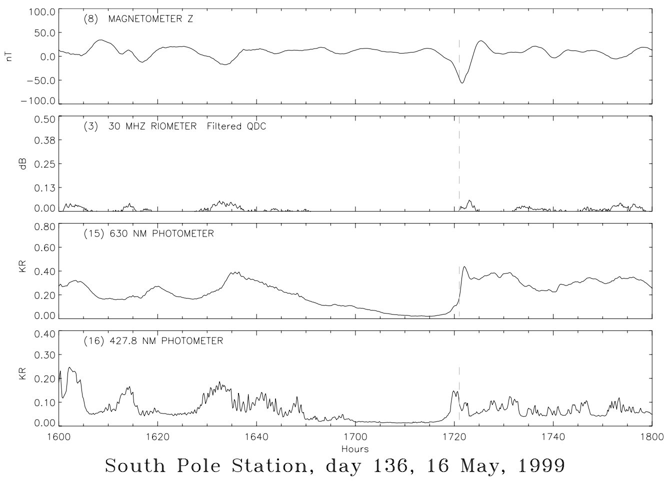

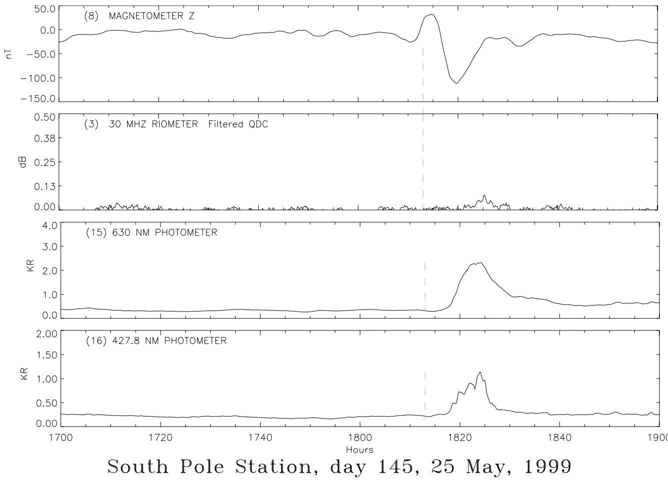

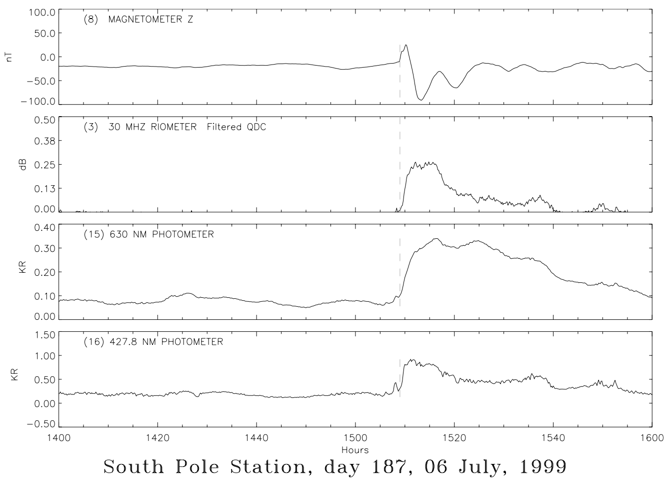

Figure 4-2. Summary plots of SP observation for selected MIEs in 1999. The format is the same as Figure 4-1. Left bottom panel (July 6, 1999) shows a MIE related to SSC.

4.2 MIEs in the dawn sector

We begin by comparing three MIEs observed at SP station in the dawn sector (~8-10 MLT). *Weatherwax et al.* [GEM 2000 poster session] showed two interesting MIEs in Figure 4-3 in terms of VLF signatures. In Figure 4-3, double pulse signatures in H-component traces are seen at 1133 and 1141 UT on July 24, 1996 (July-24 MIE) and at 1311 and 1323 UT on May 22, 1999 (May-22 MIE). Similar double pulse signatures in H-component traces are also seen at 1218 UT and 1231 UT on May 25, 1999 (May-25a MIE).

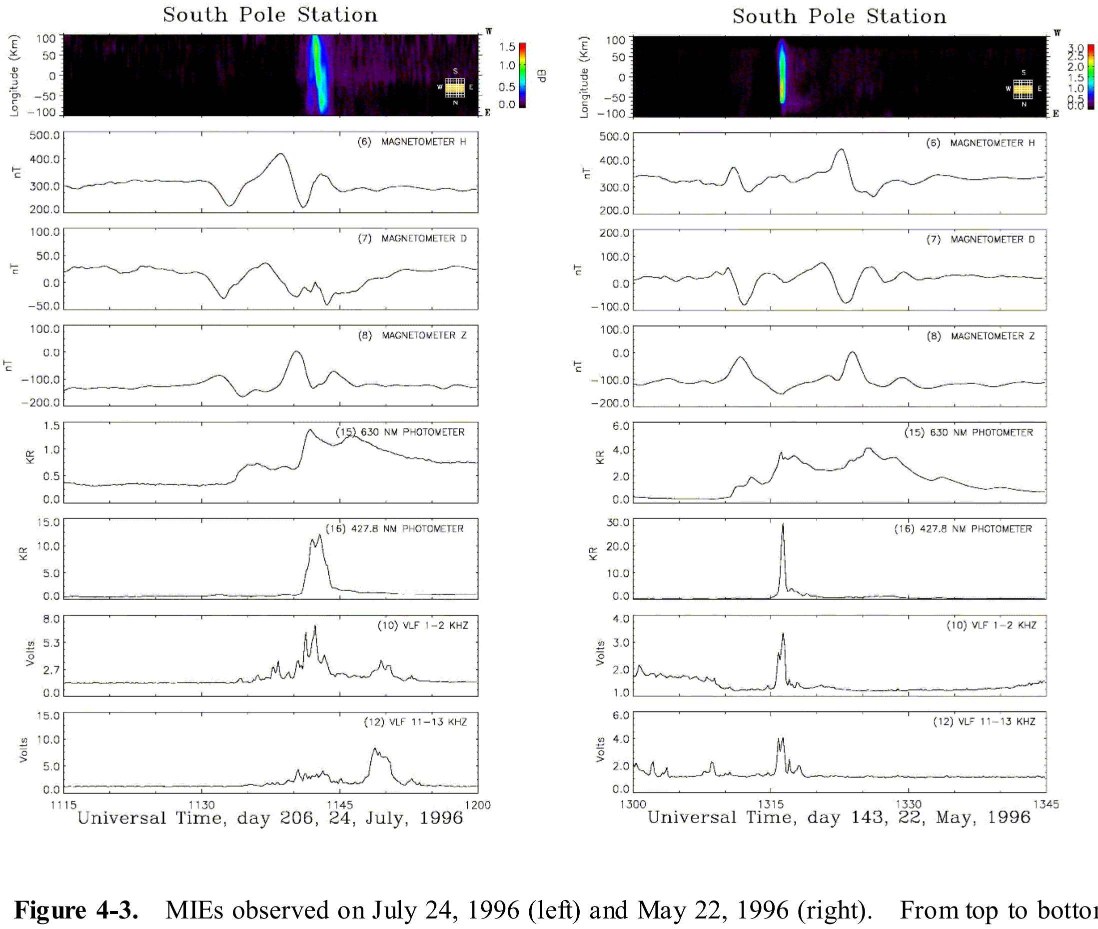

Figure 4-3. MIEs observed on July 24, 1996 (left) and May 22, 1996 (right). From top to bottom, figure contains the azimuthal riogram of the ionospheric absorption, magnetic field H, D, Z component magnitudes in nT and local geomagnetic coordinates, the intensities of 630.0 nm photometer, 427.8 nm photometer, VLF 1-2 kHz band, and VLF 11-13 kHz band. The data/plots were provided courtesy of the University of Maryland.

Auroral and CNA activities accompanied by these MIEs are shown in Figure 4-2 and Figure 4-3. The 630.0 nm auroral intensity tends to increase with a decrease in the MIE Z-component for the entire interval of MIEs. On the other hand, enhancements of the 427.8 nm auroral intensity occurred with more short durations, 3-5 min for both of the May-25a and July-24 events, but only 1-2 min for the May-22 event. The sharp enhancement of CNA generally corresponds to the enhancement of 427.8 nm aurora for the three MIEs observed in the dawn sector. VLF signatures are completely different for each event. The VLF signature for the July-24 MIE is rather different from typical impulsive auroral hiss, exhibiting wave energy mostly below 10 kHz. On the other hand, the VLF signature for the May-22 MIE covers a broader frequency range. There are not such clear VLF responses in May-25a event.

May 22, 1996 MIE

The observation of MIE related aurora using the all-sky camera network is successful on May 22, 1996. *Mende et al.* [submitted to Journal of Geophysical Research, 2000] have reported detailed optical feature on this event.

Figure 4-4 shows equivalent convection patterns at 2 min intervals. The format of the figure is the same as Figure 3-5. Beginning at ~1310 UT in the northern hemisphere, the convection arrows become large enough to indicate a tendency for clockwise rotation in the dusk side and a tendency for counterclockwise rotation in the dawn side, respectively. At 1318 UT in the northern hemisphere, the convection arrows indicate clockwise rotation in the dawn side and counterclockwise rotation in the dusk side. At this timing, the first counterclockwise vortex moved to the location of ~72° MLAT and 6.8 MLT. The scale size of the twin vortex is approximately 1000 km.

The auroral images in fish-eye coordinate in the wavelengths of 427.8 nm and 630.0 nm observed by SP are shown in Figure 4-5. The center of each image is the zenith. The magnetic poleward direction is the top of each image and right is westward. A stable auroral oval appeared near the poleward edge of the field of view before the onset of MIE at 1310 UT. From 1311 to 1314 UT when clockwise vortex passed through the SP station, 630.0 nm patchy aurora with poleward motion appeared equatorward of the auroral oval. At 1616 UT, the timing when the counterclockwise vortex passed over the SP station, an abrupt enhancement of 427.8 nm aurora occurred in a small region equatorward and westward of SP with a duration of ~1-2 min.

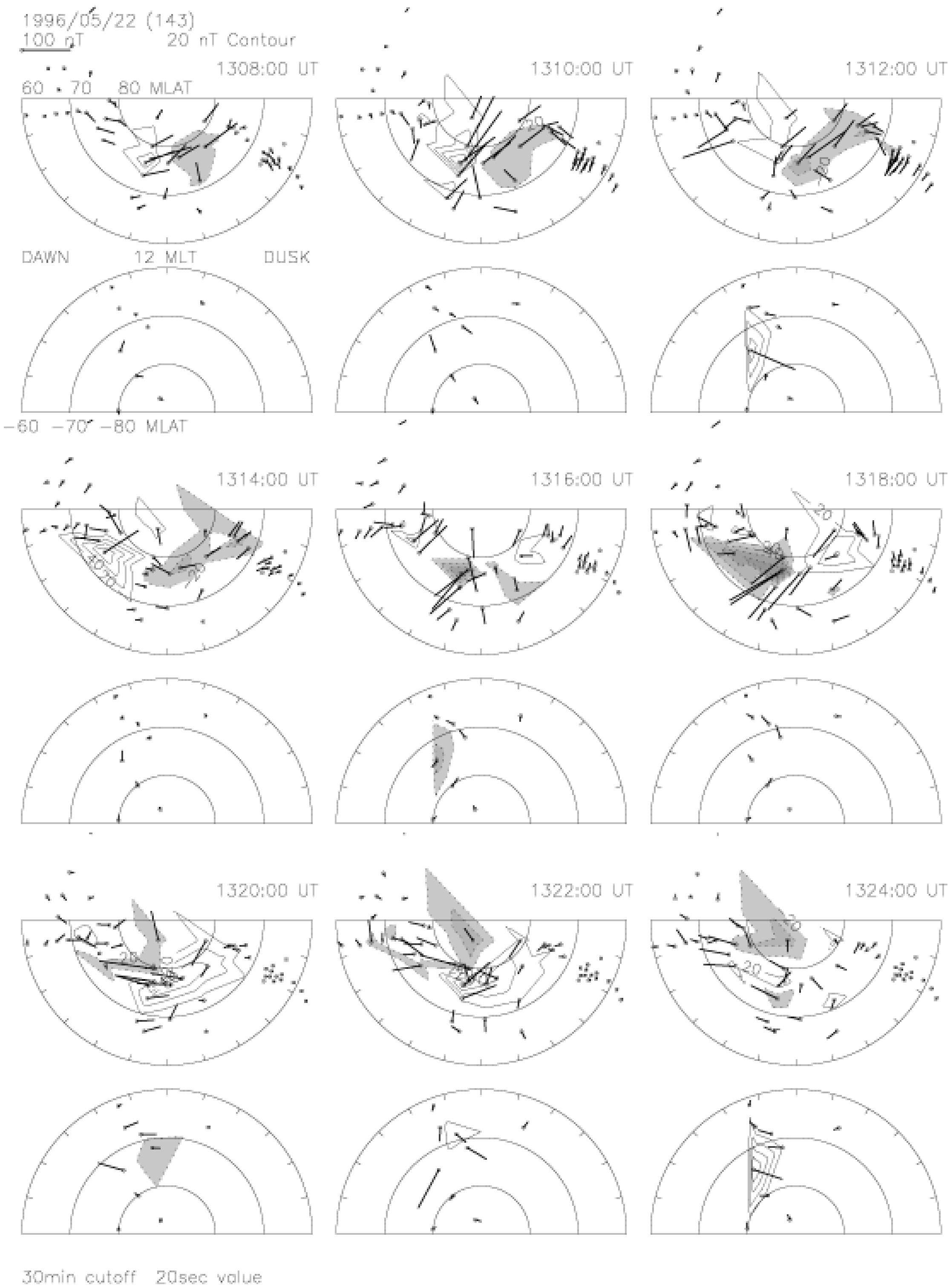

Figure 4-4. Equivalent convection direction plots at 2 min intervals from 1308 to 1324 UT May 22, 1996. The format of each figure is the same as Figure 3-5.

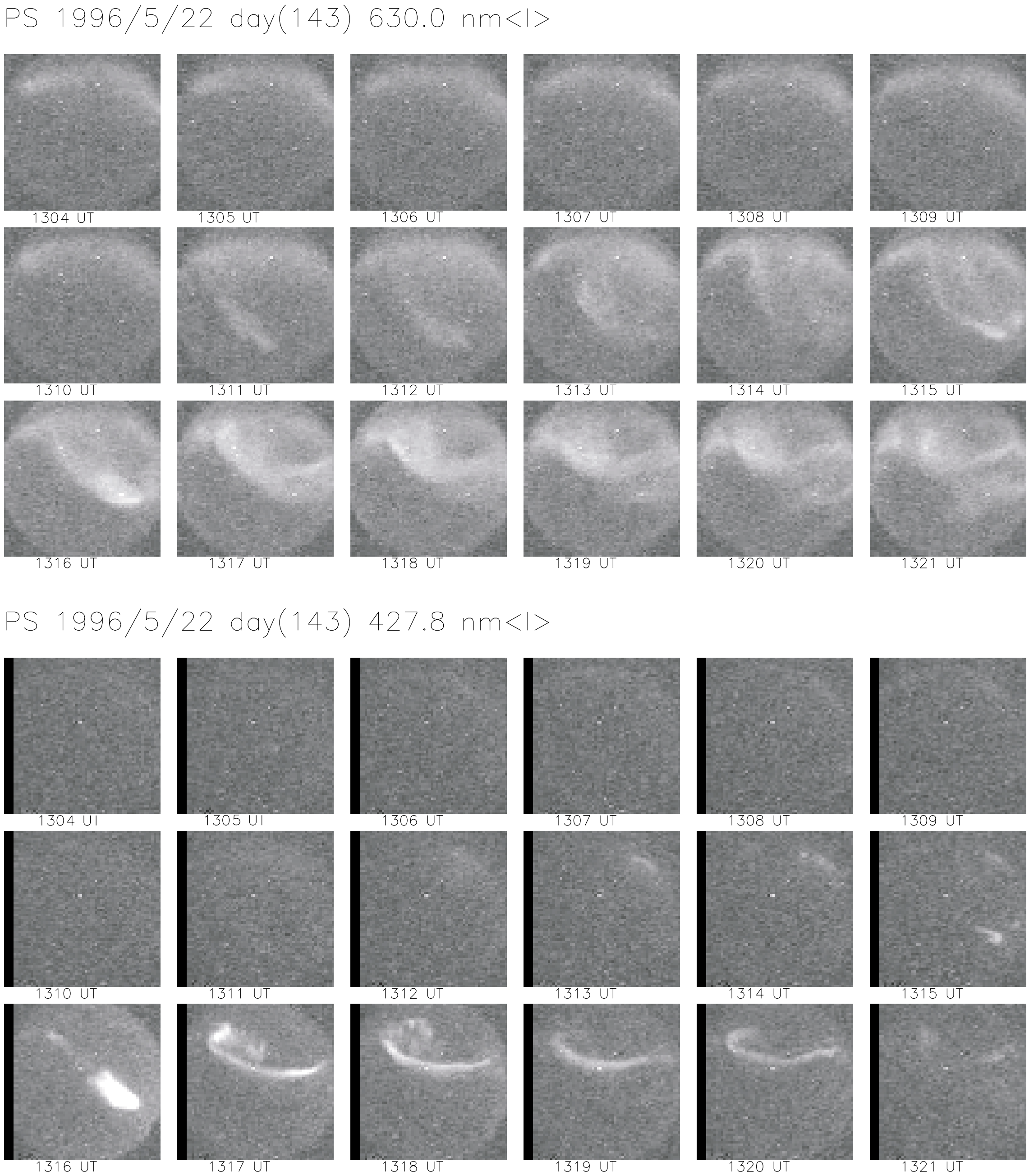

Figure 4-5. All-sky images in the wavelengths of 427.8 nm (top) and 630.0 nm (bottom) between 1304 and 1321 UT on May 22, 1996. The center of each image is the zenith, while the magnetic poleward direction is top side and right is westward in fish-eye coordinates.

The trigger of this event is relatively clear because Interball-Tail located at a good position to monitor the solar wind, GSE (x, y, z) = (23.8, -1.2, 12.3) at 1303 UT. Interball-Tail observed an abrupt northward turning from –2 to 2 nT with a slow density increase at 1303 UT that is slightly before the MIE interval (cf., Figure 4-6). The identical discontinuity was observed by Wind (1256 UT) and Geotail (1244 UT) at the location of GSE (x, y, z) = (124.1, -24.2, -6.5) and (26.3, 10.6, -3.4) respectively. Assuming that the solar wind velocity is (430, 0, 0) km/sec in GSE coordinates from Wind observation, the normal vector of the discontinuity plane is calculated as GSE (x, y, z) = (0.21, 0.93, -0.31) by applying the 3-SAT method using three satellite observation data described in Section 2.4. The minimum variance analysis (MVA) of the Wind 3-sec magnetic field data from 12:55:01 to 12:55:58 UT reveals that the normal to this discontinuity pointed in the GSE (x, y, z) = (0.40, 0.87, -0.28). The ratio of the eigenvalues for the intermediate to minimum variance directions, 8.5, indicates that the normal is well determined. Since the absolute value of the IMF normal component is small ~ 0.25 nT, this discontinuity is probably a tangential discontinuity (TD). We can also calculate the normal vector **n** by assuming that the discontinuity is the TD, that is

$$\mathbf{n} = \frac{\mathbf{B}_1 \times \mathbf{B}_2}{|\mathbf{B}_1 \times \mathbf{B}_2|}, \tag{4-1}$$

where $\mathbf{B}_1$ and $\mathbf{B}_2$ are the upstream and downstream magnetic field vectors, respectively. The normal vector using this method results in GSE (x, y, z) = (0.45, 0.84, -0.30). This result gives further evidence that the discontinuity is identified as TD.

Using the normal of the 3-SAT method, it is predicted that the discontinuity hits the bow shock nose point GSE (x, y, z) = (14, 0, 0) at 1257 UT, 6 min before the Interball-Tail observed the discontinuity. The ground onset is ~1310 UT and it is concluded that it takes 13 min from the TD hitting of the bow shock nose to the generation of the MIE.

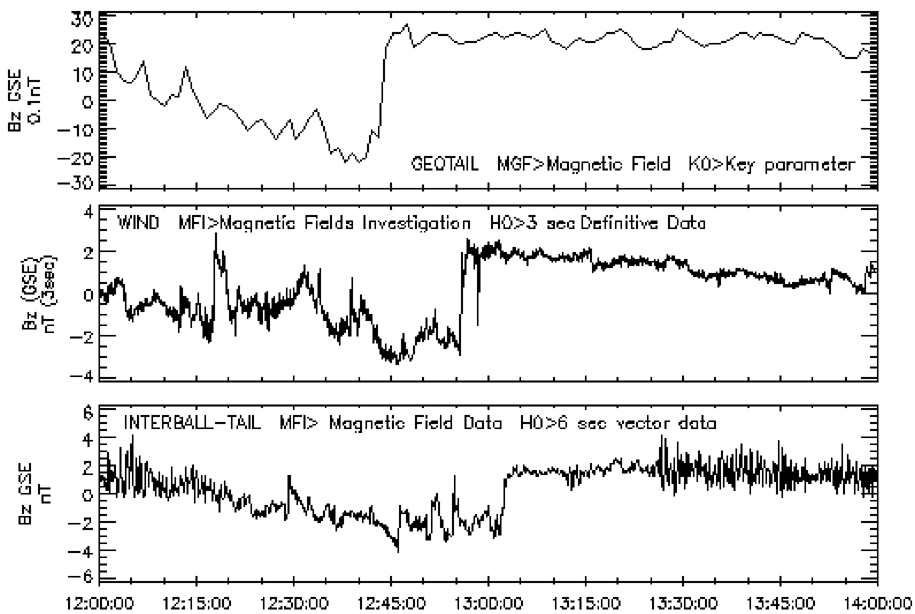

Figure 4-6. IMF B_Z variations observed at three satellites in the time interval 1200-1400 UT on May 22, 1996. From top to bottom, Geotail, Wind, and Interball-Tail are shown.

July 24, 1996 MIE

On July 24, 1996, a gross deformation of the dayside magnetopause was observed by Interball-Tail [*Sibeck et al.*, 1998]. *Sibeck et al.* [1999] concluded that the gross deformation is the magnetospheric response to an IMF tangential discontinuity (TD) interacted with the bow shock, which formed a hot flow anomaly (HFA). Pressure within and earthward of the HFA was depressed by an order of magnitude, which allowed the magnetopause to briefly (~7 min) move outward some 5 Re beyond its nominal position (see Figure 4-7). The July 24 event is analyzed in this study as the MIE that has its clear origin of the HFA.

The normal vector of the TD was calculated by applying MVA to the Wind observation from 1018:55.5 UT to 1019:37.5 UT pointed in the GSE (x, y, z) = (-0.40, -0.73, 0.56) direction [*Sibeck et al.*, 1999]. The predicted lag from Wind to Interball-Tail is 70 min [*Sibeck et al.*, 1999], which is almost consistent with the MIE timing.

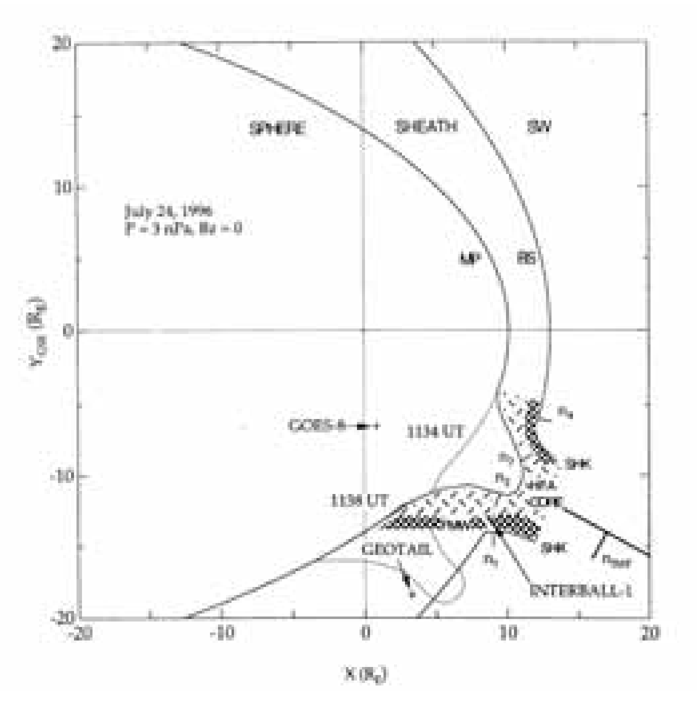

Figure 4-7. The trajectory of Interball-Tail from 1130 to 1200 UT and the positions of Geotail and GOES-8 at 1135 UT on July 24, 1996. The interaction of a northward, dawnward, and antisunward moving interplanetary magnetic field (IMF) discontinuity with the bow shock produces a hot flow anomaly (HFA) bounded by shocks (SHK) in the solar wind and fast mode waves (FMW) in the magnetosheath [form *Sibeck et al.*, 1999].

All-sky images taken at SP and sampled at one or two min intervals with an exposure time of 16 sec are depicted in Figure 4-8. 427.8 nm aurora is seen to suddenly fill the field of view at 1142 UT. There is no structure in 427.8 nm aurora except for a small blob that appears in the middle of the image. In the next image, taken at 1143 UT, the discrete feature develops equatorward and westward of SP with a latitudinal width of about 100 km and considerably larger longitudinal width of about 500 km [*Weatherwax et al.*, 1999]. On the contrary, the 630.0 nm auroral response is nearly dim. The ionospheric response might be too fast to make a clear 630.0 nm auroral structure, since the lifetime of the 630.0 nm auroral emission is 110 seconds.

Equivalent convection pattern plots are shown in Figure 4-9. Beginning at 1142 UT in the northern hemisphere when 427.8 nm aurora was seen to suddenly fill the field of view in the southern hemisphere, the convection arrows become large enough to indicate a clockwise rotation around 8 MLT and 78° MLAT. The clockwise vortex, which corresponds to the upward field aligned current from the ionosphere in the northern hemisphere, extended to ~6 MLT by 1146 UT. Although it is difficult to find clear convection vortex structure in the southern hemisphere for the event, IQA and SP shows similar rotation of the convection arrows. This implies that similar upward field aligned current existed somewhat poleward of SP at the MIE timing.

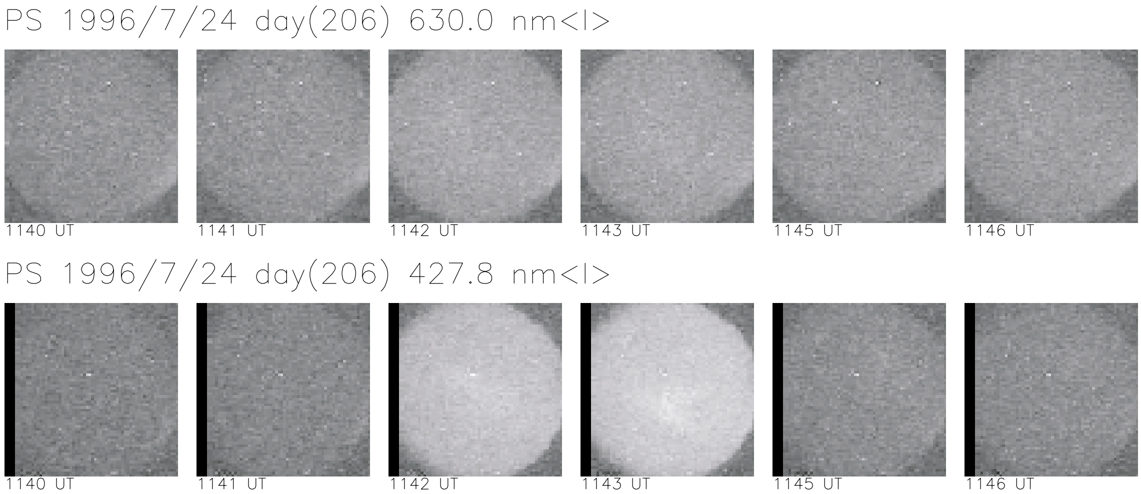

Figure 4-8. All-sky images at SP between 1140-1146 UT on July 24, 1996. The format of each image is the same as Figure 4-5

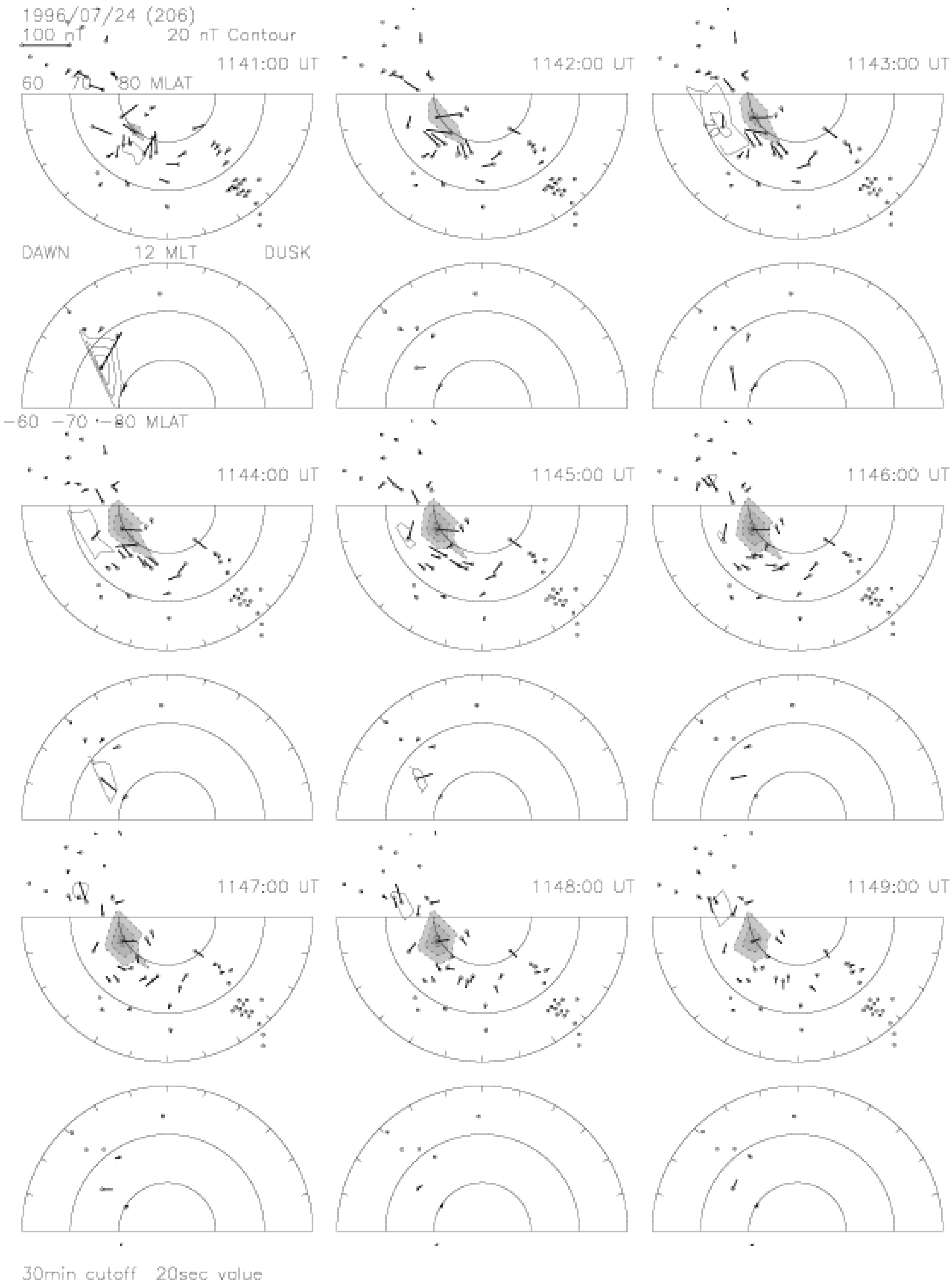

Figure 4-9. Equivalent convection direction plots at 2 min intervals from 1141 to 1149 UT July 24, 1996. The format of each figure is the same as Figure 3-5.

May 25a, 1999 MIE

Optical signature was investigated in detail for the MIE occurred in the dawn sector on May 25, 1999. The MIE-related aurora is clearly seen in 427.8 nm at SP (cf., Figure 4-10). The strongest enhancement of 427.8 nm aurora with one minute duration at 1224 UT is corresponds to the short period strong enhancement of CNA (cf. Figure 4-2) and the MIE with a largest amplitude. The enhanced east-west aligned auroral arc deformed after 1224 UT by bending the westside of arc by 90° poleward.

On the other hand, quiet auroral activity is seen at MM station (around 5.5 MLT and 80 MLAT), implying that MM is well within the polar cap. So-called a sun-aligned arc [e.g., *Shiokawa et al.*, 1995, 1996, 1997] was observed in the MIE timing (Figure 4-11). The sun-aligned arc appeared clearly at 1223 UT. Then the arc structure moved poleward and disappeared at ~1230 UT. Since the 427.8 nm aurora is very faint relative to 630.0 nm aurora, it is suggested that soft electron precipitation is dominant for this sun-aligned arc.

In order to make clear where the aurora located at that time, images mapped onto geomagnetic coordinates at 1224 UT are shown in Figure 4-12. A trident arc extending 74°, 75°, and 76° MLAT is evident in the 427.8 nm image in the right panel. An east-west aligned arc at 74°-75° MLAT over SP and a sun-aligned arc at 76°-78° MLAT over MM are seen in the 630.0 nm image.

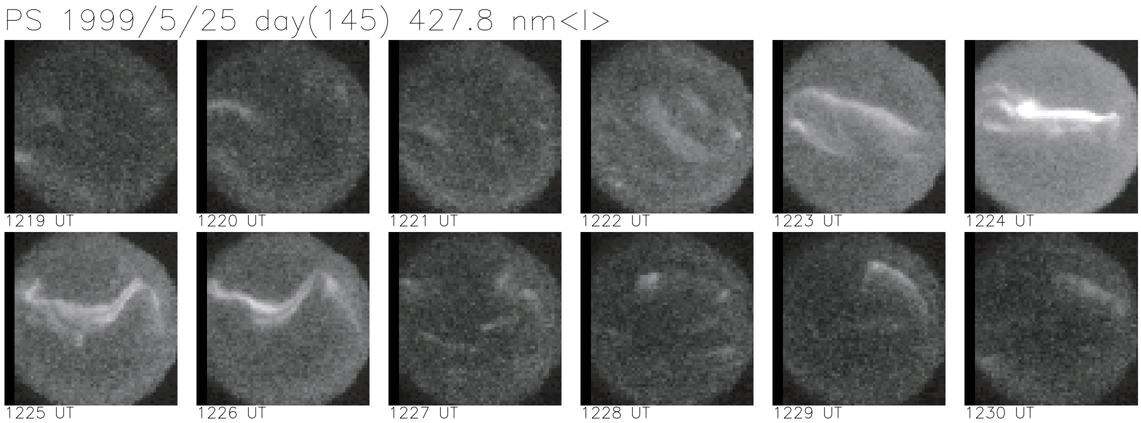

Figure 4-10. All-sky images obtained at SP between 1219 and 1230 UT on May 25, 1999. The format of each image is the same as Figure 4-5.

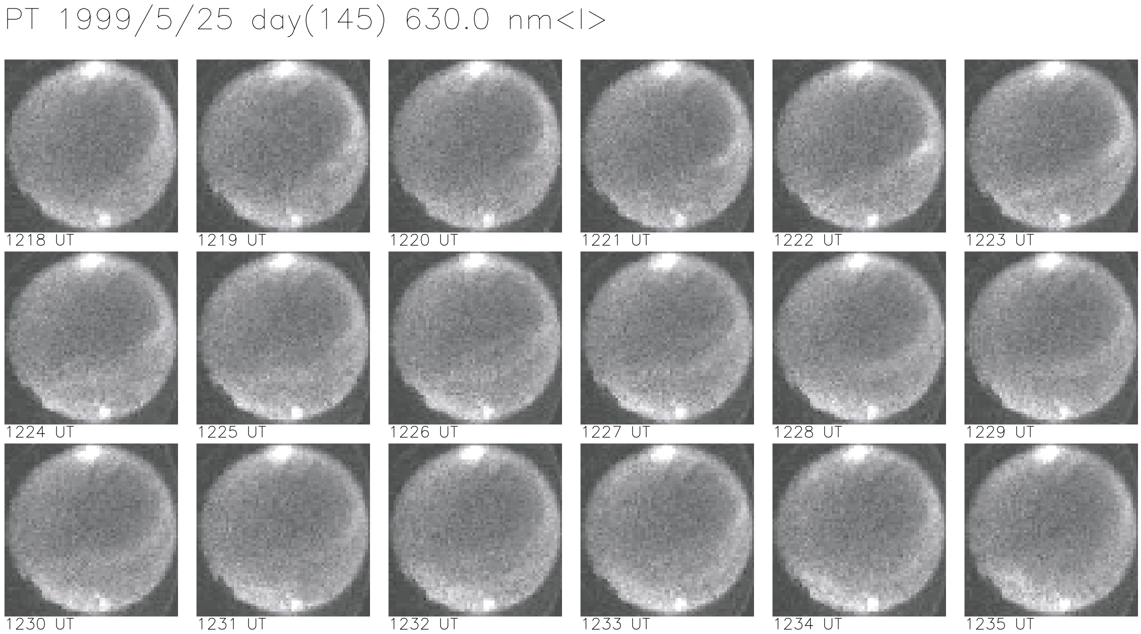

Figure 4-11. All-sky images obtained at MM between 1218 and 1235 UT on May 25, 1999. The format of each image is the same as Figure 4-5.

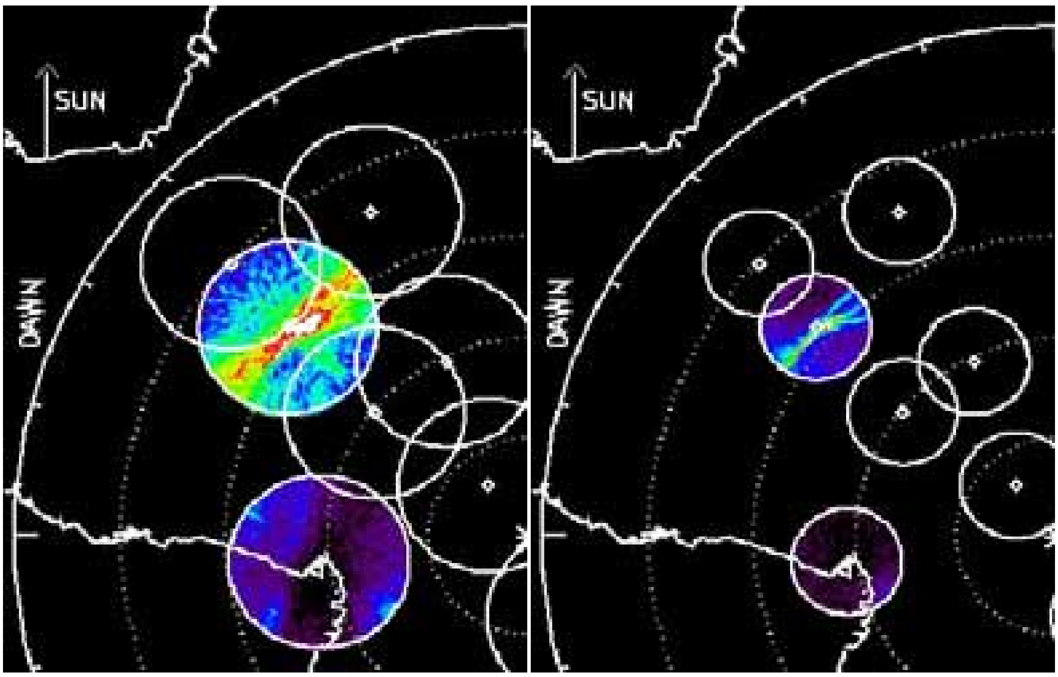

Figure 4-12. Geographic projections of the all-sky images, looking down the southern hemisphere, taken at SP and MM in the wavelengths of 630.0 nm (left) and 427.8 nm (right) at 1224 UT on May 25, 1999. The assumed altitudes of emission layers are 200 km and 110 km for 630.0 nm and 427.8 nm emissions, respectively.

Figure 4-13 shows the equivalent convection pattern plot derived from the horizontal magnetic component data of the Greenland west coast chain and the southern hemisphere magnetometer network. The pattern is obtained by first filtering the magnetic data with a 30-min high pass filter and then rotating the resulting horizontal perturbation vector 90° counterclockwise. Nearly identical counterclockwise vortices accompanied by clockwise vortices were appeared twice centered at 1223 UT and 1239 UT. Greenland SKT is the approximately conjugate station of P3. Their magnetic perturbation seems to be very similar but in opposite directions. It is expected that similar vortex pattern in opposite rotation passed in the southern hemisphere at that time. The vertical components of SP and P3 station shows that the propagation time delay of MIE is 1-2 min. Considering that P3 is located at ~1.6 MLT (23° MLON) earlier than SP, the 1-2 min difference corresponds to the propagation time of 6-12 km/sec. The burst of hard electron precipitation at 1224 UT corresponds to the timing of a passage of a counterclockwise vortex, that is, it corresponds to the upward field aligned current.

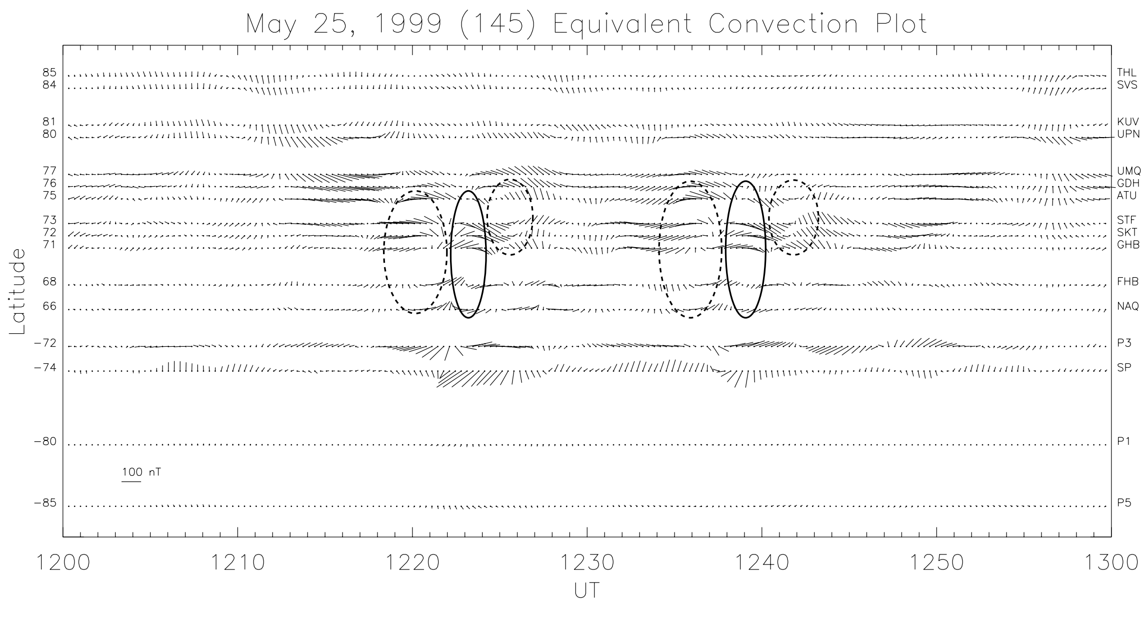

Figure 4-13. Equivalent convection pattern derived from horizontal magnetic vectors by rotating 90° counterclockwise. Each arrow is plotted every 20 sec during the interval from 1200 to 1300 UT. Upper 12 traces are Greenland west coast magnetometer chain data and bottom four traces are southern hemisphere magnetometer data. Solid circles indicate the counter clockwise vortex and dotted circles indicate the clockwise vortex.

The trigger of this event is clear when we looked at the ACE observation data (cf., Appendix). A reverse shock is identified at 0948 UT by the sharp drop of number density, temperature, and magnetic field obtained at the ACE satellite. After the reverse shock, there are almost no changes in the solar wind parameters until an abrupt change in B_X from 4 to –2 nT was observed at 1122 UT. Considering the location of the ACE satellite, GSE (x, y, z) = (224.1, 12.0, -22.5), and the solar wind velocity (-580, 15, -40) km/sec, the earthward turning seems to have occurred in a good timing to trigger the MIE. Wind and Geotail also observed a nearly identical discontinuity before the onset of the MIE (cf. Figure 4-14).

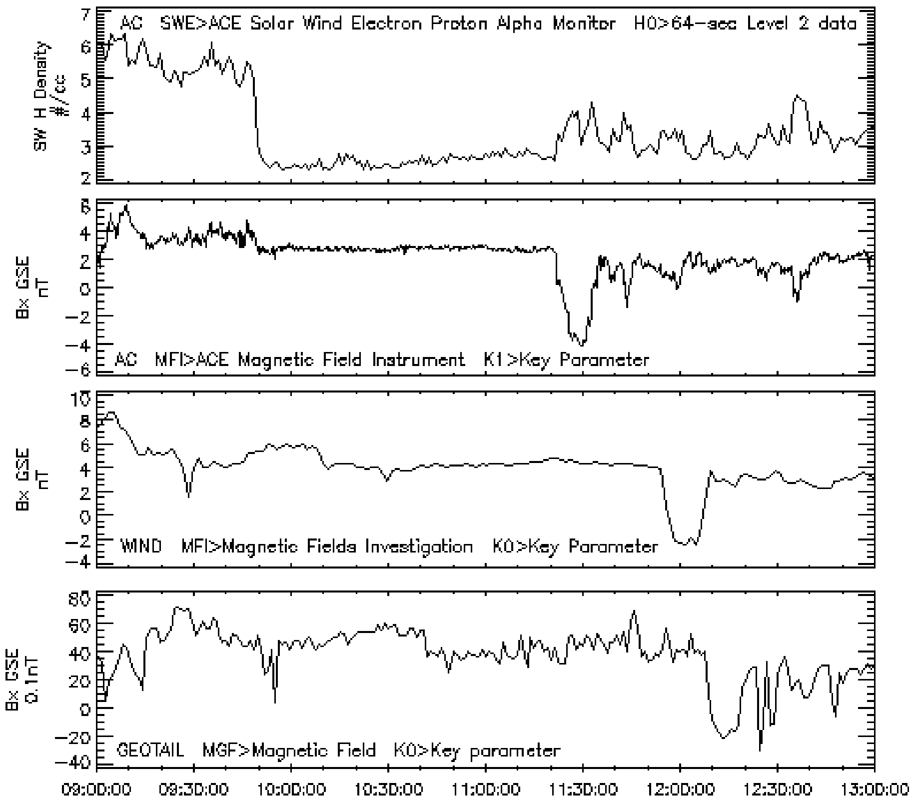

Figure 4-14. Solar wind observations of ACE, Wind, and Geotail satellites in the time interval 0900-1300 UT on May 25, 1999. Top two panels are the ion number density and IMF B_X observed by ACE. The bottom two panels are IMF B_X observed by Wind and Geotail satellites.

Wind satellite observed the strong earthward turning of IMF B_X at 1154 UT at the location of GSE = (151.1, -23.6, -11.8). Geotail also observed the discontinuity at 1210 UT at the position of GSE (x, y, z) = (17.4, 5.2, -2.8). Using the solar wind velocity of (-580, 15, -40) km/sec in GSE coordinates from ACE, the normal vector is calculated by the 3-SAT method as pointed to the direction of GSE (x, y, z) = (0.41, 0.87, -0.27). The MVA of the ACE 16-sec magnetic field data from 1118:05 UT to 1126:05 UT reveals that the normal to this discontinuity pointed in the GSE (x, y, z) = (0.42, 0.90, 0.02). The ratio of the eigenvalues for the intermediate to minimum variance directions, 18.0, indicates that the normal is well determined. Since the absolute value of IMF normal component is very small ~0.15 nT, this discontinuity is probably TD. The normal vector using the equation (4-1) results in GSE (x, y, z) = (0.40, 0.91, 0.08). This result gives further evidence that the discontinuity is TD.

Using the normal vector of the 3-SAT method, it is predicted that the discontinuity hits the bow shock nose point GSE (x, y, z) = (14, 0, 0) at 1213 UT, 3 min later the Geotail observed this TD. The ground MIE onset is found to be 1215 UT, two min before this timing when the TD hit the bow shock nose.

4.3 MIEs in the noon sector

The relationship between the vertical magnetic field component, auroral intensities of 427.8 nm and 630.0 nm, and CNA observed at SP are summarized in Figure 4-1 and Figure 4-2 for the MIEs on May 27, 1998 (May-27 MIE) and July 3, 1999 (July-3 MIE), respectively. The ratio of the intensity of 427.8 nm to the 630.0 nm is relatively low (0.05-0.2) for these two MIEs. The CNA of the MIEs are also very weak, slightly above the noise level (~0.05 dB). This implies that these MIEs are accompanied by soft electron precipitation.

May 27, 1998 MIE

In Figure 4-15, a slow increase of the 427.8 nm auroral intensity occurred in the equatorward and westward edge of the field-of-view from 1606 to 1608 UT. This variation of auroral intensity is also confirmed in Figure 4-1. Since there were no 630.0 nm auroral enhancements at that timing, this implies that hard electron precipitation occurred at first three min before the main auroral enhancement interval from 1608 UT. The MIE-related auroral activity was mostly apparent in the 630.0 nm images for the time period of the MIE at SP. The region of probably cusp/cleft aurora was seen near the poleward edge of the field-of-view. The MIE related aurora appeared in the westward edge and lower latitudes than the cusp/cleft aurora. At 1610 UT, this aurora began to extend and/or moved eastward (toward dusk) across the magnetic local noon within 72°-76° MLAT.

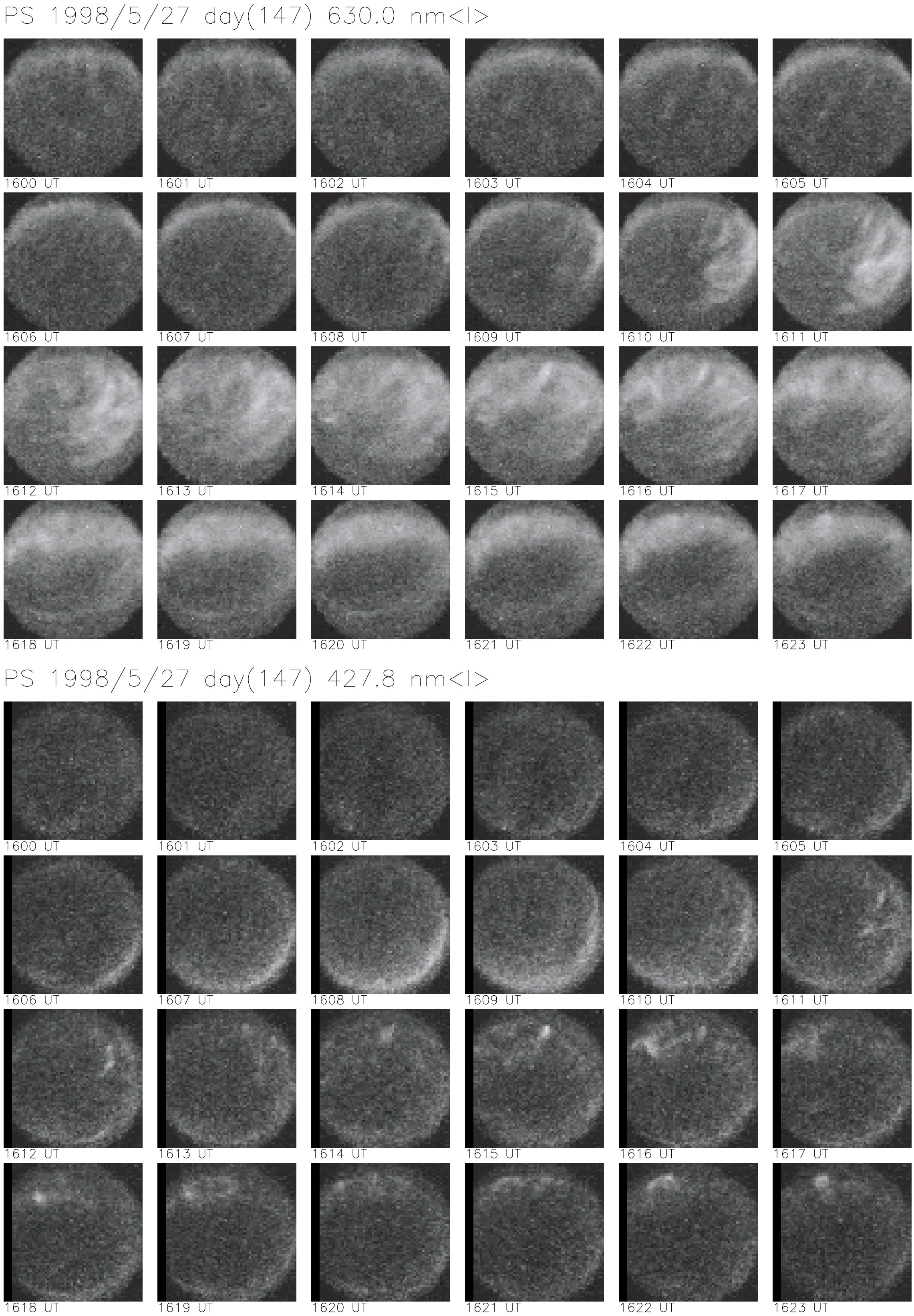

Figure 4-15. All-sky images at SP between 1600 and 1623 UT on May 27, 1998.

Equivalent convection pattern in the northern and the southern hemisphere on May 27, 1998 is shown in Figure 4-16. Beginning at 1552 UT in the northern hemisphere, the convection arrows become large enough to indicate a tendency for counterclockwise rotation centered at ~77° MLAT and ~11.5 MLT. This vortex moved eastward and equatorward by 1604 UT centered at 75° MLAT and 14 MLT and disappeared. The next clockwise vortex appeared in lower latitude region centered at ~73° MLAT and ~11.3 MLT at 1606 UT. This clockwise vortex moved eastward and slightly poleward across the noon meridian and ended at ~1616 UT around 76° MLAT and 13.5 MLT. The separation between the first counterclockwise vortex and the second clockwise vortex is ~1000 km.

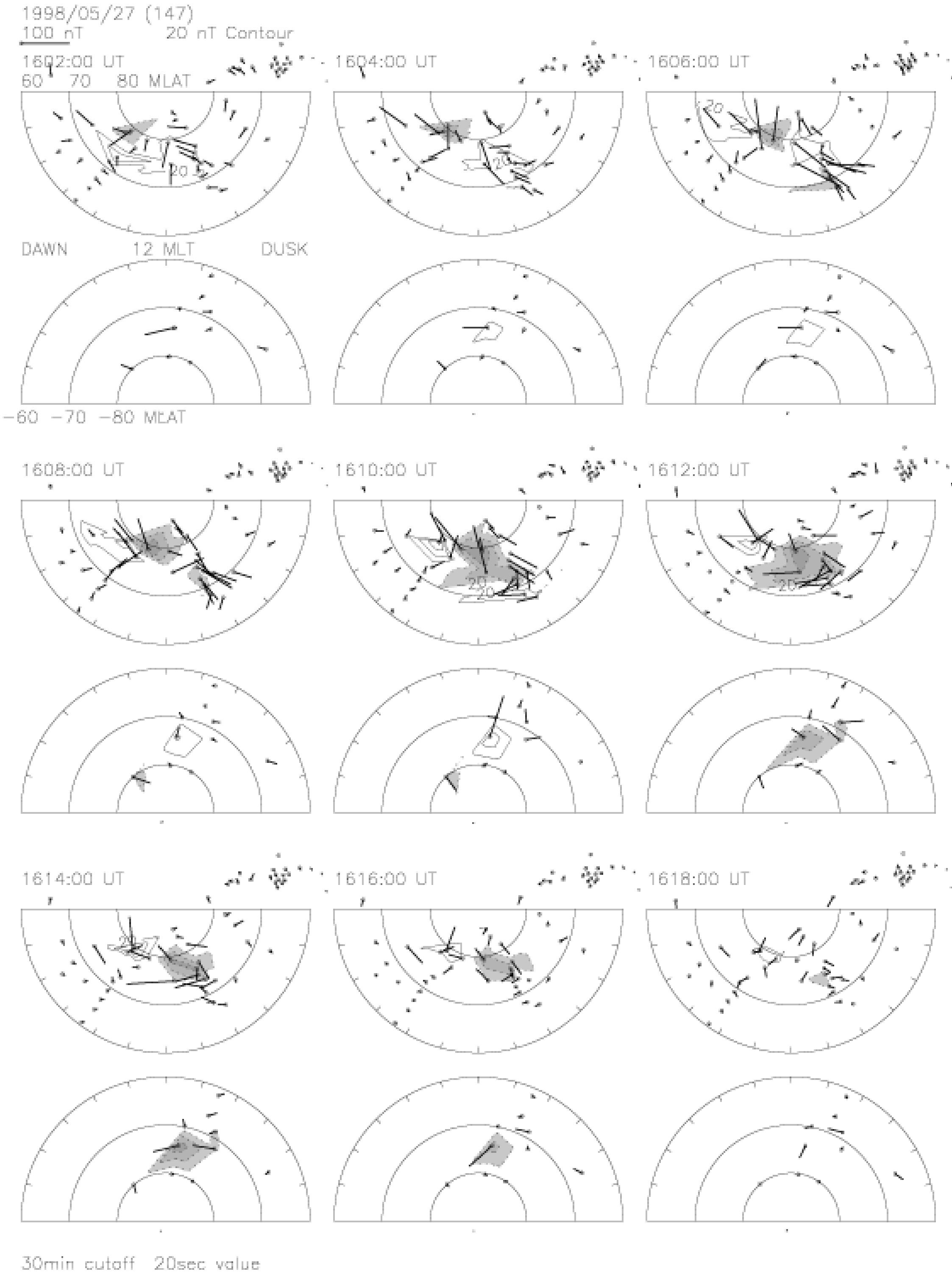

Figure 4-16. Equivalent convection patterns on May 27, 1998. The format of each figure is the same as Figure 3-5.

The interplanetary conditions during the May-27 MIE are investigated using Wind, IMP-8, and Geotail data. It is found that IMF B_Y turning occurred at 1508, 1523, and 1608 UT, respectively, which might be the trigger of the MIE. The normal vector of the discontinuity is calculated to estimate the propagation time from three satellites to the Earth. The locations of these each satellites are GSE (x, y, z) = (192.4, 36.7, 25.6) for Wind, (3.5, 29.9, -25.4) for IMP-8, and (21.6, 10.7, -3.0) for Geotail as shown in Figure 4-17. Using the solar wind velocity of (-360, -5, -10) km/sec in GSE coordinates from Wind, the normal vector is calculated by the 3-SAT method as pointed to the direction of GSE (x, y, z) = (0.17, 0.80, -0.57). The MVA was tried but the normal vector could not be determined. Using the normal vector of the 3-SAT method, the time when the discontinuity hits the bow shock nose point at GSE (x, y, z) = (14, 0, 0) is predicted to be 1629 UT. This time is late than the MIE onset at ~1605 UT. The B_Y turning actually interacted with the bow shock more earlier at the point, for example, GSE (x, y, z) = (10, 15, 0) at 1608 UT. However, the trigger should be observed still 10-20 min earlier than this discontinuity. This is confirmed from a comparison between the number density (fifth panel) measured by Geotail and 'Hp' (sixth panel) measured by GOES-8 in Figure 4-18. Some correlation is found between these two panels. Number density variations were approximately 10 min preceding magnetic field variations for this four-hour interval.

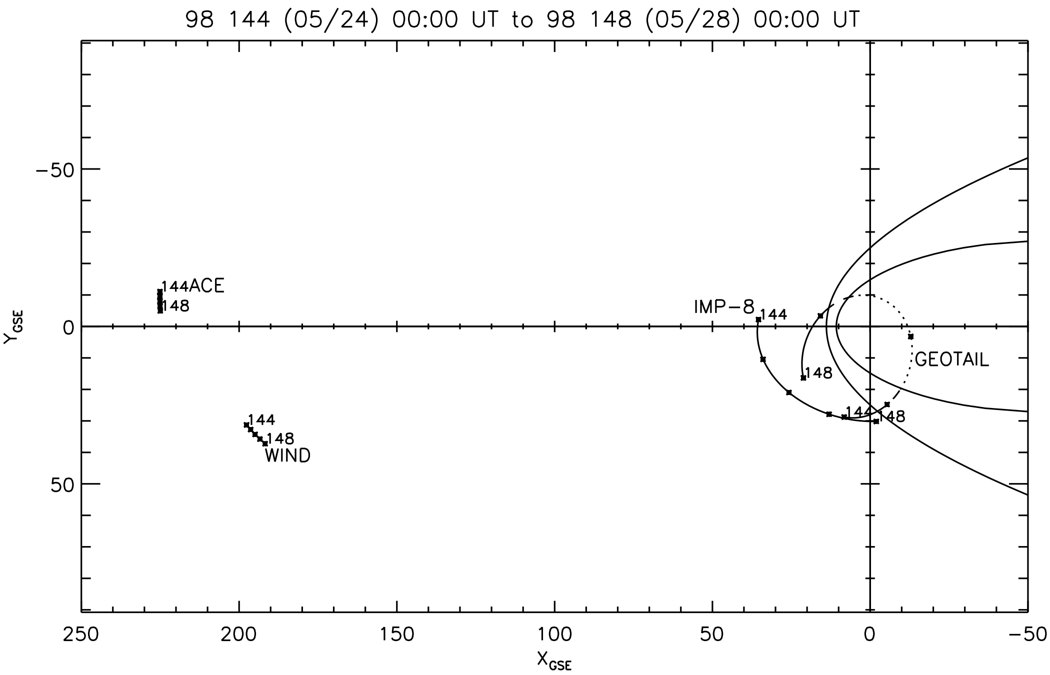

Figure 4-17. Locations of the space crafts from May 24 to May 28, 1998.

It is concluded that the trigger was embedded in the very disturbed solar wind region between 1548 and 1558 UT. There were many pressure pulses which could be the trigger of this event. The Wind spacecraft also observed many pressure pulses. However, if these pressure pulses are the trigger of the MIE, it remains mysterious how these pressure pulses could make single impulsive magnetic field response.

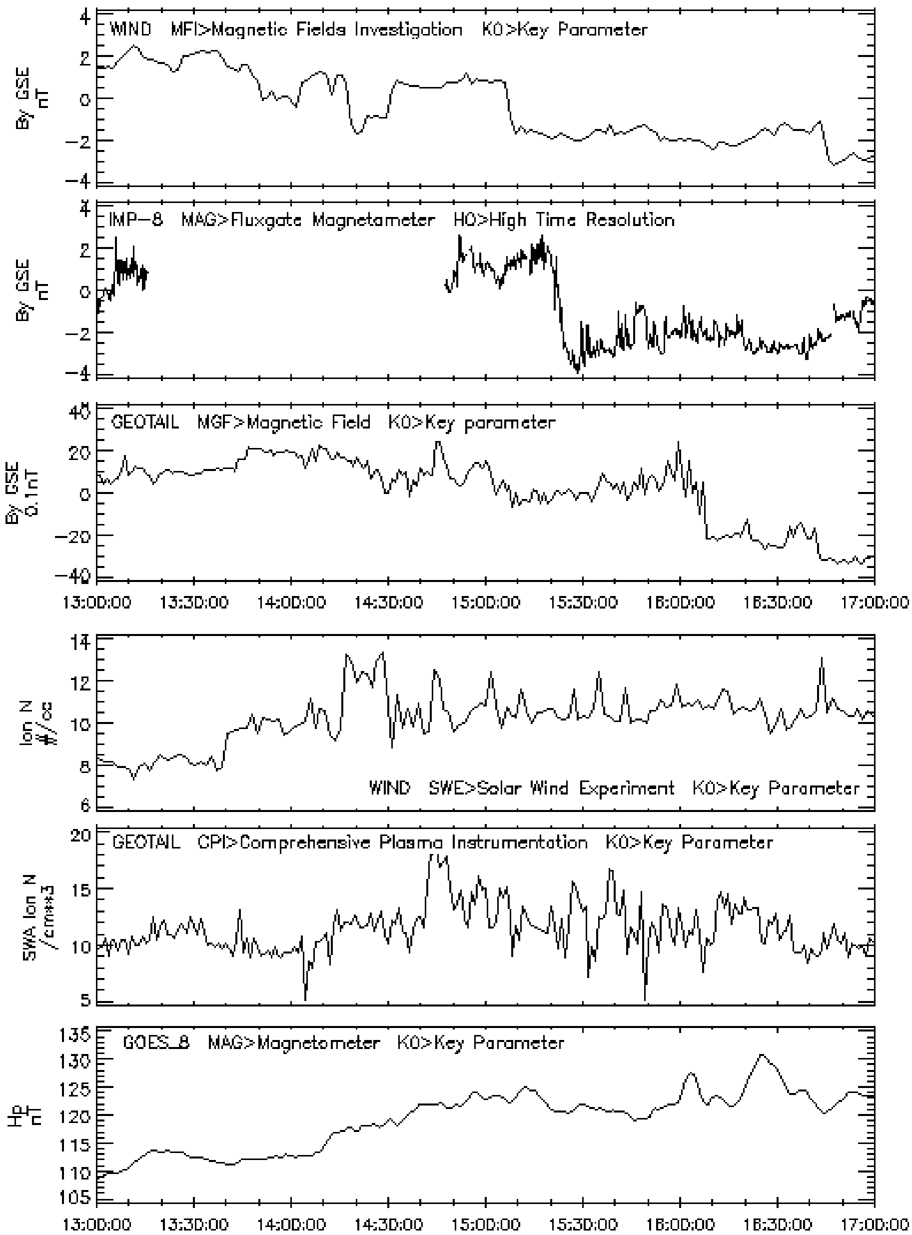

Figure 4-18. Solar wind and geosynchronous data between 1300 and 1700 UT on May 27, 1998. The top three panels show B_Y turning observed by Wind, IMP-8, and Geotail. The bottom three figures show number density observed at Wind and Geotail, and the magnetic field perpendicular to the orbital plane of GOES-8.

July 3, 1999 MIE

We suggests that the trigger of this MIE may be a clear northward turning observed by ACE at 1555 UT (cf., Appendix). There are no significant disturbances in the previous two hours. The discontinuity line in the X-Y plane could be determined assuming that the discontinuity is constant in the Z direction. The ACE and Wind spacecraft located very closely on the X-Y plane at GSE (x, y, z) ~ (237, 38, 0) and (208, -22, 0) respectively. Using the solar wind velocity of (510, 0, 0) km/sec in GSE coordinates and the timing of 1445 UT when the Wind observed the northward turning, normal vector is GSE (x, y) = (0.18, -0.98), that is strongly dawnward. The northward turning plane reached to the bow shock nose at 1553 UT. The northward turning could be the trigger of the ground onset timing at ~1540 UT because there is significant ambiguity in the determination of the real triggering on this event. The cone angle is very small ~20° for previous hours. Since the discontinuity oriented nearly along the sun-earth line, the discontinuity strikes near the bow shock nose and magnetopause nose for a long time up to ~1 hour. Equation (4-1) for the Wind observation of this discontinuity gives the direction of GSE (x, y, z) = (0.03, -0.97, -0.24). Since the absolute value of the normal component of IMF is very small (less than 0.1 nT), this discontinuity is probably TD. The all-sky images of the July-3 MIE taken at SP are shown in Figure 4-19. The moon was at the westward and poleward edge of the field-of-view. MIE-related 630.0 nm aurora appeared at the edge of the field-of-view at SP during 1544-1545 UT. Patchy-shaped aurora moved from dawn to dusk in lower latitudes than the auroral oval. During this interval, the clockwise vortex corresponding to the upward field-aligned current, moved eastward across the noon meridian in the northern hemisphere. The bulk auroral motion as well as the motion of the vortex, which is originated the dawn side and moved eastward in the both hemispheres across the noon meridian, is similar to the May-27 event and the June-6 event described in Chapter 3.

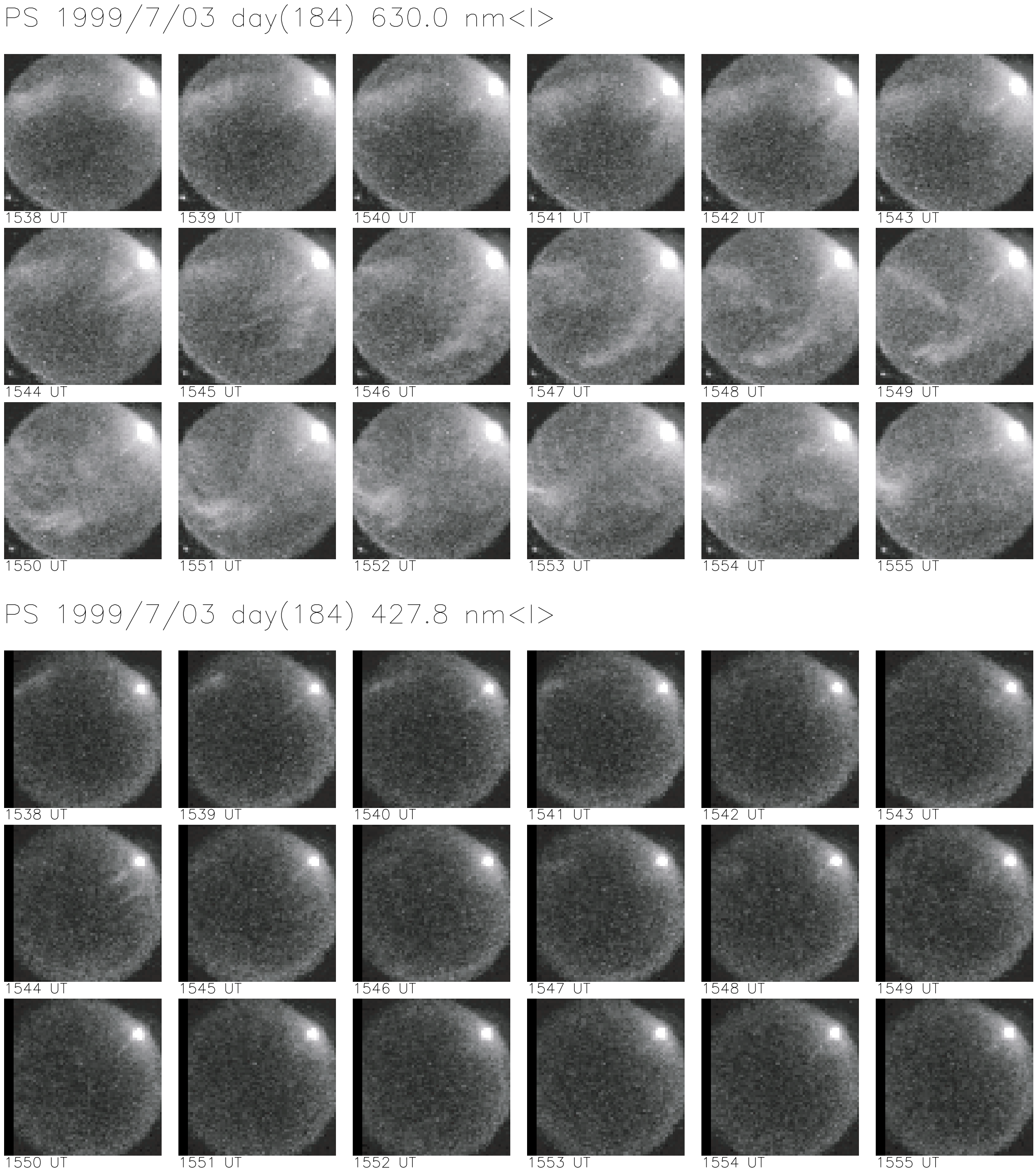

Figure 4-19. All-sky images between 1538 and 1555 UT on July 3, 1999. The format of each image is the same as Figure 3-5.

The NIPR image was investigated in order to see more detailed structure of aurora. Figure 4-20 shows the 630.0 nm auroral images obtained by the all-sky imager of National Institute of Polar Research (NIPR-ASI) at SP. All images are mapped onto CGM coordinates as looking down the ionosphere. Top is sunward and a solid line shows the CGM pole direction. In the coordinate transformation, the height of the emission layer is set to 200 km for the 630.0 nm emission. The NIPR imager revealed that the patchy-shaped aurora has so-called corona structure.

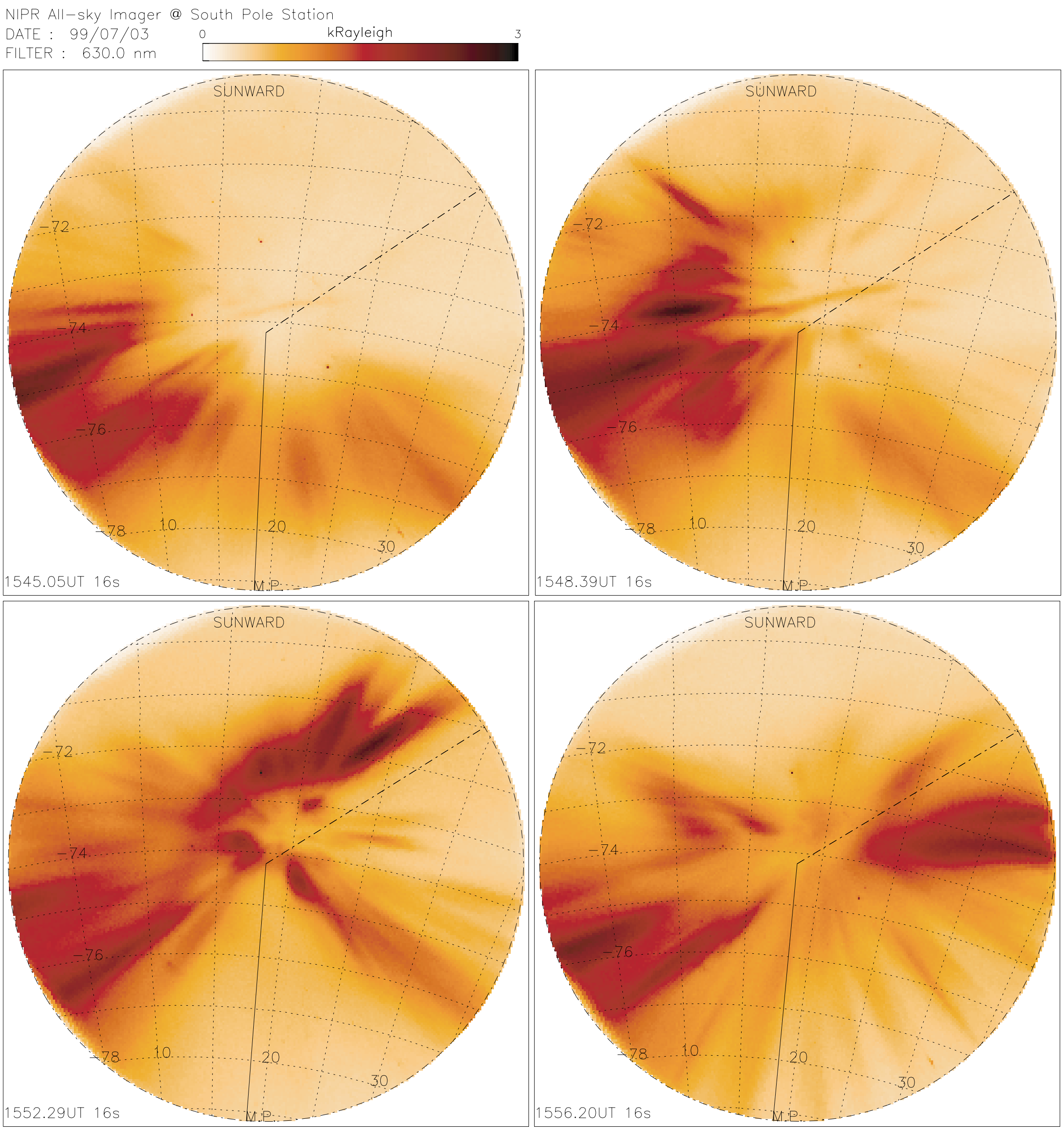

Figure 4-20. 630.0 nm images taken by the NIPR-ASI at SP between 1545:05 and 1556:20 UT on July 3, 1999. Top is sunward and a solid line shows CGM pole direction. Each image is transformed on CGM coordinates by assuming that the height of the emission layer is 200 km.

4.4 MIEs in the dusk sector

Three MIEs observed in the dusk sector were investigated. These MIEs were accompanied by auroral activities with 427.8 nm to 630.0 nm intensity ratios of 0.3-0.5 (cf. Figure 4-1 and Figure 4-2). Enhancements of CNA activity were very low (~0.05 dB) for two MIEs on May 16 (May-16 MIE) and May 25, 1999 (May-25b MIE), but it is relatively high (~0.13 dB) for the MIE on July 30, 1998 (July-30 MIE). Convection patterns, auroral activities, and characteristics of the solar wind are shown for three MIEs.

July 30, 1998 MIE

The Wind and Geotail spacecraft observed evidence of pressure pulses in the solar wind which might cause the MIE on July 30, 1998. In Figure 4-21, the top five panels show the solar wind IMF B_X, B_Y, and B_Z in GSE coordinates, proton number density, and dynamic pressure observed by Geotail in the time interval of 1600-2000 UT on July 30, 1998. The bottom panel in Figure 4-21 shows geomagnetic field observation observed by GOES-8 at geosynchronous orbit in the same time interval. Twin pressure pulses were observed at 1835 and 1850 UT. The first pressure pulse consists almost only density change, while the second pressure pulse is accompanied by a large rotation of the magnetic field from duskward to dawnward. Using the relation (4-1), the direction of the normal vector of the second discontinuity plane observed at Geotail is determined to be GSE (x, y, z) = (0.40, -0.08, -0.91). Since the IMF normal component to this normal vector is small ~0.2 nT, this discontinuity is appeared to be tangential discontinuity. The MVA method also presented the same result. There is a clear correlation between occurrences of pressure pulses and GOES Hp field variations. The calculated time lag is 3 min from Geotail to the bow shock nose point GSE (x, y, z) = (14, 0, 0) using the normal vector. The approximate time lag from the double pressure pulse to the double peak of the GOES-8 Hp at 1842 and 1857 UT is 7 min.

These compression effects appeared in the ionosphere as the counterclockwise vortex in the dusk hemisphere. Equivalent convection plots are shown in Figure 4-22. Note that the first pressure pulse causes the counterclockwise vortex at 1842 UT. Then the second pressure pulse causes the counterclockwise vortex beginning at 1854 UT. These downward field-aligned currents were collapsed soon by the convection patterns of opposite rotation. This is explained by the same story as the Araki94 SC model [*Araki*, 1994]. The enhancement of the dawn-to-dusk electric field in the magnetosphere after the abrupt compression causes the opposite convection patterns to break the first counterclockwise vortex pattern in the dusk hemisphere. Motion of vortices is not clear in Figure 4-22 and the scale size of the vortices is significantly large (twice or more) compared with that of the July-24 and May-27 MIE.

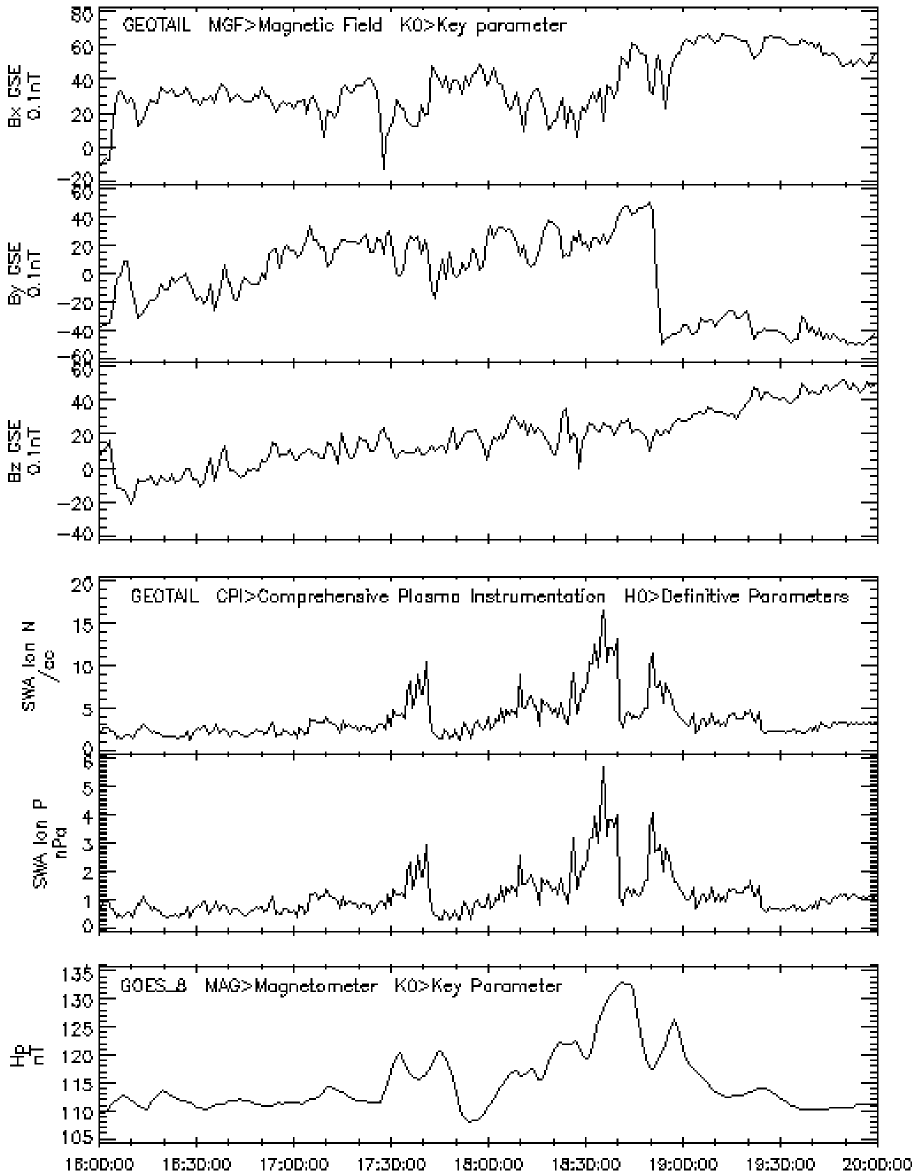

Figure 4-21. Geotail solar wind data and GOES-8 magnetic field data between 1600 and 2000 UT on July 30, 1998. From top to bottom, magnetic field variations in the GSE X, Y, and Z components, ion number density, dynamic pressure, and the geosynchronous magnetic field perpendicular to the orbital plain of GOES-8. The GOES-8 satellite moved from 11 to 15 MLT.

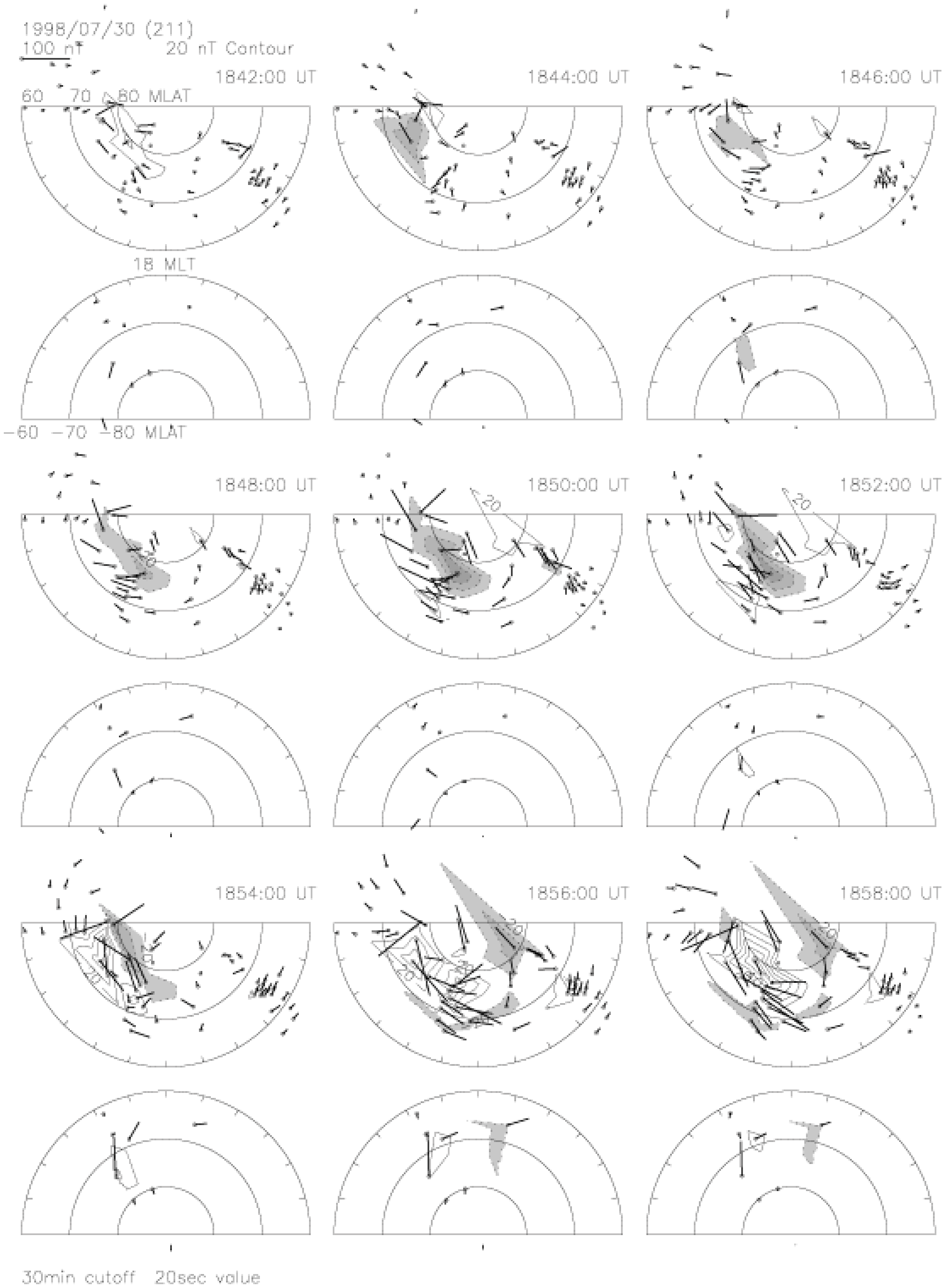

Figure 4-22. Equivalent convection plots at 2 min intervals from 1842 to 1916 UT July 30, 1998. Note that the northern and southern dusk hemispheres from 12 to 24 MLT are shown. Left (right) is 12 MLT (24 MLT).

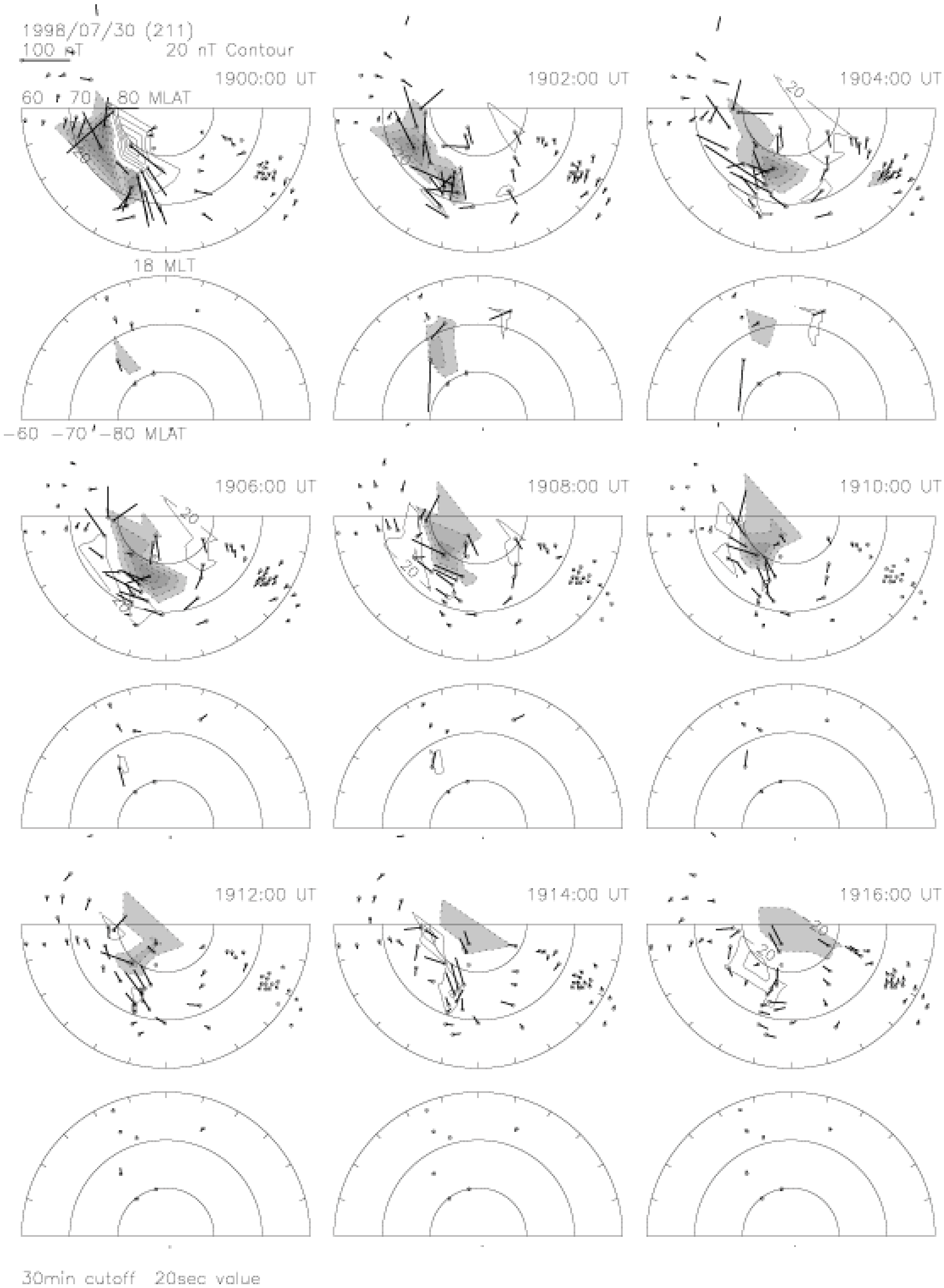

Figure 4-22. continued.

The difference between these two pressure pulses appeared in the auroral response. The first pressure pulse is ~150% larger than the second one. Nevertheless, auroral enhancement at SP occurred only for the second pressure pulse. The 630.0 nm auroral oval is stable near the poleward edge of the field of view at SP when the first pressure pulse strikes the magnetosphere. The enhancement of 630.0 nm aurora at 1903 UT is occurred when the upward field aligned current was added over SP ~5 min after the second pressure pulse compressed the magnetosphere. The enhancement of 427.8 nm aurora is very little for the MIE interval.

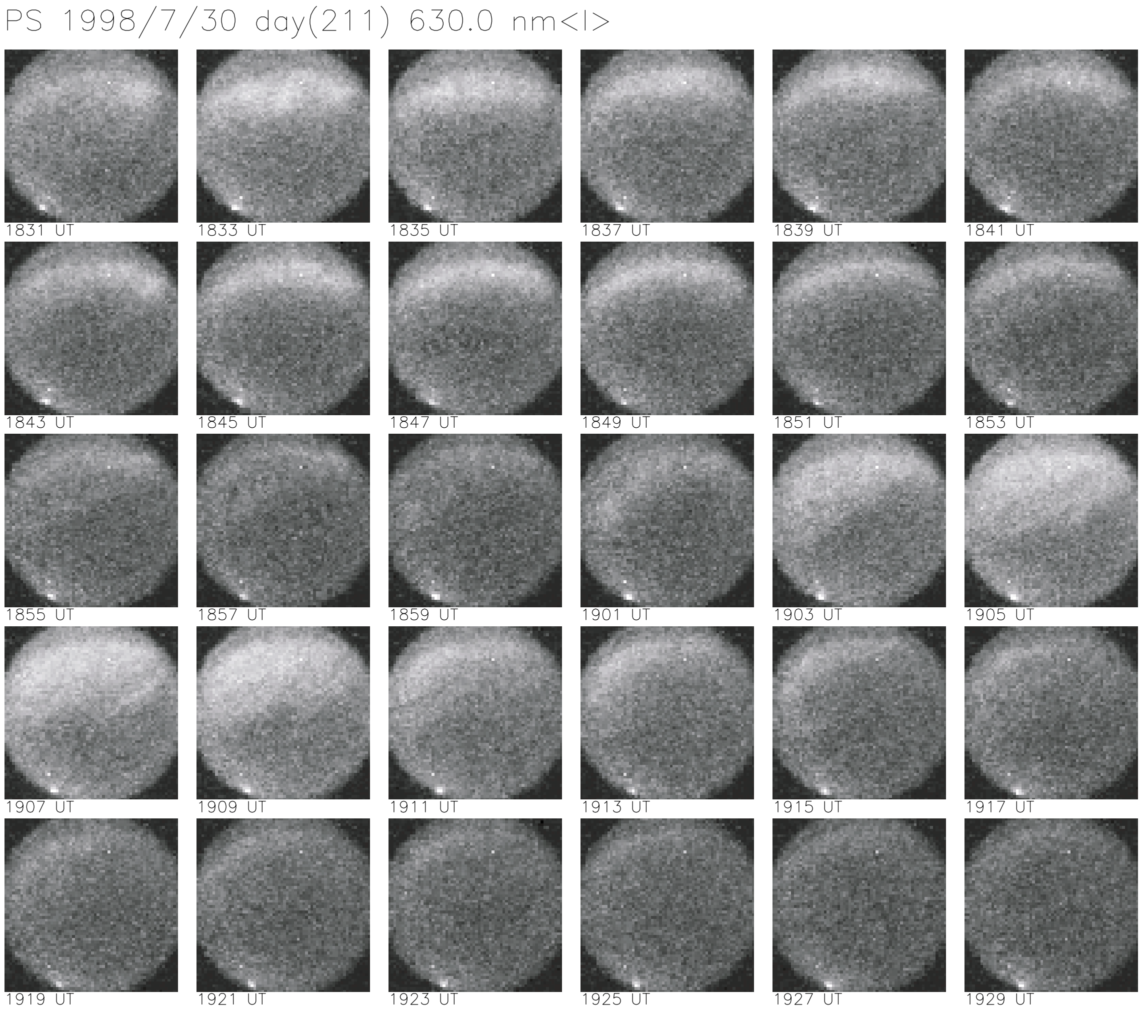

Figure 4-23. All-sky images between 1831 and 1929 UT on July 30, 1998. The format of each image is the same as Figure 4-5.

May 16, 1999 MIE

The equivalent convection pattern of this MIE is very simple. At first the downward current appeared around noon and moved eastward (1714-1718 UT). The following upward field aligned current appeared in the afternoon and moved tailward (1720-1728 UT) as shown in Figure 4-24. There is a good conjugacy in the northern and southern hemispheres in terms of the center of the vortex determined by eye.

Auroral activity is dominant in the wavelength of 630.0 nm images. The behavior of 630.0 nm aurora is very simple as shown in Figure 4-25. A narrow auroral arc appeared in the lower latitude side than the stable auroral oval. Then auroral oval expanded to equatorward from westward to eastward to fill the space between the narrow arc and the oval. This is almost consistent with the counterclockwise vortex motion with an upward field aligned current. It is interesting to note that *Mende et al.* [1990] also reported very similar MIE-related auroral response in the dusk sector in their fourth example.

The candidate trigger of this event is the southward excursion of IMF at 1622 UT observed at ACE, GSE (x, y, z) = (224.5, -0.6, -22.7). The corresponding southward excursion was observed by Wind (92.7, -33.2, -8.7) and Geotail (2.9, 29.9, -1.5) at 1643 UT and 1721 UT, respectively. The normal vector calculation by the 3-SAT method using a solar wind speed of (-380, -10, -10) km/sec in GSE coordinates resulted in the direction of GSE (x, y, z) = (-0.45, 0.43, -0.78), directed strongly duskward, antisunward, and upward. The MVA method was tried but the normal could not be determined for this event. This southward excursion reached the bow shock nose point, GSE (14, 0, 0) at 1709 UT, approximately 10 min before the ground onset of the MIE.

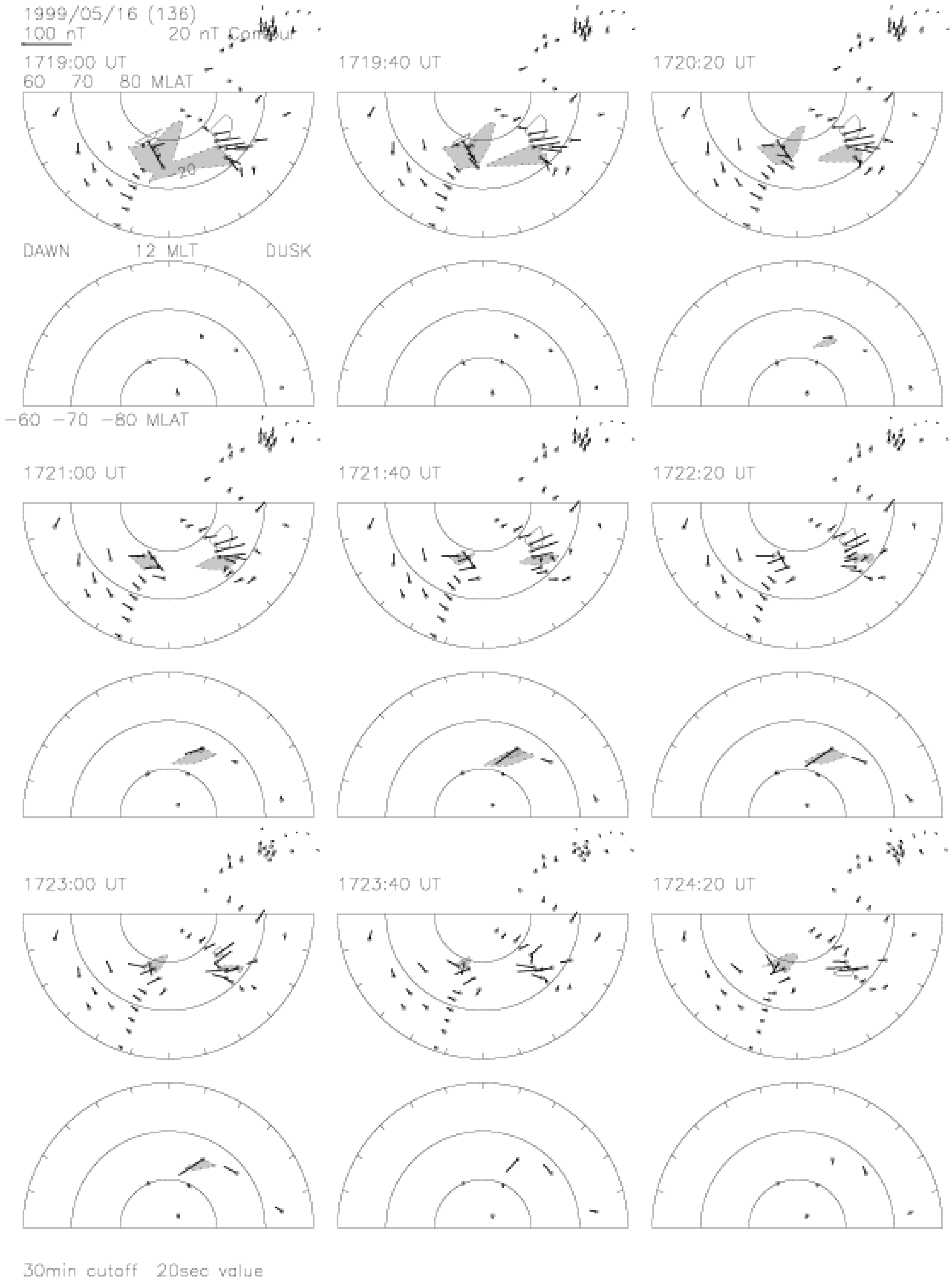

Figure 4-24. Equivalent convection patterns between 1719:00 and 1724:20 UT on May 16, 1999. The format is the same as Figure 3-5.

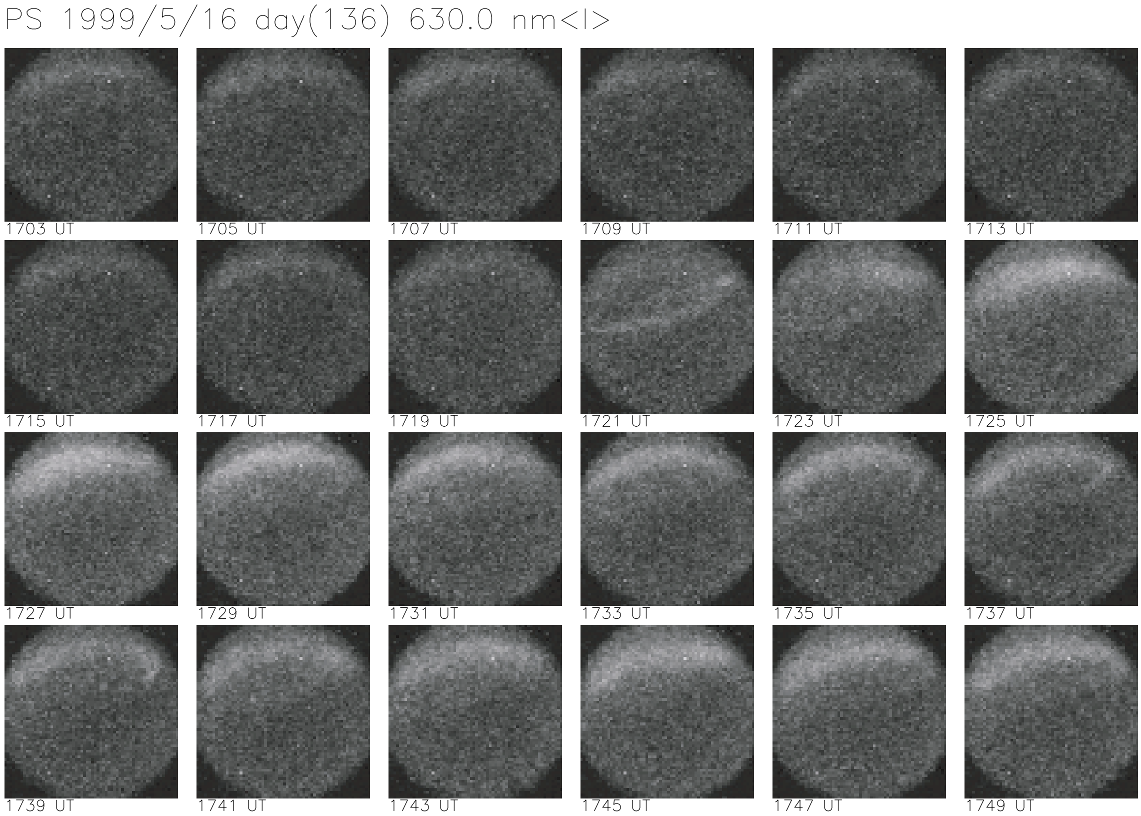

Figure 4-25. All-sky images at SP between 1703 and 1749 UT on May 13, 1999. The format is the same as Figure 4-5.

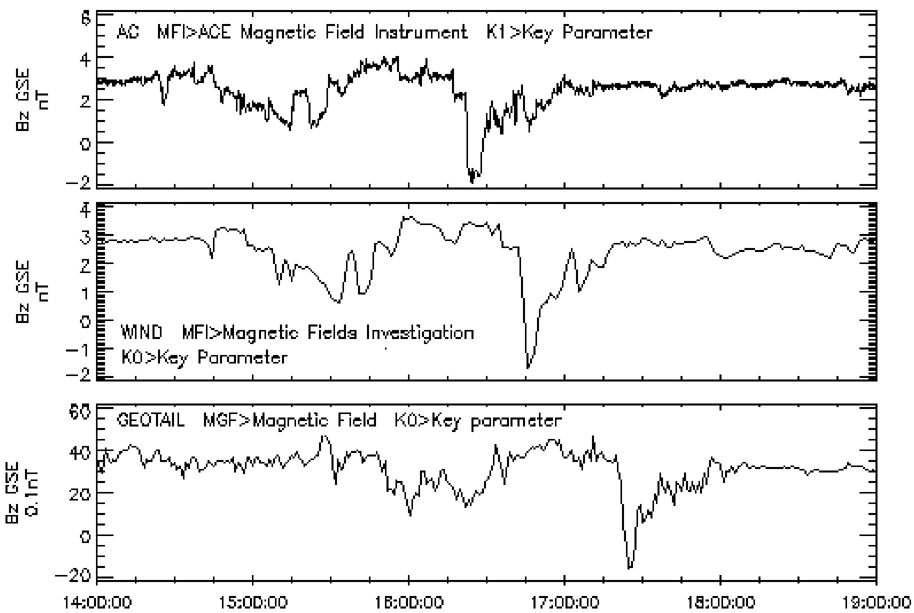

Figure 4-26. IMF B_Z data from ACE (top), Wind (middle), and Geotail (bottom).

May 25b, 1999 MIE

The CANOPUS magnetometer array in the dawn hemisphere observed the Pc5 wave train for the timing of the MIE. On the other hand, in the dusk side, equivalent convection pattern shows traveling convection vortices at the timing of the MIE (cf., Figure 4-27). Considering that the convection arrows of P3 directed the conjugate direction as Greenland SKT that is the approximately conjugate station of P3, there was conjugacy in terms of the motion of vortices in the dusk hemisphere. In the southern hemisphere, a clockwise vortex appeared over SP and P3 at 1812 UT. The next counterclockwise vortex appeared over SP and P3 at 1820 UT.

Auroral response to this MIE is very complicated. Three all-sky imagers were available in the southern hemisphere for this MIE interval on May 25, 1999. Figure 4-28 shows all-sky imager data obtained at SP. The SP imager observed tailward moving multiple arcs from 1815 UT when the next upward field aligned current vortex passed over SP. The enhancement and the motion of narrow transpolar arc were observed at P1 station simultaneously (cf., Figure 4-29). It is interesting to note that the DMSP IR imager confirmed that this transpolar arc existed before the MIE and continued to far nightside. The bright region of the arc is elongated along the arc from dayside auroral oval toward polar cap, beginning from 1313 UT. It is speculated that the enhancement of the 4-cell convection pattern due to the first TCV in the southern hemisphere may cause this enhancement and the propagation of the transpolar arc. The MM imager observed east-west aligned arc detached from stable auroral oval at 1811 UT near the equatorward edge of the field-of-view. This detached arc moved and disappeared at ~80° MLAT at 1817 UT (cf., Figure 4-30 and Figure 4-31).

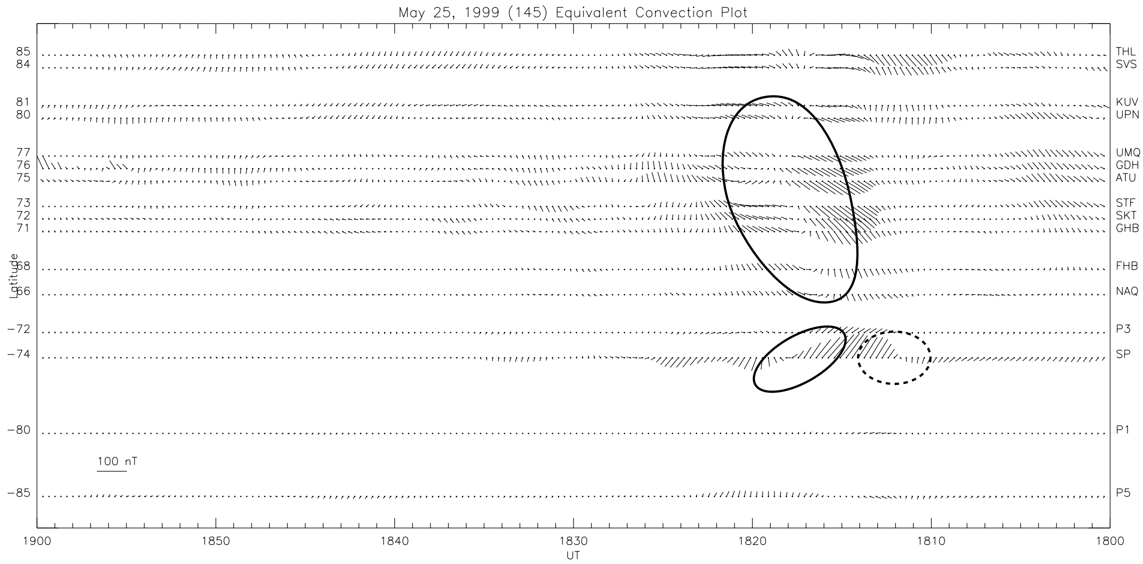

Figure 4-27. Equivalent convection pattern from 1800 to 1900 UT. Format is the same as Figure 4-13. Solid circles indicate the counter clockwise vortex, while a dotted line indicates the clockwise vortex that corresponds to the upward field aligned current.

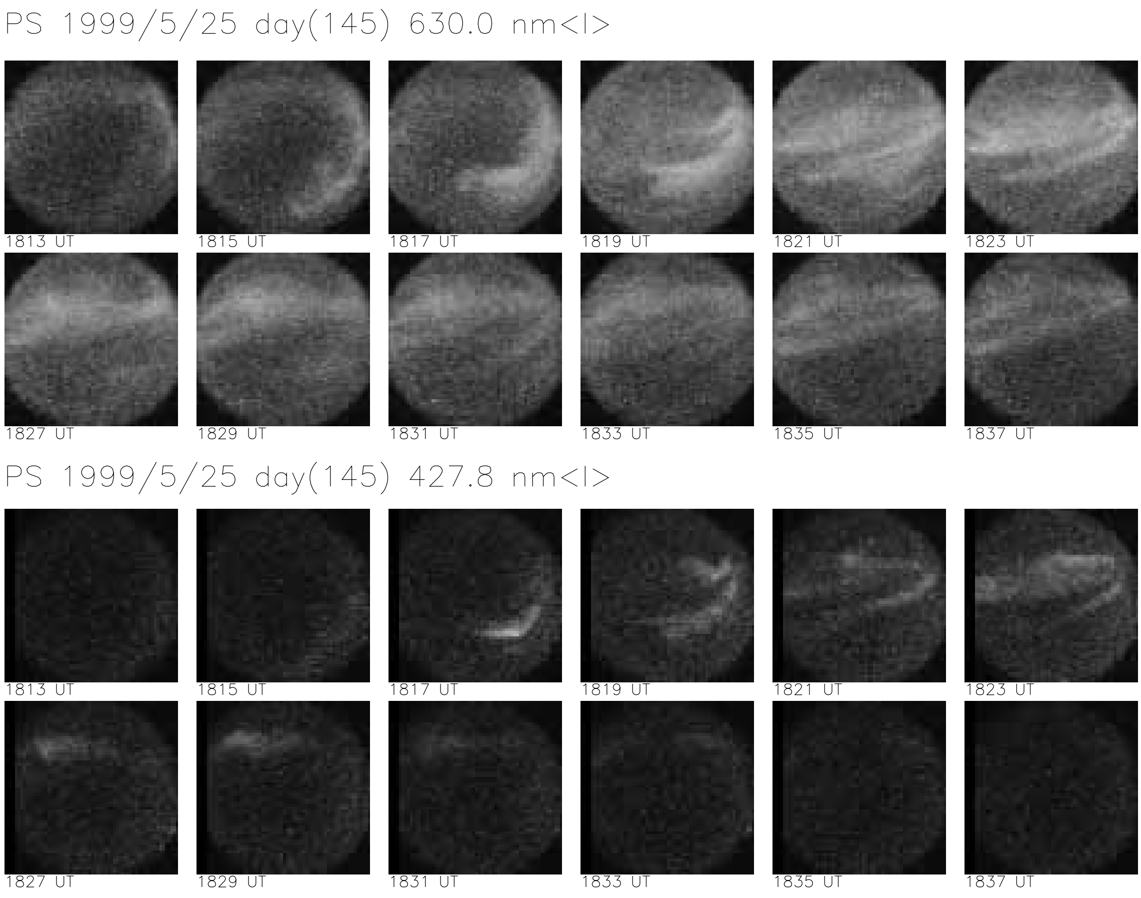

Figure 4-28. All-sky images obtained at SP between 1813 and 1837 UT on May 25, 1999.

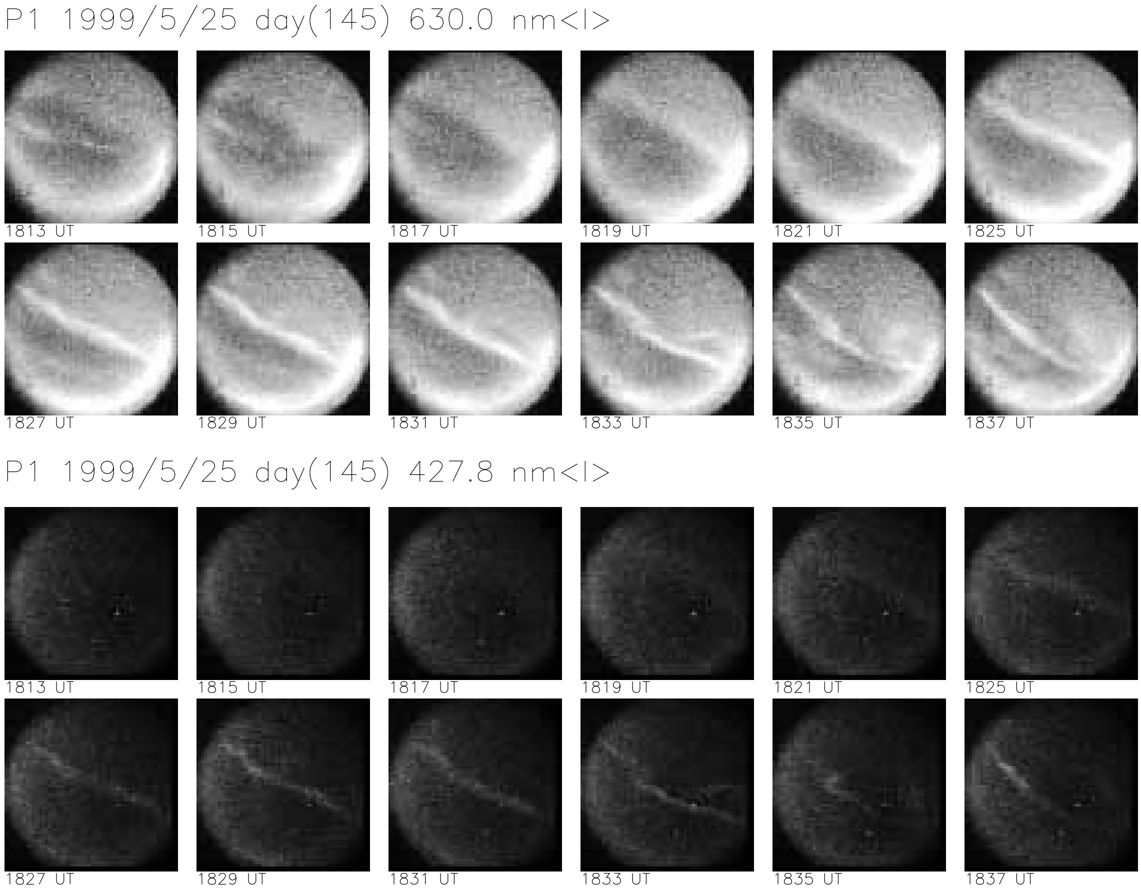

Figure 4-29. All-sky images obtained at P1 between 1813 and 1837 UT on May 25, 1999.

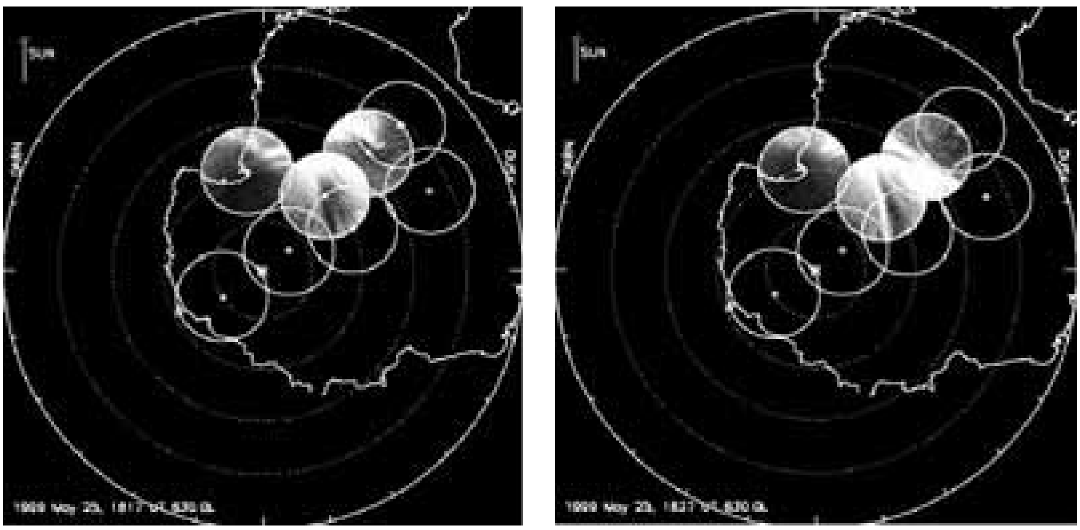

Figure 4-30. Projection images at 1817 (left) and 1827 UT (right) on May-25, 1999.

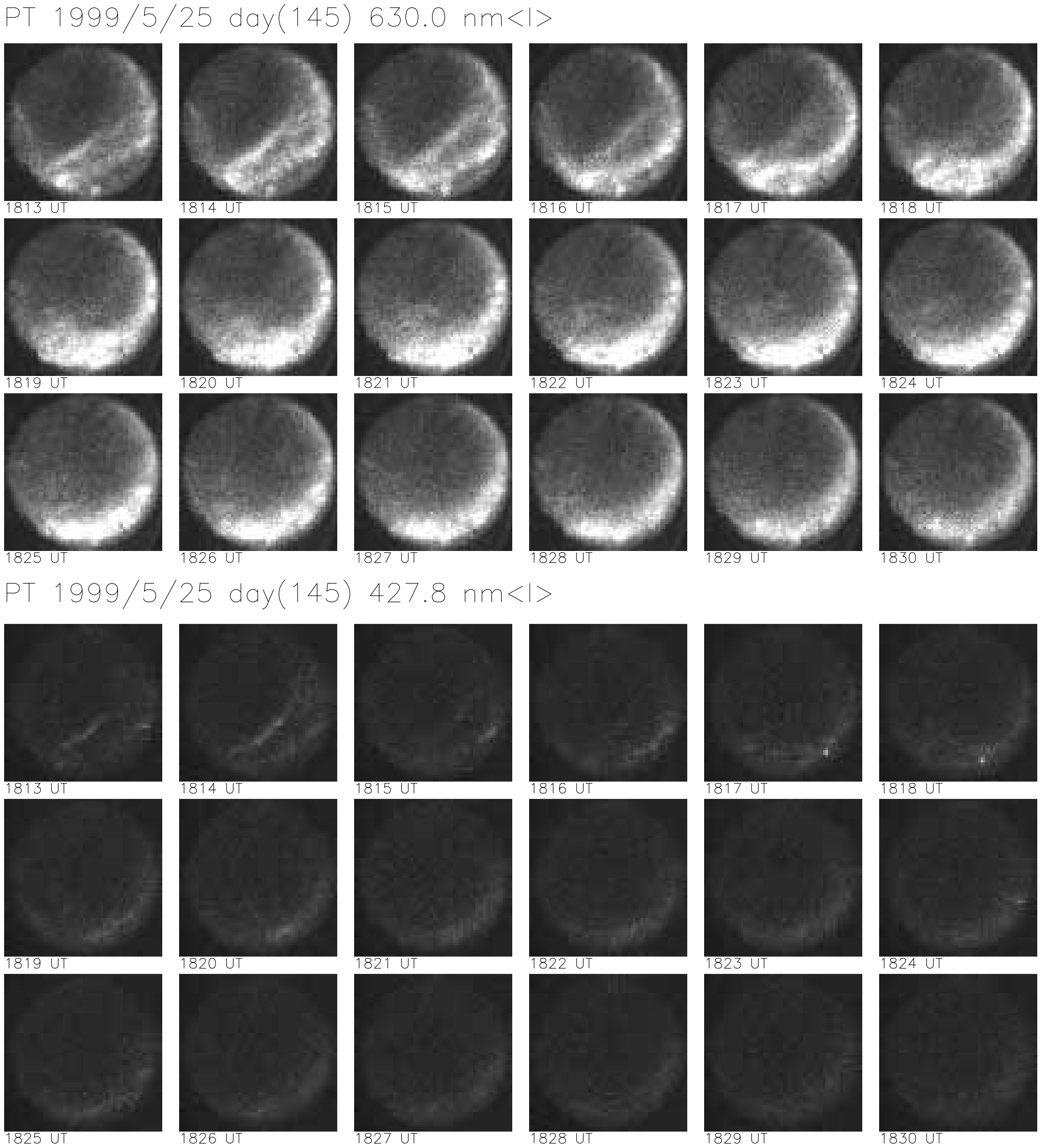

Figure 4-31. All-sky images obtained at MM between 1813 and 1830 UT on May 25, 1999.

ACE, IMP-8, and Geotail observed a sharp B_X change at 1715, 1758, and 1800 UT at the locations of GSE (x, y, z) = (224.2, 12.3, -22.5), (18.2, 10.9, -3.0), and (3.8, 32.6, -24.6), respectively (cf., Figure 4-32). Using the solar wind speed of GSE (x, y, z) = (-530, -20, -20), the normal vector is determined, GSE (x, y, z) = (0.77, 0.30, -0.56). The MVA method was tried but the normal could not be determined. This discontinuity propagated to the bow shock nose at 0802 UT, ~8 min before the onset of the MIE. The solar wind data show a very clear correlation between solar wind velocity and magnetic field in each component (cf., Figure 4-32 and Appendix). This is the typical characteristic of Alfvén wave. It is concluded that solar wind was filled by the Alfvén wave train around the MIE interval.

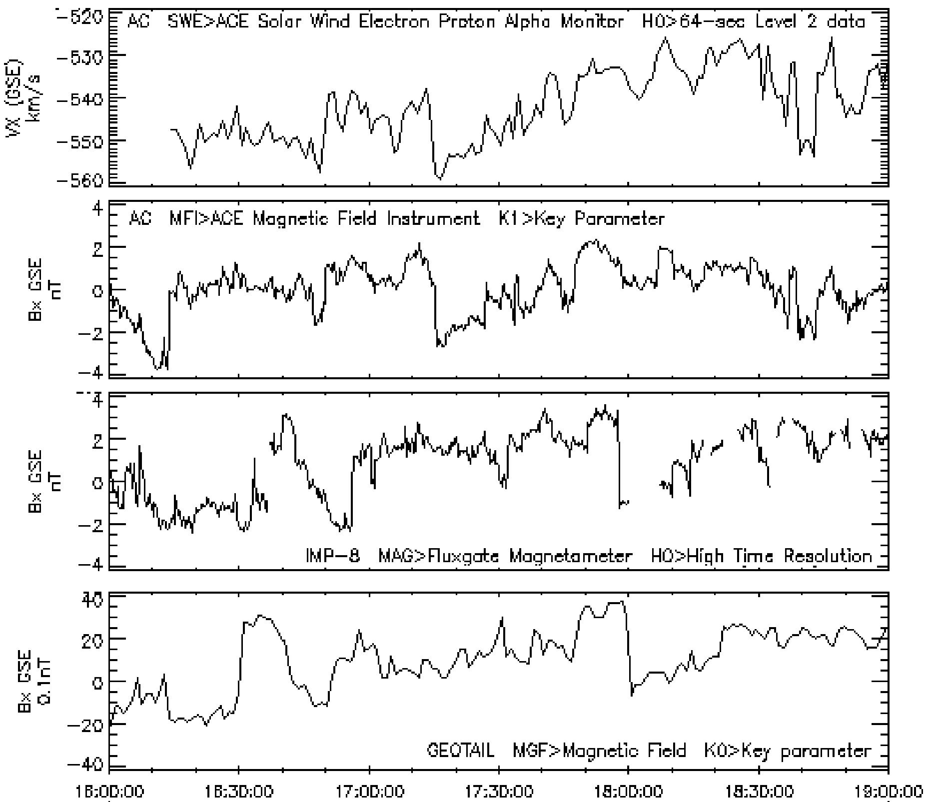

Figure 4-32. Solar wind data between 1600 and 1900 UT on May 25, 1999. From top to bottom, solar wind velocity V_X and IMF B_X obtained by ACE, IMF B_X obtained by IMP-8, IMF B_X obtained by Geotail in GSE coordinates.

4.5 MIEs related to SSCs

Three MIEs are related to the SSCs. A shock structure triggering each SSC is easily identified in the solar wind data for each MIE (cf., Appendix). The MIEs on May 3, 1998 (May-3 SSC) and June 13, 1998 (June-13 SSC) were observed in the dusk sector. The MIE on July 6, 1999 (July-6 SSC) was observed in the noon sector.

May 3, 1998 SSC

The result of the convection pattern analysis is shown in Figure 4-33. First, a counterclockwise vortex appeared in the dusk side in northern hemisphere at 1742 UT. Four minutes later at 1746 UT, the second clockwise vortex broke the first vortex. The motions of the guiding center of both the first and second vortices are not clear. Although it seems that the first vortex pattern has tailward propagation, it is difficult to determine the 'center' of the vortices because of its longitudinal large extension. The second large vortex corresponds to the field-aligned current out of the ionosphere in the dusk side. At the timing of the second clockwise vortex, auroras in the wavelength of 427.8 and 630.0 nm began to move equatorward rapidly at 1747 UT and were enhanced in the both wavelengths at 1751 UT (Figure 4-34). The equatorward motion of the auroral oval is consistent with the southward turning of IMF after the passage of the shock wave. It is interesting to note that *Mende et al.* [1990] reported very similar MIE-related transient auroral response with southward IMF but without SSC in their first example.

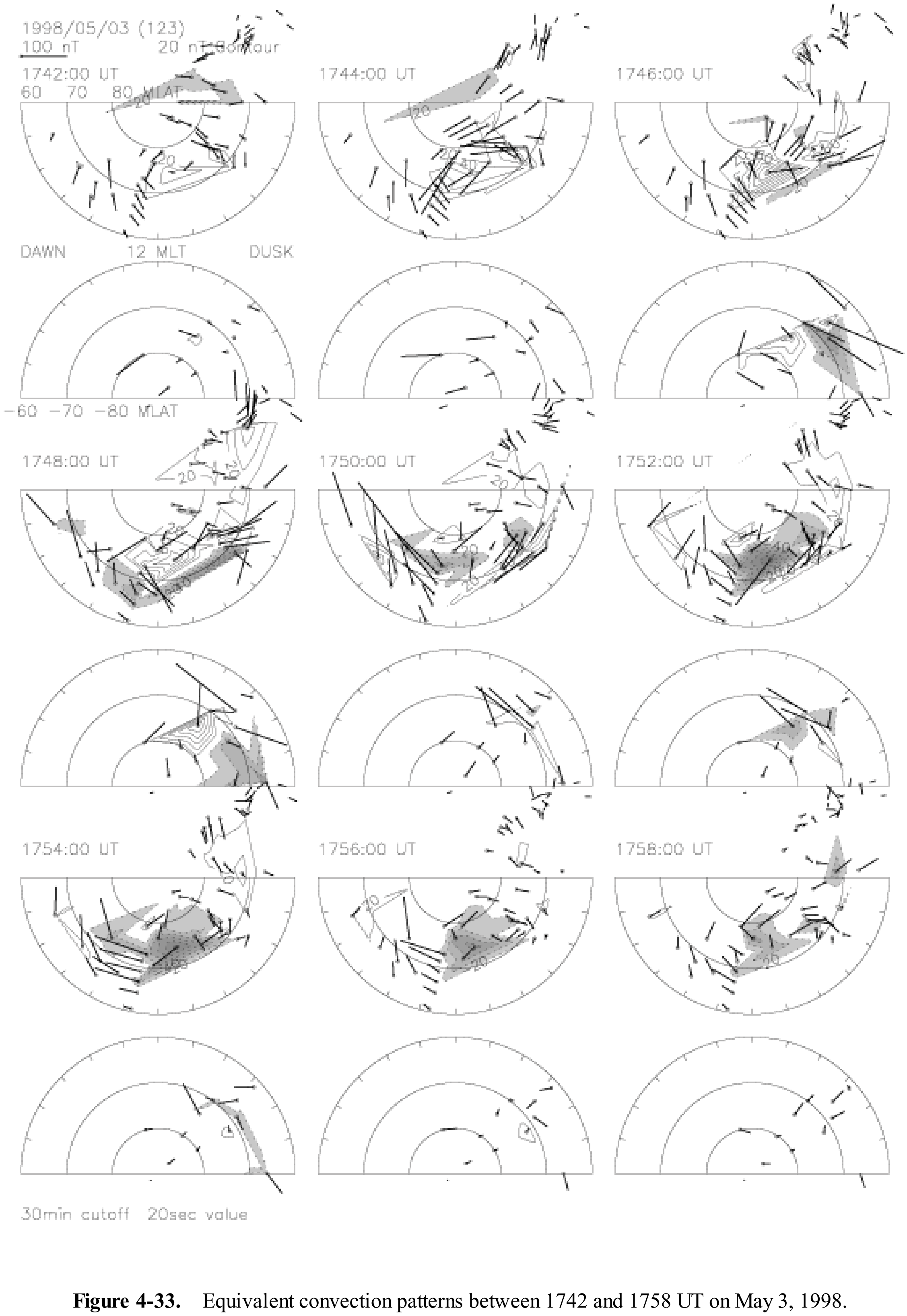

Figure 4-33. Equivalent convection patterns between 1742 and 1758 UT on May 3, 1998.

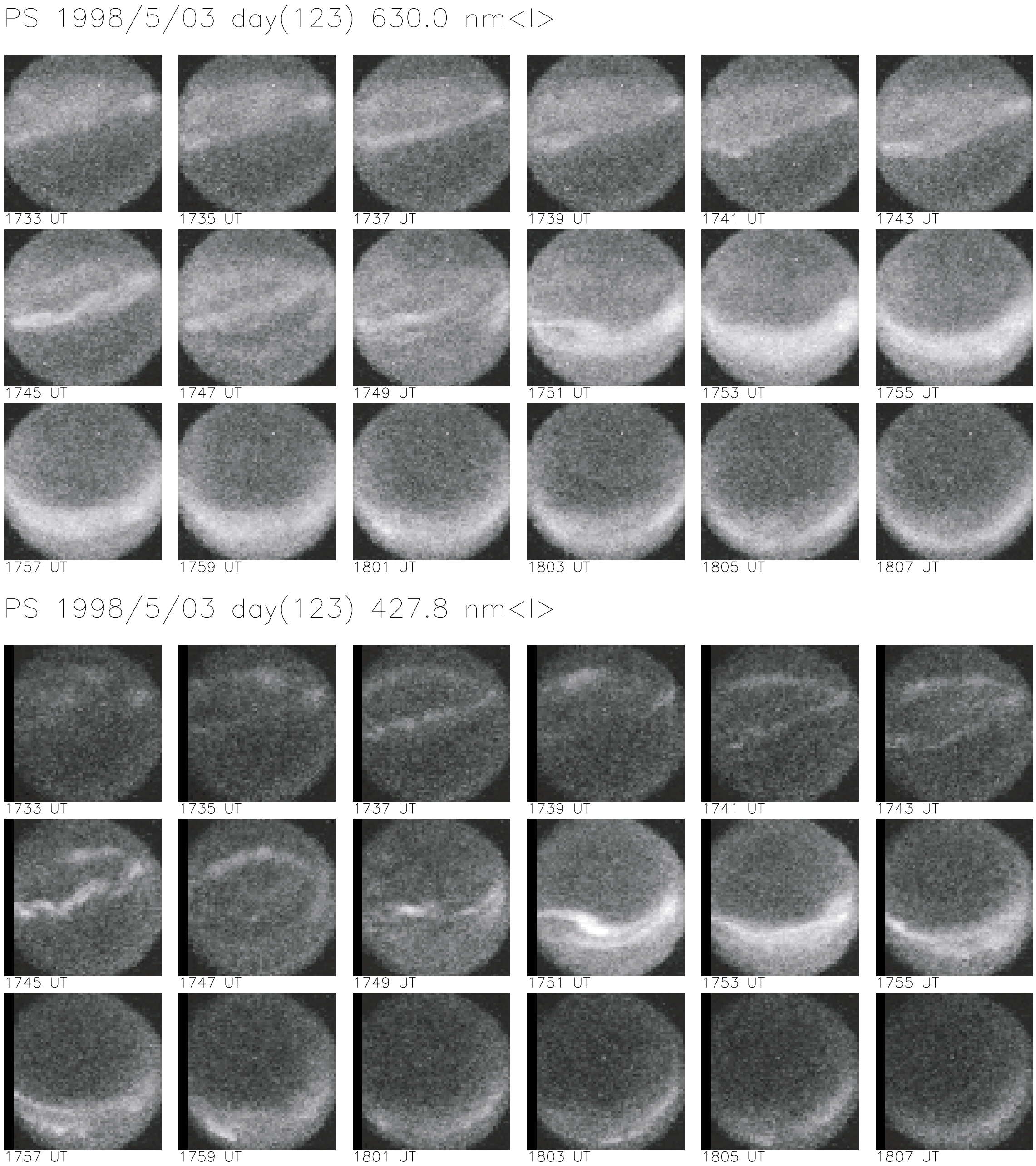

Figure 4-34. All-sky images at SP between 1733 and 1807 UT on May 3, 1999.

June 13, 1998 SSC

Figure 4-35 shows equivalent convection pattern on June 13, 1998. The characteristics of the convection pattern are similar to the May-3 SSC event. First, a counterclockwise vortex appeared in the dusk hemisphere at 1926 UT. Then 8 min later at 1934 UT, another clockwise vortex appeared and broke the first vortex. The motions of both the first and second vortices are not clear as the May-3 SSC event. The morphology of the enhanced aurora related to the upward filed-aligned current is significantly different from the case of the May-3 SSC event. The NIPR imager revealed that high structured auroral curtain was enhanced, with corresponding to the MIE timing (cf., Figure 4-36). The motion of the curtain is not clear. The 3-SAT method resulted that the normal of the shock wave is directed GSE (x, y, z) = (0.13, -0.45, 0.88). The shock wave would first hit the magnetosphere dawnside flank.

July 6, 1999 SSC

Network imaging observation was performed for this event. At the onset of the SSC, aurora around the cusp was abruptly enhanced in all wavelengths of 427.8, 557.7, 630.0, and 730.0 nm with almost without correlation with the upward field aligned current. Figure 4-37 shows the snapshot of geographical projected image. It is interesting to note that after this SSC, strange N-S aurora was observed equatorward of the cusp aurora in 557.7 and 427.8 nm.

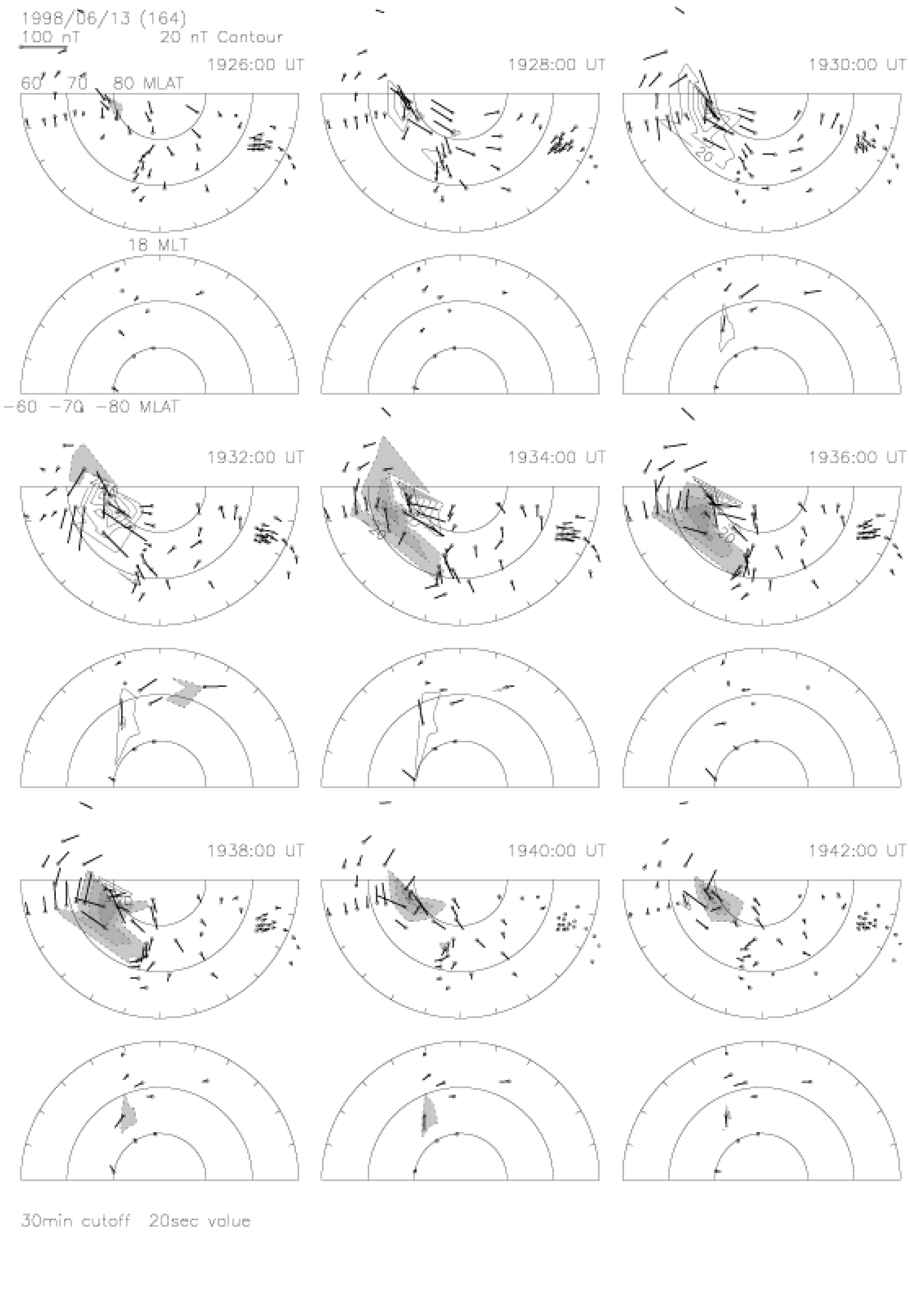

Figure 4-35. Equivalent convection plots between 1926 and 1942 UT on June 13,1998. Note that northern and southern dusk hemispheres are shown. Left (right) is 12 MLT (24 MLT).

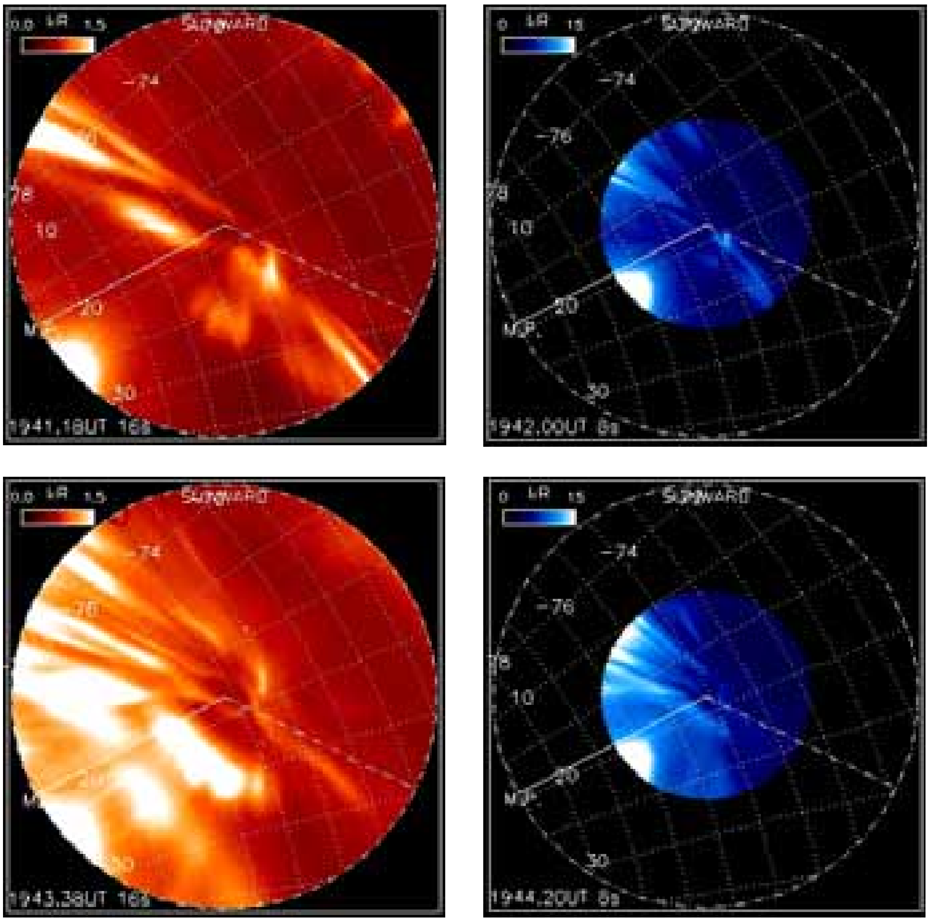

Figure 4-36. Mapped images colored in red (630.0 nm) and blue (427.8 nm) obtained at SP during the June 13, 1998 SSC event.

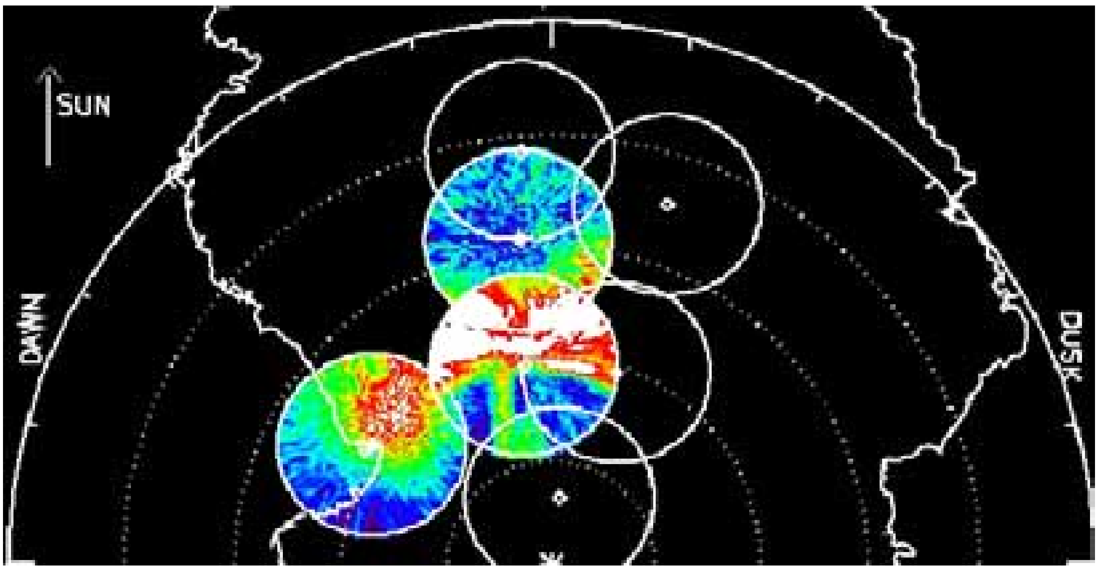

Figure 4-37. Image of 630.0 nm at 1511 UT on July 6, 1999.

4.6 Discussions

The main characteristics are summarized in Table 4-2 for each MIE. From left to right, the table contains the trigger, the GSE longitudinal angle of the discontinuity plane (θ = atan(n_X/n_Y), where **n** is the normal vector, positive dawnward from GSE X direction in degrees), changes of dynamic pressure (dP in nPa), IMF B_Z (dB_Z in nT, 'n': negative turning, 'p': positive turning) and the cone angle change (dCA in degrees) in the solar wind, auroral characteristics, the ratio of the intensity of 427.8 nm to 630.0 nm (Bl/Rd), and the motion of the guiding center of the convection patterns.

Table 4-2. A summary table of the multi event study.

Date	trigger	θ	dP	dB_Z	dCA	aurora	Bl/Rd	motion
Dawn sector								
96 July 24 (206)	TD	30	0	4p	20-80	short lived	8	tailward
99 May 25 (145)	TD	25	1+	2-	30-80	short lived	4	tailward
96 May 22 (143)	TD	20	1+	4p	60-20	short lived	7	tailward
Noon sector								
98 May 27 (147)	ST	10	0	2n	20-40	corona	0.3	duskward
99 July 3 (184)	TD	-5	0	3p	10-40	corona	0.1	duskward
Dusk sector								
99 May 16 (136)	ST	-45	1+	4n	30-50	oval	0.3	tailward
99 May 25 (145)	AT	70	0	2+	80-60	arcs	0.5	tailward
98 July 30 (211)	TD	-80	13+	1-	60	oval	0.5	not clear
SSC								
98 May 3 (123)	Shock	90	4+	5-	60-70	oval	1	not clear
98 June 13 (136)	Shock	-16	4+	7+	60-80	curtain	0.2	not clear
99 July 6 (187)	Shock	90	1+	5+	40-70	strange N-S	3	not clear

* TD: tangential discontinuity, ST: southward turning, and AT: Alfvén train.

In the dawn sector, the triggers of all three MIEs are tangential discontinuities (TDs) which have the normal direction of antisunward and duskward. Traveling convection vortices were produced at the timing of the MIE. Nevertheless the TDs accompanied by pressure changes, the TCV that is seen as MIE have relatively small ~1000 km scale length. This type of MIEs is clearly distinguished from SSC type MIEs which have a global scale response with twice or more larger vortices related to the MIEs, with almost no clear motion of the guiding center of the convection patterns. In Figure 4-38, a summary sketch of May-22 event is shown as a representative example of the MIE feature in the dawn sector. The solid circles C1, C2, and C3 show the locations of the guiding center of the clockwise vortex in the northern hemisphere at 1614, 1616, and 1618 UT respectively, while the dotted circles C0', C1', C2', and C3' show the corresponding locations for the counterclockwise vortices at 1612, 1614, 1616, and 1618 UT. The tailward motion of the twin vortex is shown by the westward movement of pairs of C1 and C1', C2 and C2', and C3 and C3'. There is a good conjugacy between the northern and southern polar regions.

All-sky images at the wavelength of 630.0 nm for the May-22 MIE are depicted as geographical projection plots in Figure 4-39. Basically, auroral activity was enhanced at the timing of the passage of upward field aligned current near the optical observation site. Note that at 1316 UT when 427.8 nm aurora was enhanced with 1-2 min duration above SP, the center of the upward current region (C2) was located very close to SP. However, auroral activity enhancements were also seen in the timing of the passage of downward field-aligned current following the upward field-aligned current. At 1612 UT, a relatively dark blob equatorward of SP was related to the C0' that is basically the center of the downward field aligned current region. After the passage of the clockwise vortex at 1618 UT, the auroral arc bended 90° and began to collapse.

The good conjugacy of northern and southern auroral activities is further confirmed by the Polar satellite looking down the northern polar region. Figure 4-40 shows the images obtained by Polar-UVI for the time interval of 1306:38 to 1331:10 UT on May 22, 1996. The individual images have an integration time of 36.8 sec and are taken in the wavelength range 160-180 nm through the longer-wavelength N_2 Lyman-Birge-Hopfield (LBH-long) filter. The intensity of auroral emission in this wavelength range is approximately range proportional to the total precipitating electron energy flux, with little sensitivity to the characteristic energy of precipitation [*Strickland et al.*, 1993; *Germany et al.*, 1994]. The images are mapped into geomagnetic polar coordinates. The image brightness is scaled logarithmically in units of photon flux (photons cm^{-2} sec^{-1}). The dayglow contribution to the images has been removed and pixel brightness is corrected for the line-of-sight effect. Note that the wobble degradation of images is still present in these data.

A clockwise vortex appeared at noon ~78° MLAT in the northern polar region at ~1312:40 UT when the brightest patchy UVI aurora was observed at noon ~78° MLAT in Figure 4-40. Then at the timing of the next image of POLAR satellite at ~1318:40 UT, a clockwise vortex was located centered at ~77° MLAT and ~9 MLT, near the location of the brightest patchy UVI aurora. These results confirm that the clockwise (counterclockwise) vortices well correspond to the upward field-aligned current in the northern (southern) hemisphere.

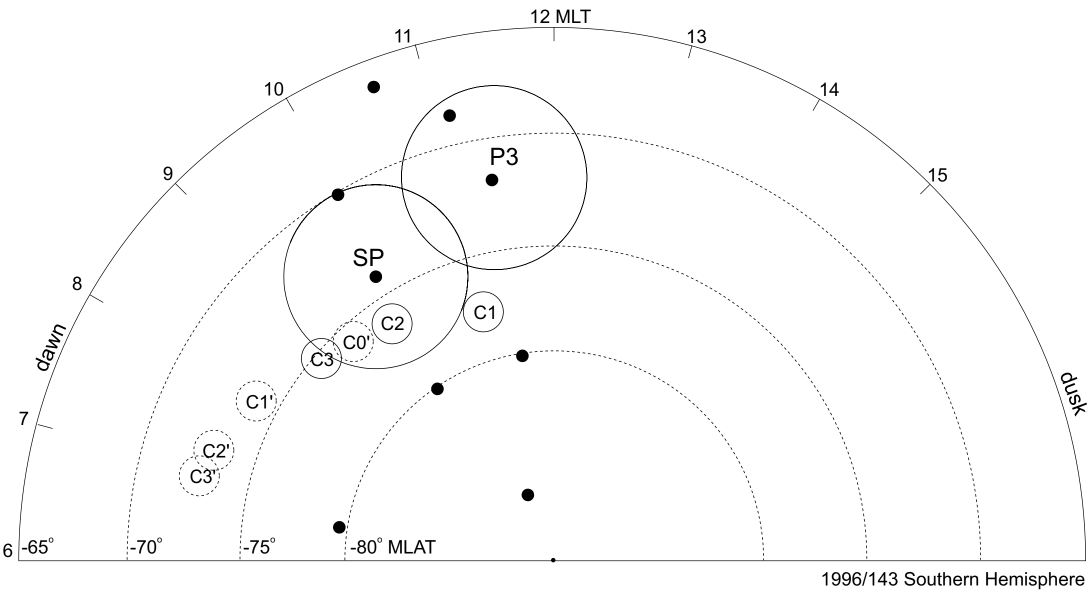

Figure 4-38. Schematic illustration of the MIE occurrence region and its movement on the geomagnetic polar map for the May-22 event. The guiding centers of the MIE/TCV derived from the horizontal magnetic perturbations are plotted as C1 to C3 for the clockwise vortex and C0' to C3' for the counterclockwise vortex.

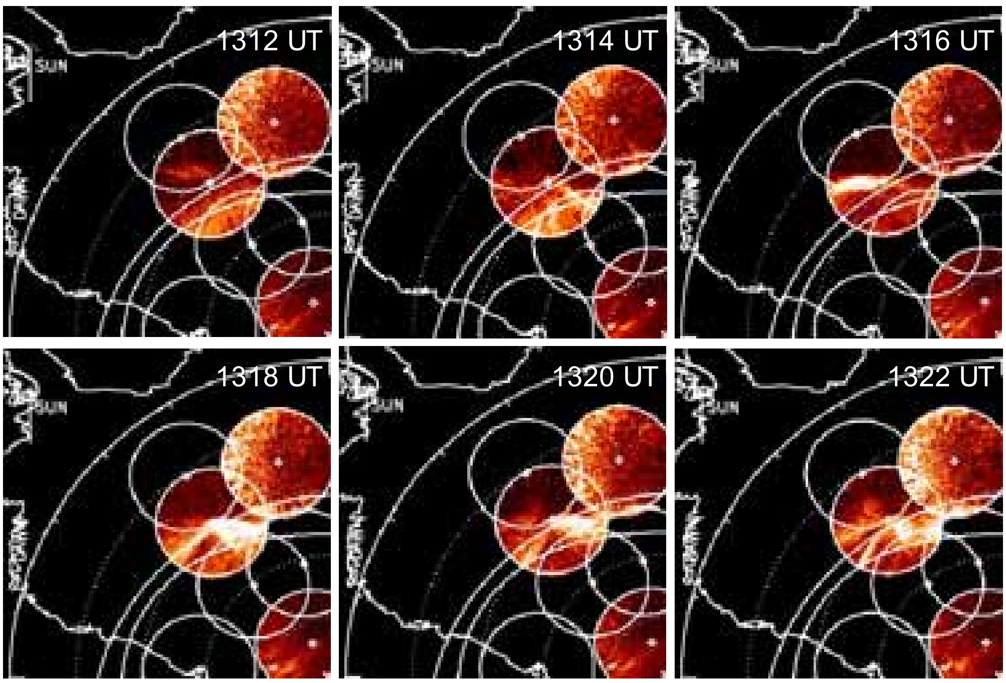

Figure 4-39. All-sky images of the 630.0 nm aurora seen overhead at SP, P1, and P5 at two min intervals from 1312 to 1322 UT on May 22, 1996.

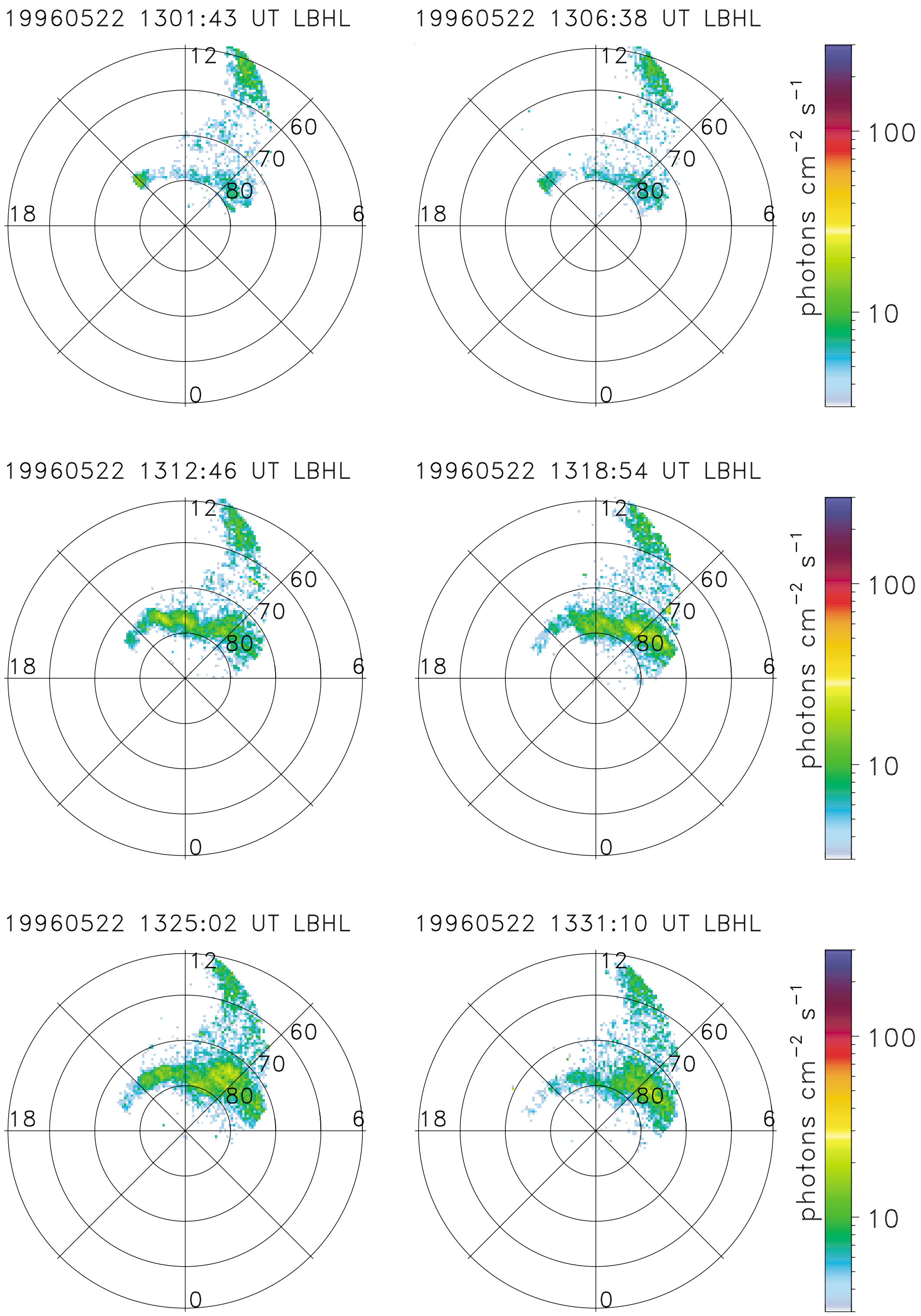

Figure 4-40. POLAR UVI images for the time interval of 1306:38 to 1331:10 UT on May 22, 1996. Individual images have an integration time of 36.8 sec and are taken through the LBH-long filter (160-180 nm). The images are mapped into geomagnetic polar coordinates.

The story above is almost consistent for the other two MIEs in the dawn sector. Figure 4-41 presents a series of UVI auroral images of July-24 MIE in the northern hemisphere with dayglow removed, transferred into polar geomagnetic coordinates as shown by *Sibeck et al.* [1999]. From 1107:04 to 1133:12 UT, postnoon aurora brightened and spread antisunward. Then, a prenoon brightening occurred near 10 MLT and 77° MLAT at 1139:20 UT and also spread antisunward. This brightening was stronger than the postnoon brightening and reached a maximum at 1145:28 UT. *Sitar et al.* [1998] reported the TCV field aligned current pairs observed by the Greenland magnetometers and intensification of the UVI aurora related to a hot flow anomaly (HFA). Localized intensification of higher energy auroral electron precipitation was observed at SP in Antarctica as the enhancement of 427.8 nm auroral emission and CNA. However, such enhancements were not observed at P3 or at the nominal conjugate locations IQA and STF [*Weatherwax et al.*, 1999].

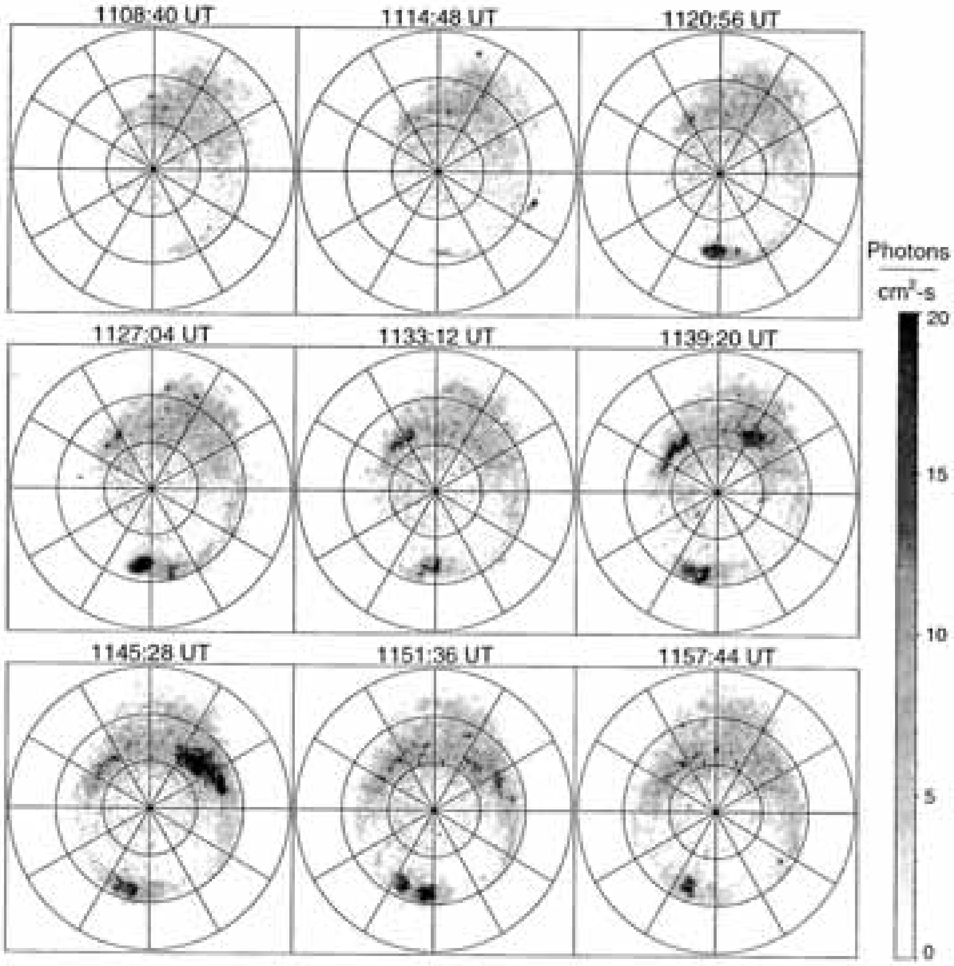

Figure 4-41. POLAR UVI LBH long (170.0 nm) image data from 1108:40 UT to 1157:44 UT on July 24, 1996. Local noon is the top of each image, and dawn is right. Latitudinal circles are drawn at 60°, 70°, and 80° N geomagnetic latitudes [from *Sibeck et al.*, 1999].

The relatively good conjugacy implies that TCVs occur within the closed field line region. Considering that all TCVs propagate tailward at a maximum speed of ~10 km/sec at Earth's surface and consist of twin or triple TCVs, it is concluded that the surface wave of the magnetopause could make these MIEs in the dawn sector. It is known that the interaction between TD and the bow shock could make a significant deformation of the magnetopause by abrupt pressure enhancement or abrupt pressure decrease [e.g. *Lin et al.*, 1996, 1997; *Sibeck et al.*, 1998, 1999]. The HFA observed on July 24, 1996 is one of such interactions between TD and the bow shock. HFA is produced when the TD is parallel to the BS normal vector [*Lin et al.*, 1997]. The orientation of the normal vector of the TD is similar for the three MIEs in the dawn sector. It is possible that the three MIEs in the dawn sector could be the result of the field-aligned current caused by the abrupt deformation of the magnetopause not only by the pressure pulse accompanied by the TD and also the TD-BS interaction such as HFA formation. Including the generation condition of HFA, the orientation of TD (20°-30° duskward from the GSE X positive direction) and/or the large cone angle change may be key points in the generation of MIEs and related phenomena such as high-energy particle precipitation with a short duration in the dawn sector.

The MIEs in the noon sector have definitely different characteristics as the MIEs in the dawn sector. The auroral activity is dominant in 630.0 nm. The intensity ratio of 427.8 nm aurora to 630.0 nm aurora is relatively low (usually 0.05-0.2). The enhancements of CNA are also very weak, slightly above the noise level (usually ~0.05 dB). These observations imply that low energy (less than several 100 eV) particle precipitation is dominant. The enhancement of auroral activity is corresponds to almost the timing when the counterclockwise vortex passes over the field of view of the SP imager. This suggests that the vortex connected to the upward field aligned current is related to auroral activity enhancements. The upward field aligned current is mostly originated in the dawn hemisphere and moves eastward (toward dusk) across the noon meridian. The scale length of the MIE/TCVs in the noon-sector is ~1000 km, almost the same scale as MIE/TCV in the dawn-sector. The interesting point is that all of these characteristics of MIEs in the noon sector are seen in the June 6, 1997 event described in the Section 3.1.

In Figure 4-42, a summary sketch of the May-27 event is shown as representative example of the MIE feature in the noon sector. The circles C1-C4 are the mapping to the southern polar region of the guiding centers of TCVs determined in the northern hemisphere at two min intervals from 1606 to 1612 UT. The guiding center of the TCV moved eastward and poleward across the noon meridian. Figure 4-43 shows all-sky images of the 630.0 nm aurora observed at SP and MM. Unfortunately, MM was cloudy at the timing of the MIE. As seen in Figure 4-43, 630.0 nm corona aurora appeared ~4 min later, centered at C1-C4. The convection pattern also indicates this 4 min time delay as shown in Figure 4-16. It is concluded that the center of the TCV was significantly deviating between the northern and southern hemispheres for this event. It is possible that the large X-component of IMF caused such a north-south asymmetry. For example, the location of the merging process at the dayside magnetosphere shifts north or south significantly depends on the IMF X-component.

The May-27 MIE could be originated in significantly low latitude ~73° MLAT, which may correspond to the 'void' or central plasma sheet (CPS) region as observed by DMSP satellites [e.g., *Newell et al.*, 1992]. *Lyatsky and Sibeck* [1997] proposed a mechanism of CPS disruption model, which has the origin in the outer boundary of CPS and could cause the formation of dayside poleward moving auroral events in the closed field line. According to this mechanism, the outer boundary of the CPS could be the unstable region with respect to the interchange (ballooning) instability. There are many pressure pulses at the timing of the May-27 MIE. It is speculated that the pressure pulses might be the trigger of the instability in the outer boundary of CPS.

The cone angle of the solar wind IMF is very small (~20°) in the period before the onset of MIEs in the noon sector. This implies that the geometry of the bow shock is in the quasi-parallel shock (QPS) conditions. It is possible that satellites missed the trigger of this kind of MIEs frequently. Even if there was no pressure pulse in the solar wind medium, it is possible that pressure pulse could be produced in the magnetosheath or ion foreshock region in such QPS conditions. Moreover, the small cone angle makes it difficult to determine the time lag from satellites to the magnetosphere.

Contrary to this, the source of MIEs related to SSCs is clearly identified as interplanetary shocks. The global simultaneous occurrence, including even GOES satellites, with clear onsets are the main characteristics distinguishing MIEs related to SSCs from other MIEs. It was shown that most of the convection patterns of SSC related MIEs could be explained by the Araki94 model [*Araki*, 1994].

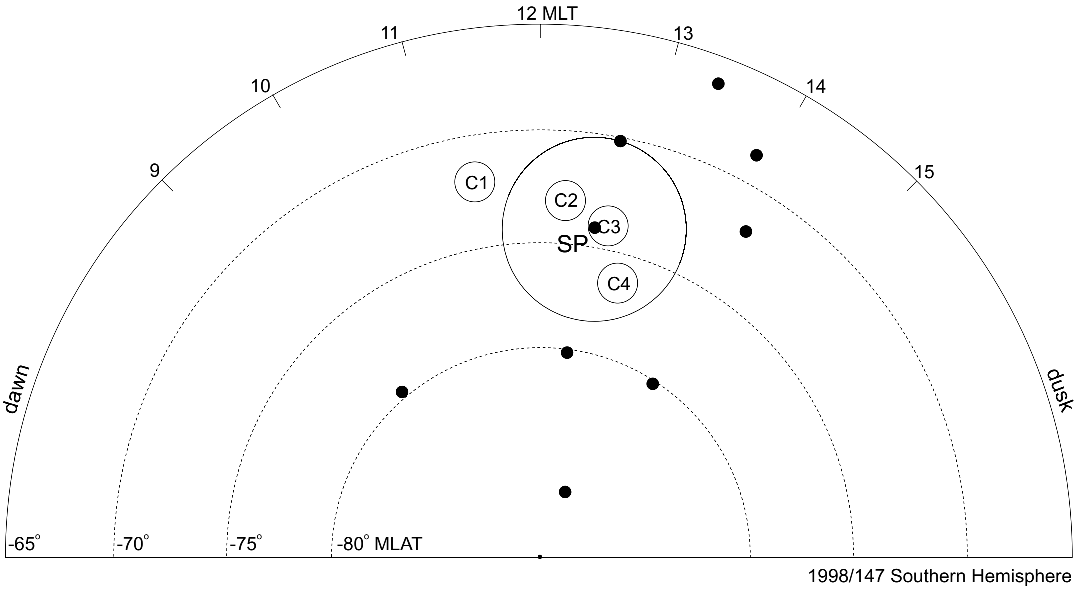

Figure 4-42. Schematic illustration of the MIE occurrence region and its movement in the geomagnetic polar map for the May-27 event. The guiding centers of the MIE/TCV derived from the horizontal magnetic perturbations are plotted as C1 to C4.

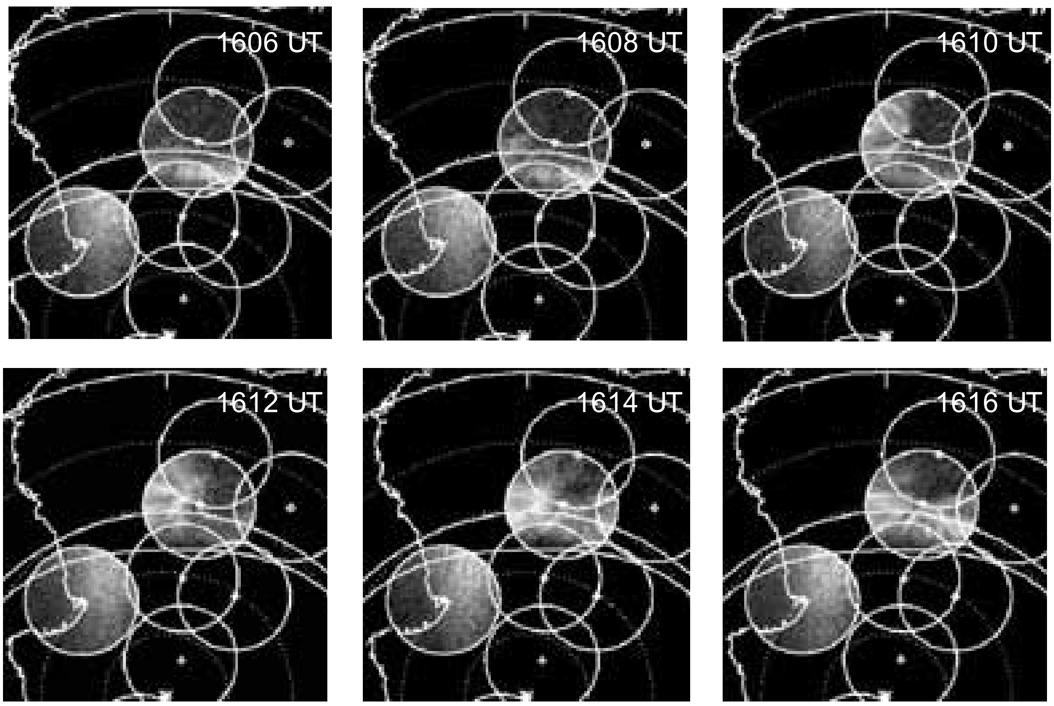

Figure 4-43. All-sky images of the 630.0 nm aurora at two min intervals for 1606-1616 UT on May 22, 1996.

According to the Araki94 model, the dawn to dusk magnetopause current (J_M) is enhanced first when the dynamic pressure increases. The enhanced magnetopause current (J_M) and the polarization current (Jp) along the compressional wavefront form a current loop inside of which the northward magnetic field increases. When the wavefront reaches the earth, the H-component of the ground magnetic field begins to increase. This abrupt H-component increase is called SC (sudden commencement) in general as it is observed at magnetometers in low latitudes. The inhomogeneity of the magnetospheric plasma and magnetic field produces Alfvén mode wave which propagates along field lines to the polar ionosphere. The wave accompanies a field-aligned current (J_F) which flows into the ionosphere on the dusk side and out of the ionosphere on the dawn side. This field-aligned current produces ionospheric currents of the twin vortex type which are clockwise in the afternoon over the northern hemisphere and counterclockwise in the morning, as shown in Figure 4-44(A) [*Araki*, 1994].

After the passage of the compressional wavefront toward the magnetotail, the magnetospheric convection has to adjust to the new compressed state of the magnetoshpere if the dynamic pressure of the solar wind remains high behind the shock or discontinuity. The convection electric field in the dawn-to-dusk direction has to be enhanced in the compressed magnetosphere. The associated field aligned current flows into the dawn ionosphere and out from the dusk ionosphere as shown in Figure 4-44(B). Then a twin vortex current with opposite sense to the preceding current system appears in the ionosphere.

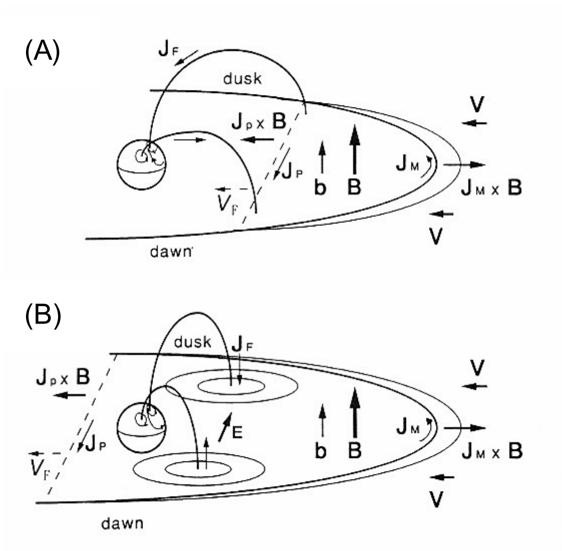

Figure 4-44. A schematic illustration of the model for SC [from *Araki,* 1994].

The predicted twin vortices were clearly found in Figure 4-33 and Figure 4-35 as mentioned in Section 4.5 already. The scale size of the MIEs related to SSCs is of course large with a global-scale extension. Main auroral enhancement at SP occurred in the timing of the upward field-aligned current. The morphology of the aurora varies depending on MLT and IMF direction embedded in the shock wave structure.

The similar response as SSCs was found in the July-30 event. For this case, the first density pulse could not produce MIEs which fulfilled the LJL91 criteria. The second pressure pulse accompanied by the tangential discontinuity (TD) made the LJL91 MIE nevertheless the pressure increase is 150% larger for the first pressure pulse than the second one. Recently, *Chen et al*. [2000] simulated the interaction between this kind of TD, across which the plasma density increases, and dayside magnetosphere including the bow shock passage. It was shown that the TD/bow shock interaction produces TCV signatures on the ground [*Chen et al.*, 2000]. The July-30 event may be a typical example of such pressure pulse mechanism of *Chen et al.* [2000].

Chapter 5

Summary and conclusions

5.1 Summary of a case study of a MIE

A magnetic impulse event (MIE) on June 6, 1997 was investigated using ground and space based omnivorous data sets including observations of Automatic Geophysical Observatories (AGOs) in Antarctica. The result of conjugate analysis using magnetometer network data in northern and southern high latitudes was reported for the first time in this thesis. The analysis of simultaneous observation data of aurora, CNA, and HF backscatter was also performed at first as to the motion of traveling convection vortex (TCV) accompanied by the MIE. The main results are summarized as follows.

1) The TCV was initiated at 10 MLT and 78° MLAT in the low latitude boundary layer. The motion of the TCV was eastward (toward dusk) and slightly equatorward across the noon meridian with a traveling velocity of 1-3 km/sec at the Earth's surface. The TCV has conjugate guiding centers in the northern and southern hemisphere.

2) All-sky cameras observed the 630.0 nm aurora following the motion of the TCV guiding center with 2 min time delay. It was found that the upward field aligned current was located near the rear edge of the Hall current loop rather than the center of the loop. The imaging riometer only at SP observed the similar motion of a weak cosmic noise absorption event. This MIE-related CNA may imply F-region electron density enhancement by localized soft electron precipitation.

3) There were no abrupt changes in dynamic pressure or interplanetary magnetic field (IMF) that could be the direct trigger of the MIE. The IMF showed strongly outward (-5 nT) B_X, slightly positive (1-2 nT) B_Z, and nearly zero B_Y orientation in GSM coordinates. The classical generation mechanisms of MIEs such as dayside reconnection, pressure pulse, Kelvin-Helmholtz instability, and plasma penetration are excluded for the candidate mechanisms for this MIE.

4) Although the origin of this MIE is not clear, it is speculated that the abrupt cone angle change from 60° to 20° at ~30 min ahead the onset timing may be the indirect trigger of this MIE via the interaction between the solar wind and the bow shock. A rapid change of foreshock geometry into the quasi-parallel shock structure could be produced by such IMF rotation.

5.2 Summary of a multi event study of MIEs

A multi event study of MIEs was executed in order to investigate the characteristics of MIEs in terms of solar wind triggering, auroral activity, and the north-south conjugacy of TCVs. MIEs with more than 100 nT amplitude in the vertical component were selected by applying the LJL91 criteria to South Pole fluxgate magnetometer data in 1998 and 1999. Then 9 events with distinct triggering signatures in the solar wind plasma and magnetic field were selected. Three events were related to the SSC. The remaining 6 events and two more MIEs in the literature were categorized into dawn (8-10 MLT), noon (11-13 MLT), and dusk (14-16 MLT) sector events. MIEs in the dawn and dusk sector have some tendencies in auroral responses and the motion of the TCVs. Three of total 11 MIEs were related to the SSC. The main results are summarized as follows.

1) In the dawn sector, it is found that twin or triple TCVs moved tailward with a good north-south conjugacy. The tailward motion of the TCV guiding center has at a maximum speed of ~10 km/sec at the Earth's surface. The scale length between twin vortices is 1000-1500 km. Hard electron precipitation with short duration (1-5 min) was observed with 427.8 aurora at the timing of the upward field-aligned current. The trigger of the MIEs is identified to be the tangential discontinuity with an orientation of 20°-30° duskward from the GSE X positive direction.

2) In the noon sector, TCVs moved eastward across the noon. The motion of the guiding center had a maximum speed of ~5 km/sec at the Erath's surface. The scale length between twin vortices was ~1500 km. The north-south conjugacy of TCV somewhat collapsed in the May-27 event in which there was ~4 min time delay between northern and southern hemispheres. Corona-shaped 630.0 nm aurora due to soft electron precipitation was observed with eastward motion. Auroral activity was enhanced in the upward field aligned current region. The IMF had very small cone angle (10°-20°) and it implies that quasi-parallel shock structure may play an important role in the generation mechanism of MIEs in the noon sector.

3) Three MIEs related to SSCs were analyzed. After the first counterclockwise vortex appeared in the dusk side of the northern hemisphere, the second clockwise vortex broke the first vortex. These phenomena are interpreted by the preliminary impulse (PI) and the main impulse (MI) of the Araki-94 model. The vortices had global extension. Main auroral enhancement at South Pole station occurred at the timing of the convection vortex accompanied by the upward field-aligned current.

5.3 Conclusions

We tried to analyze magnetic impulse events (MIEs) with ground and space based omnivorous data sets to elucidate the evolution and generation mechanisms of MIEs. We obtained the following with respect to the conjugacy of traveling convection vortices (TCVs), MIE related auroral activities, and solar wind sources of MIEs.

1) Most of TCVs accompanied by MIEs have conjugate guiding centers in northern and southern hemispheres in CGM coordinates. However, the north-south conjugacy collapses when IMF points strongly radial direction.

2) MIE related aurora is enhanced at the timing of the passage of TCV accompanied by the upward field-aligned current. The characteristic energy and the shape of MIE-related aurora depend on magenetic local time. Basically, MIE-related aurora appears in lower latitude (72°-77° MLAT) than the dayside auroral oval. It is also found that sun-aligned arcs are often observed in higher latitude (78°-83° MLAT) than the dayside auroral oval at the timing of MIEs.

3) The local time dependence on the occurrence of MIEs is controlled by the orientation of the interplanetary discontinuity plane triggering the MIE. It is suggested that the interaction between the solar wind and the bow shock plays an important role. The trigger of MIEs may occur near the bow shock when the quasi-parallel shock structure exists.

We suppose that the characteristic feature of many aspects of MIEs analyzed and clarified in this study will help in understanding the generation mechanisms of MIEs and more general transient responses of the magnetosphere to various solar wind changes.

Appendix

Key Parameter data of the CDA Web (http://cdaweb.gsfc.nasa.gov/) are used to plot solar wind parameters. All traces are plotted by using coarse noise filtering to remove values outside 3 deviations.

WI_K0_SWE: Wind Solar Wind Experiment, Key Parameters (~90 sec)

- K. Ogilvie (NASA GSFC)

AC_H0_SWE: ACE/SWEPAM Solar Wind Experiment 64-Second Level 2 Data

- D. J. McComas (Los Alamos National Laboratory)

N: Proton number density in units of cm-3

P: Dynamic pressure (nMV^2, where n is the density, V is the velocity, and M is the mass of a proton) in units of nPa.

H temp (Ace): Radial component of the proton temperature in units of Kelvin.

Vth (Wind): Thermal speed of the proton in units of km/sec.

Vsw: Solar wind bulk speed in units of km/sec

GSE Vx, Vy, and Vz: Solar wind velocity in units of km/sec, Cartesian GSE coordinate.

WI_K0_MFI: Wind Magnetic Fields Investigation, Key Parameters (~60 sec)

- R. Lepping (NASA/GSFC)

AC_K1_MFI: ACE Magnetic Field 16-Second Key Parameters

- N. Ness (Bartol Research Institute)

|B|: Magnetic field magnitude in units of nT.

GSE B_X, B_Y, and B_Z: magnetic field in units of nT, Cartesian GSE coordinate.

Cone angle: GSE cone angle derived from acos($|B_x|/|B|$) in units of degree.

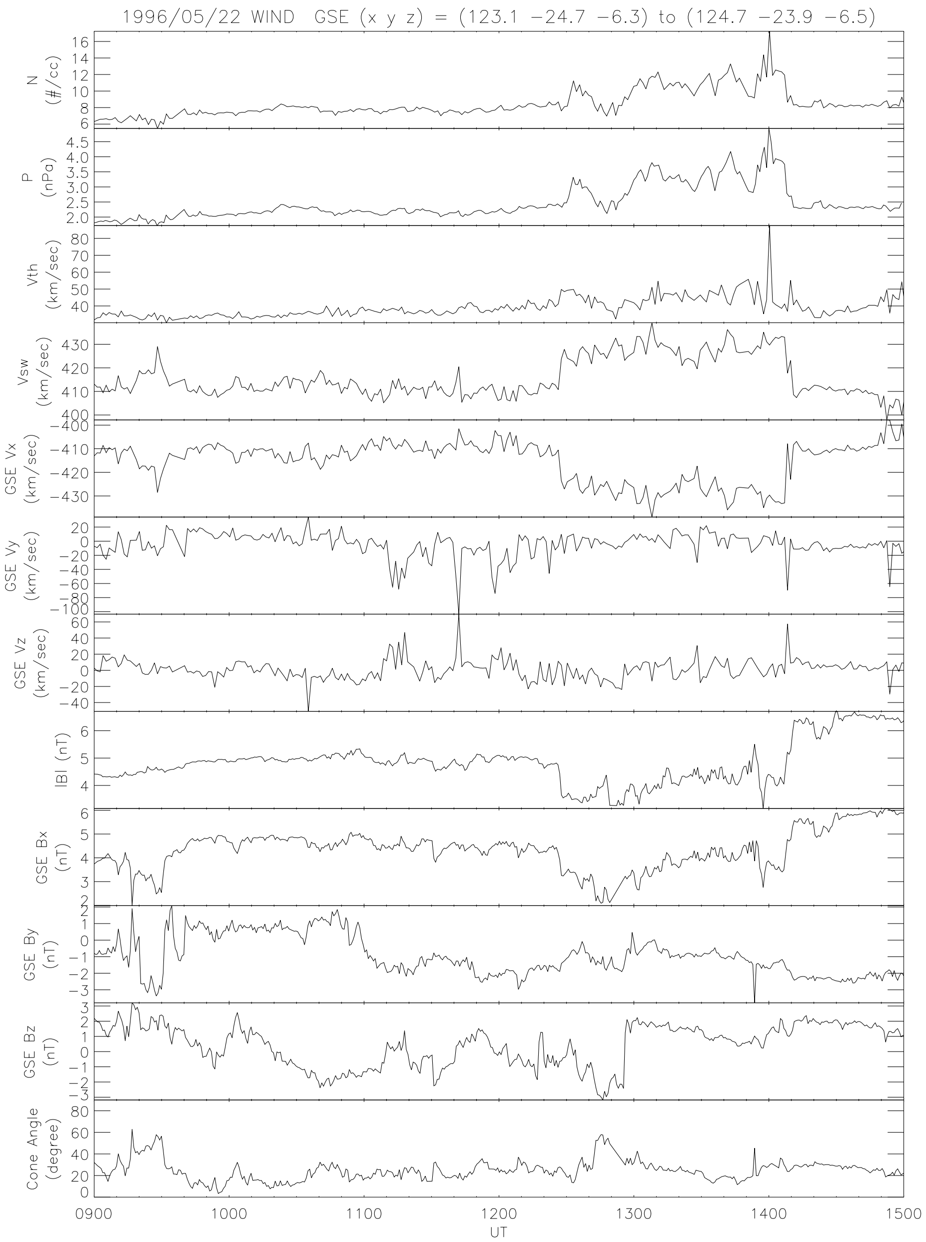
1996/05/22 WIND GSE (x y z) = (123.1 −24.7 −6.3) to (124.7 −23.9 −6.5)
N (#/cc)
P (nPa)
Vth (km/sec)
Vsw (km/sec)
GSE Vx (km/sec)
GSE Vy (km/sec)
GSE Vz (km/sec)
|B| (nT)
GSE Bx (nT)
GSE By (nT)
GSE Bz (nT)
Cone Angle (degree)
0900
1000
1100
1200
1300
1400
1500
UT

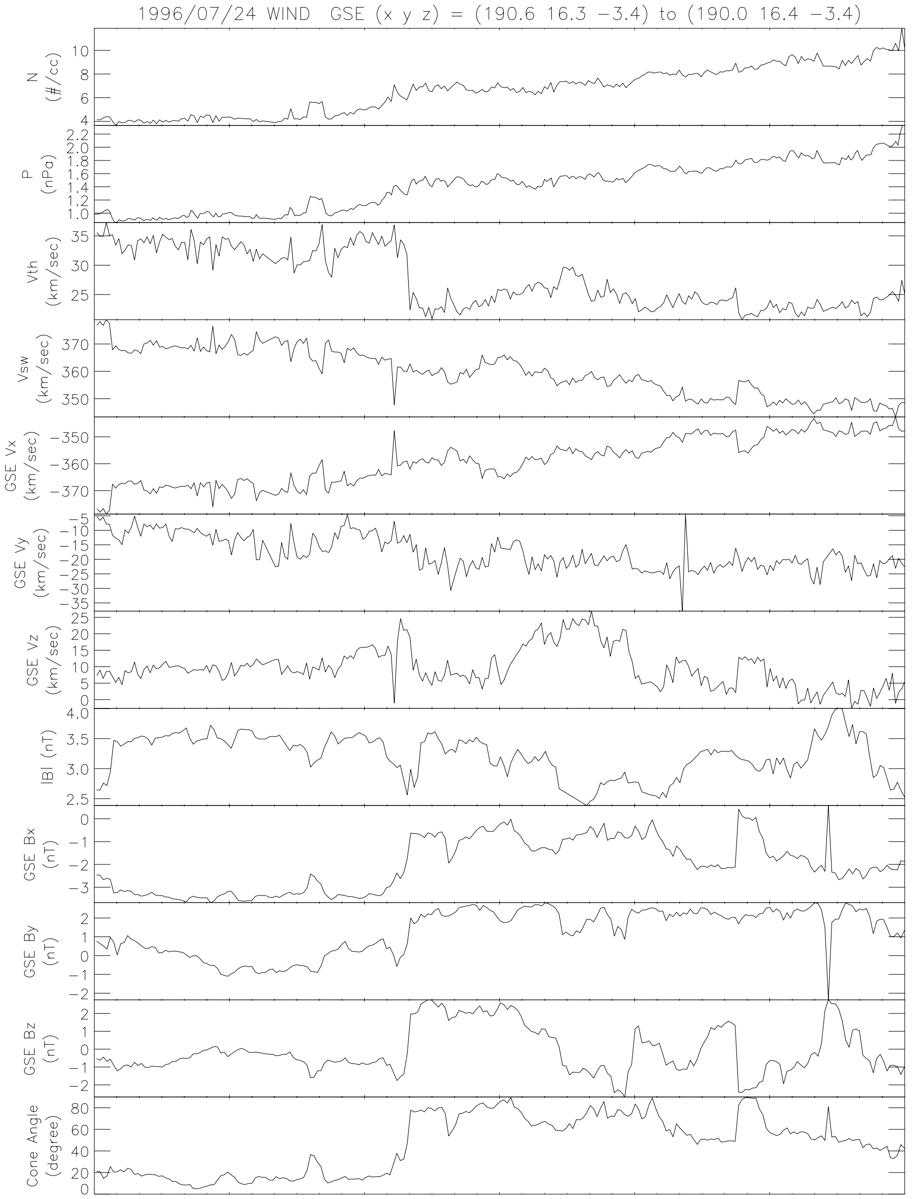
1996/07/24 WIND GSE (x y z) = (190.6 16.3 −3.4) to (190.0 16.4 −3.4)
N (#/cc)
P (nPa)
Vth (km/sec)
Vsw (km/sec)
GSE Vx (km/sec)
GSE Vy (km/sec)
GSE Vz (km/sec)
|B| (nT)
GSE Bx (nT)
GSE By (nT)
GSE Bz (nT)
Cone Angle (degree)
0800
0900
1000
1100
1200
1300
1400
UT

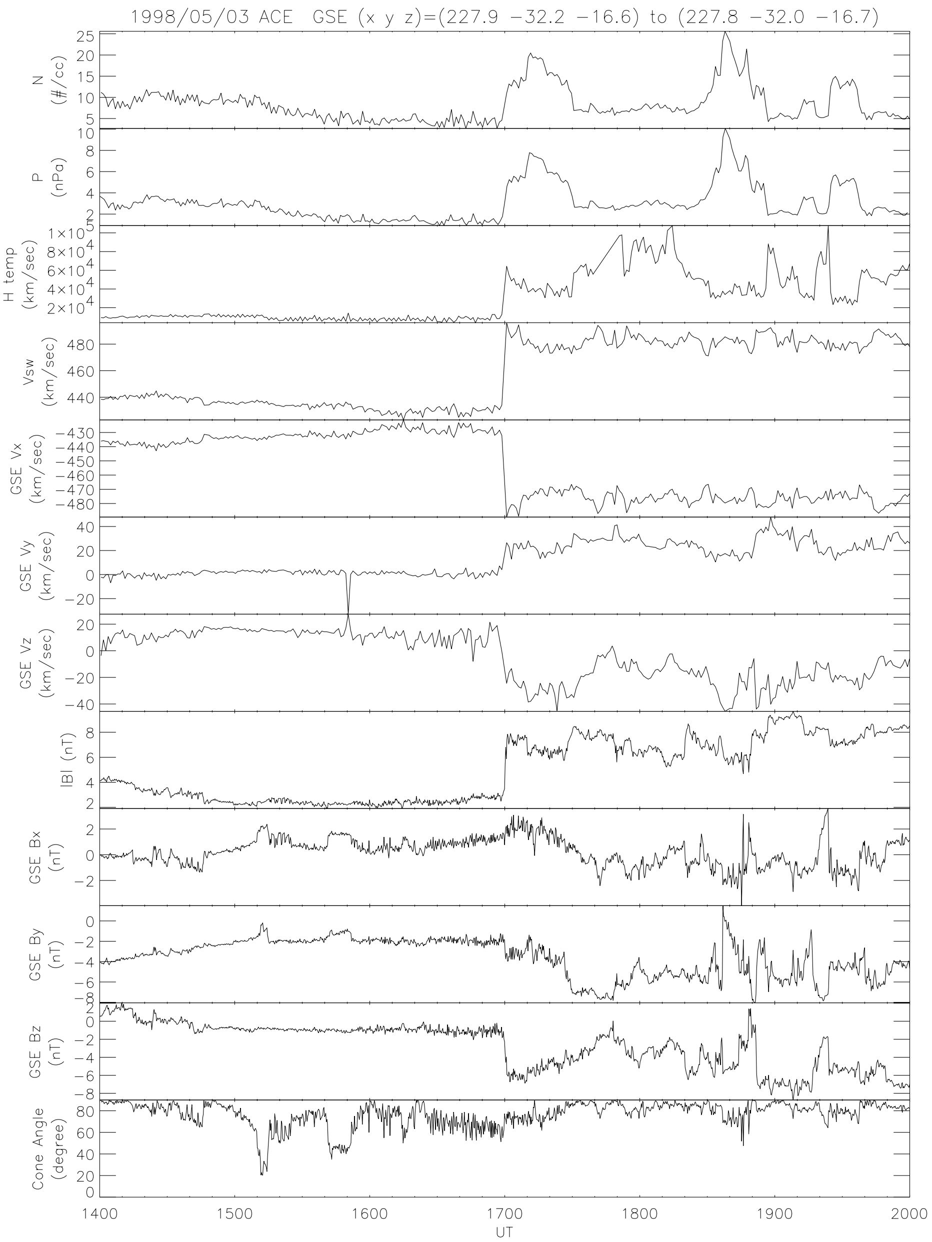

1998/05/03 ACE GSE (x y z)=(227.9 −32.2 −16.6) to (227.8 −32.0 −16.7)
N (#/cc)
P (nPa)
H temp (km/sec)
Vsw (km/sec)
GSE Vx (km/sec)
GSE Vy (km/sec)
GSE Vz (km/sec)
|B| (nT)
GSE Bx (nT)
GSE By (nT)
GSE Bz (nT)
Cone Angle (degree)
UT

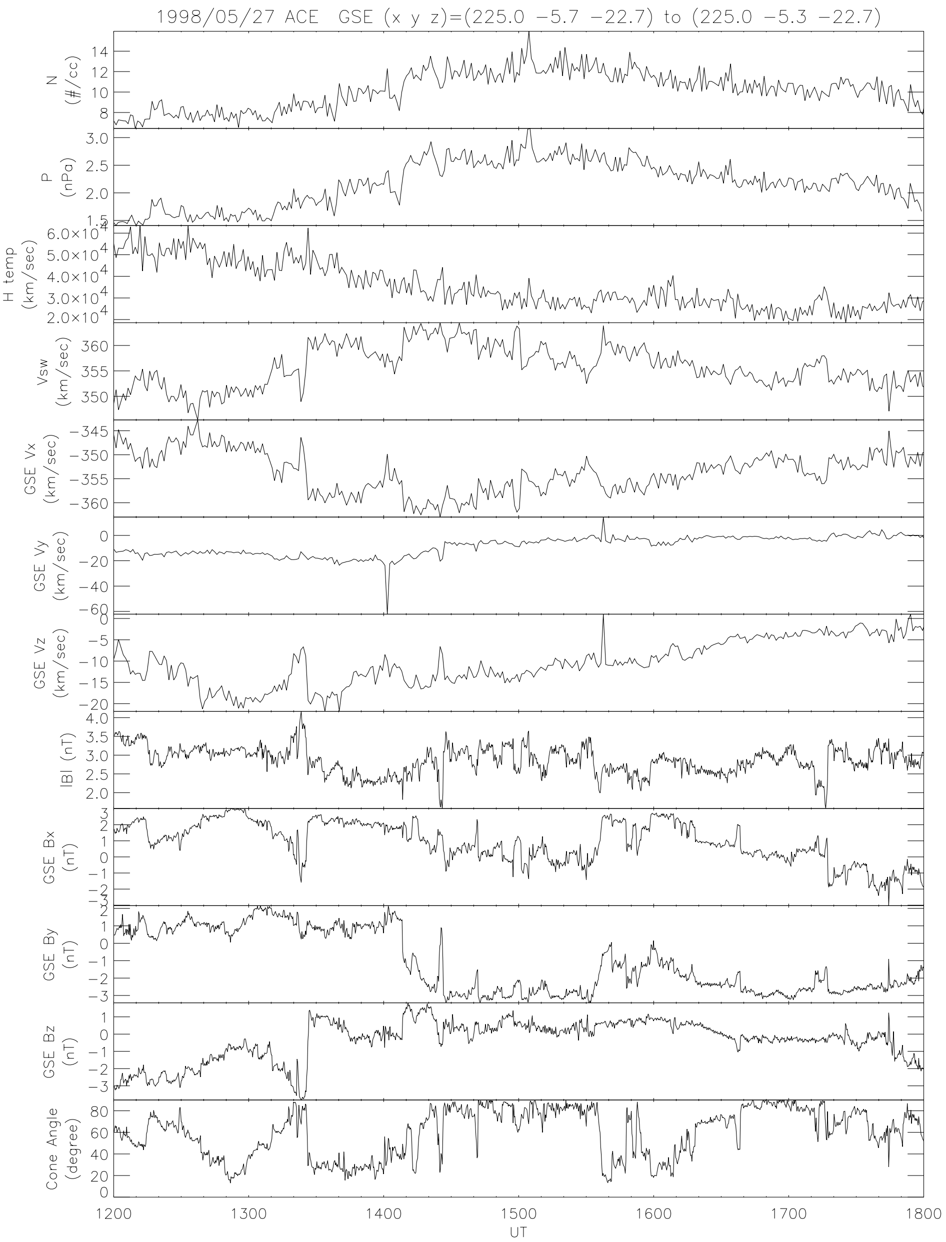
1998/05/27 ACE GSE (x y z)=(225.0 −5.7 −22.7) to (225.0 −5.3 −22.7)
N (#/cc)
P (nPa)
H temp (km/sec)
Vsw (km/sec)
GSE Vx (km/sec)
GSE Vy (km/sec)
GSE Vz (km/sec)
|B| (nT)
GSE Bx (nT)
GSE By (nT)
GSE Bz (nT)
Cone Angle (degree)
UT

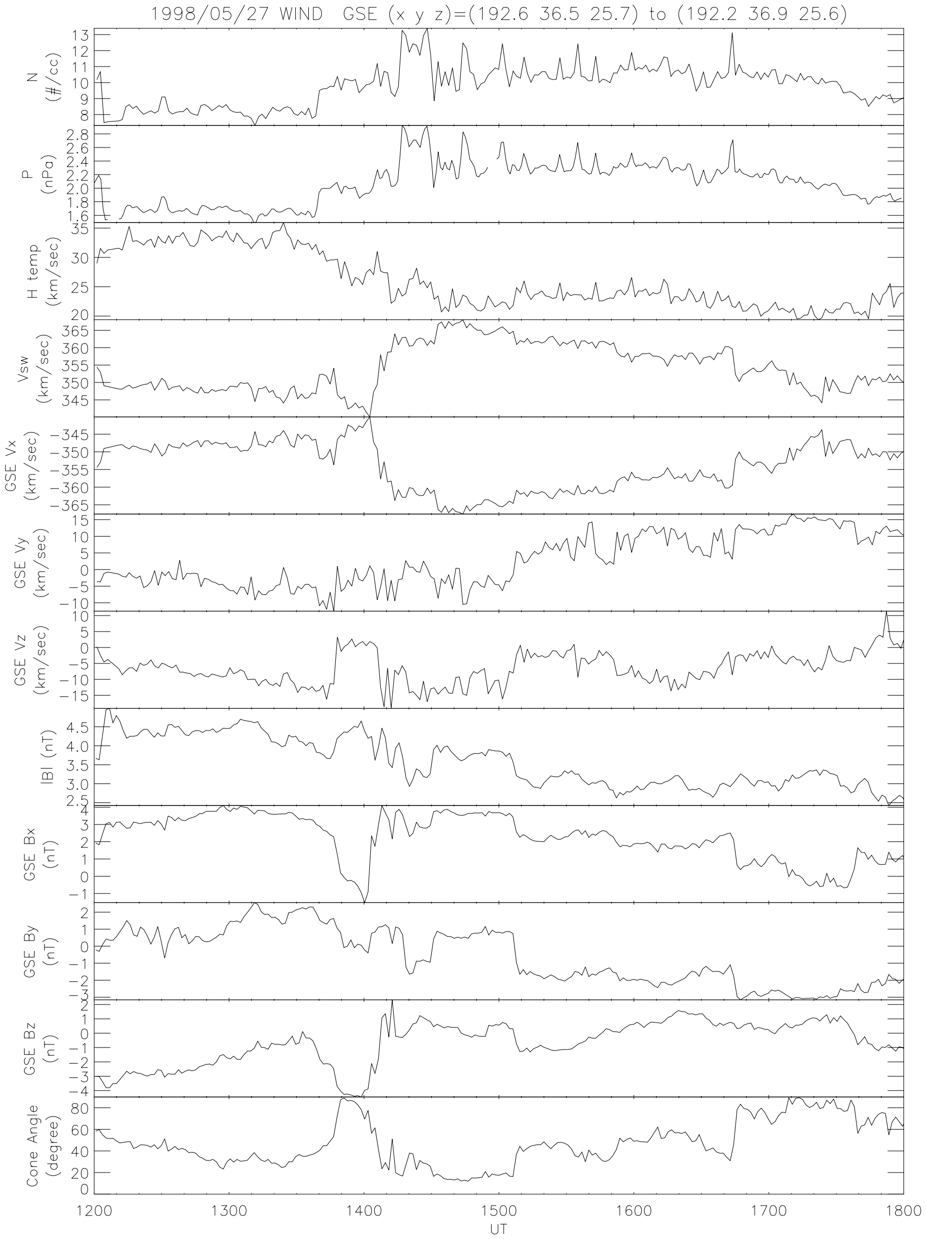
1998/05/27 WIND GSE (x y z)=(192.6 36.5 25.7) to (192.2 36.9 25.6)
N (#/cc)
P (nPa)
H temp (km/sec)
Vsw (km/sec)
GSE Vx (km/sec)
GSE Vy (km/sec)
GSE Vz (km/sec)
|B| (nT)
GSE Bx (nT)
GSE By (nT)
GSE Bz (nT)
Cone Angle (degree)
1200
1300
1400
1500
1600
1700
1800
UT

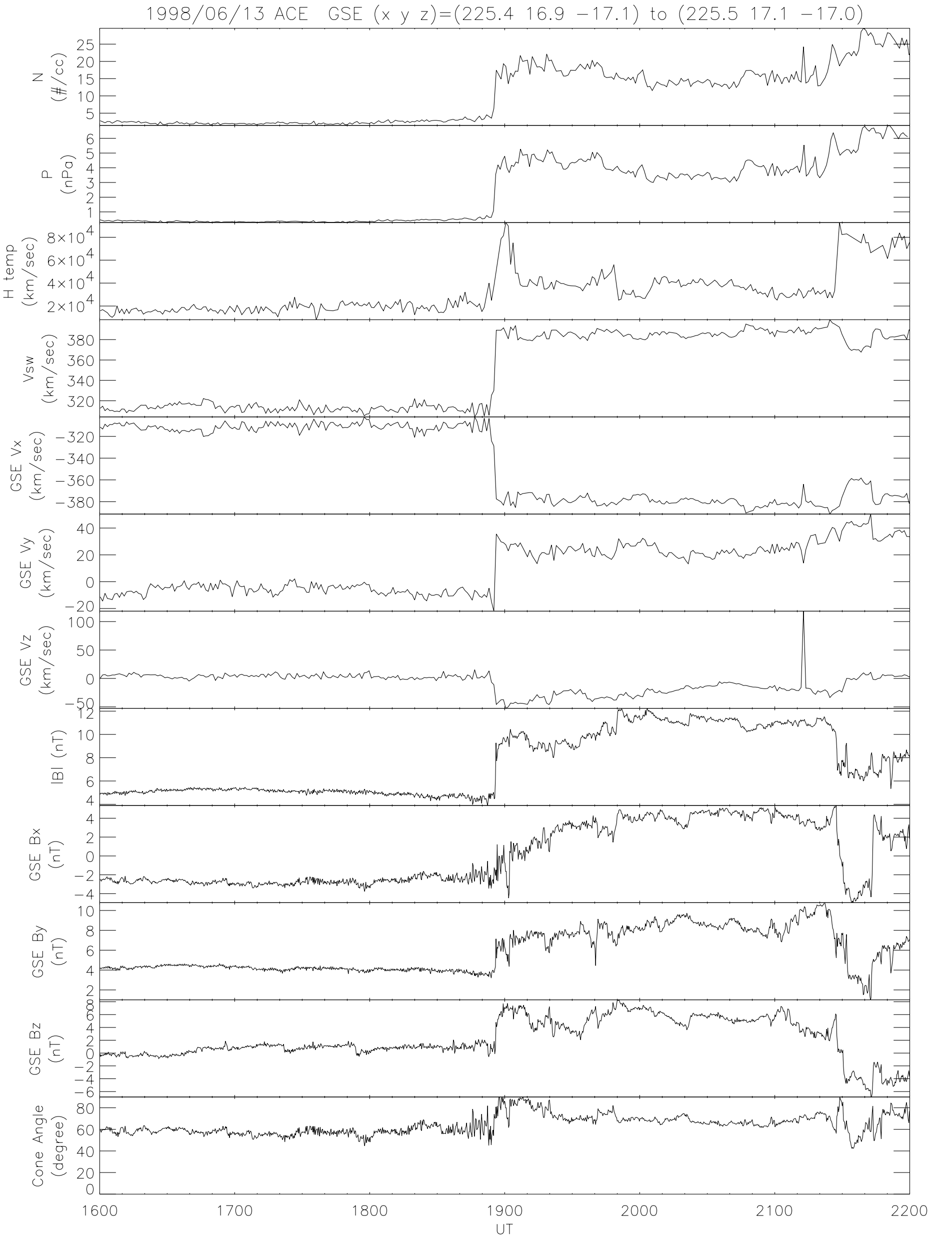

1998/06/13 ACE GSE (x y z)=(225.4 16.9 −17.1) to (225.5 17.1 −17.0)
N (#/cc)
P (nPa)
H temp (km/sec)
Vsw (km/sec)
GSE Vx (km/sec)
GSE Vy (km/sec)
GSE Vz (km/sec)
|B| (nT)
GSE Bx (nT)
GSE By (nT)
GSE Bz (nT)
Cone Angle (degree)
1600 1700 1800 1900 2000 2100 2200
UT

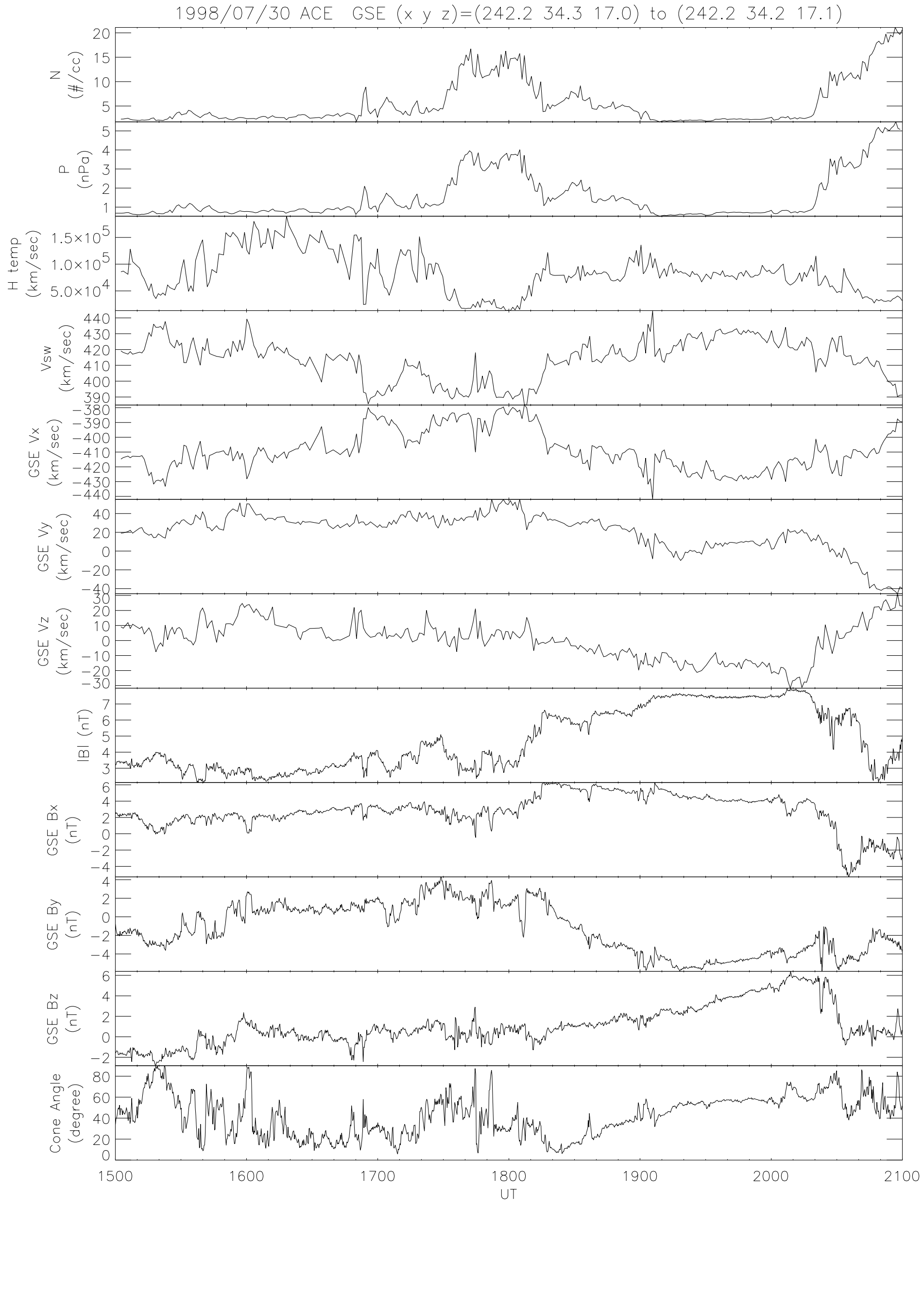
1998/07/30 ACE GSE (x y z)=(242.2 34.3 17.0) to (242.2 34.2 17.1)
N (#/cc)
P (nPa)
H temp (km/sec)
Vsw (km/sec)
GSE Vx (km/sec)
GSE Vy (km/sec)
GSE Vz (km/sec)
|B| (nT)
GSE Bx (nT)
GSE By (nT)
GSE Bz (nT)
Cone Angle (degree)
1500
1600
1700
1800
1900
2000
2100
UT

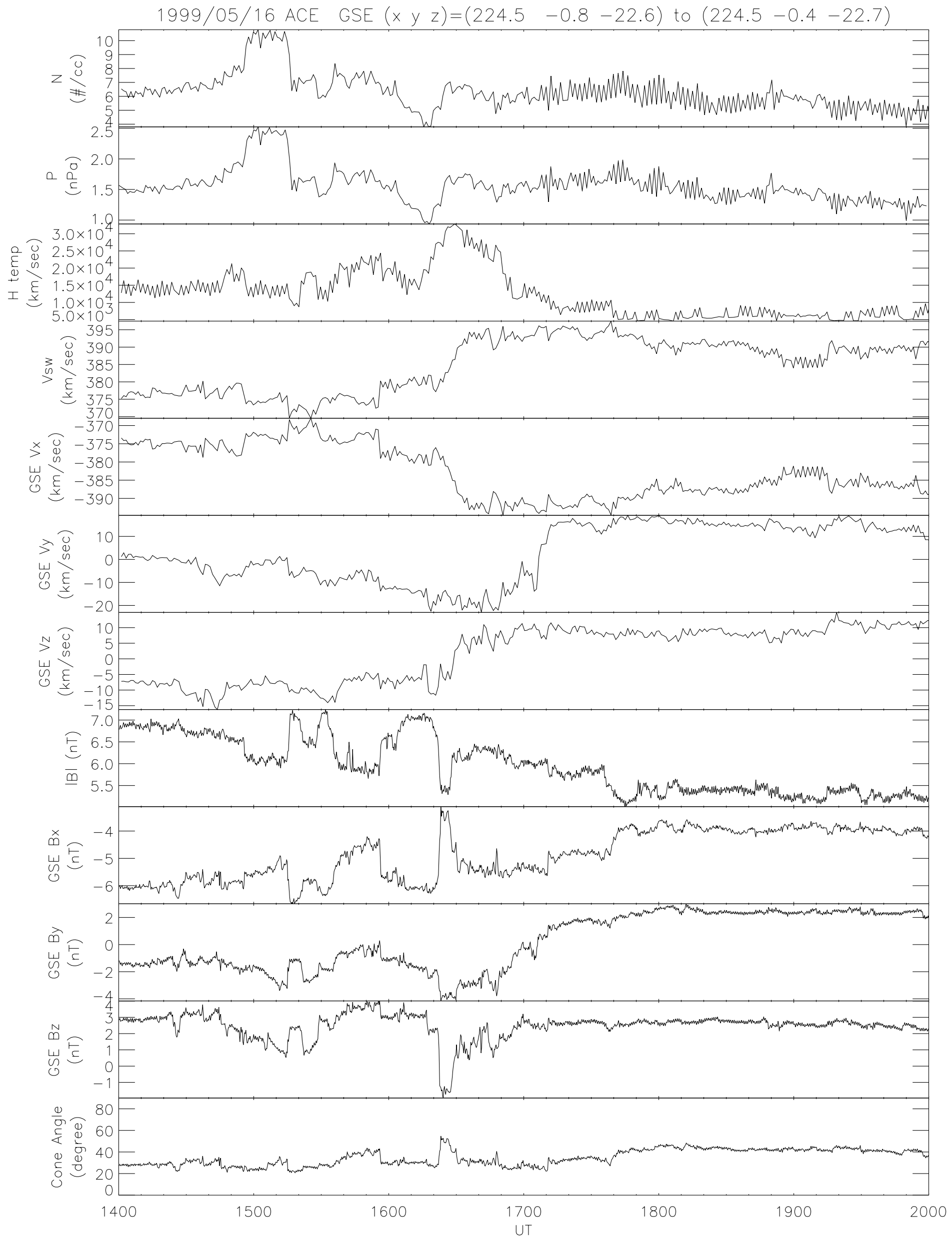
1999/05/16 ACE GSE (x y z)=(224.5 -0.8 -22.6) to (224.5 -0.4 -22.7)
N (#/cc)
P (nPa)
H temp (km/sec)
Vsw (km/sec)
GSE Vx (km/sec)
GSE Vy (km/sec)
GSE Vz (km/sec)
|B| (nT)
GSE Bx (nT)
GSE By (nT)
GSE Bz (nT)
Cone Angle (degree)
1400
1500
1600
1700
1800
1900
2000
UT

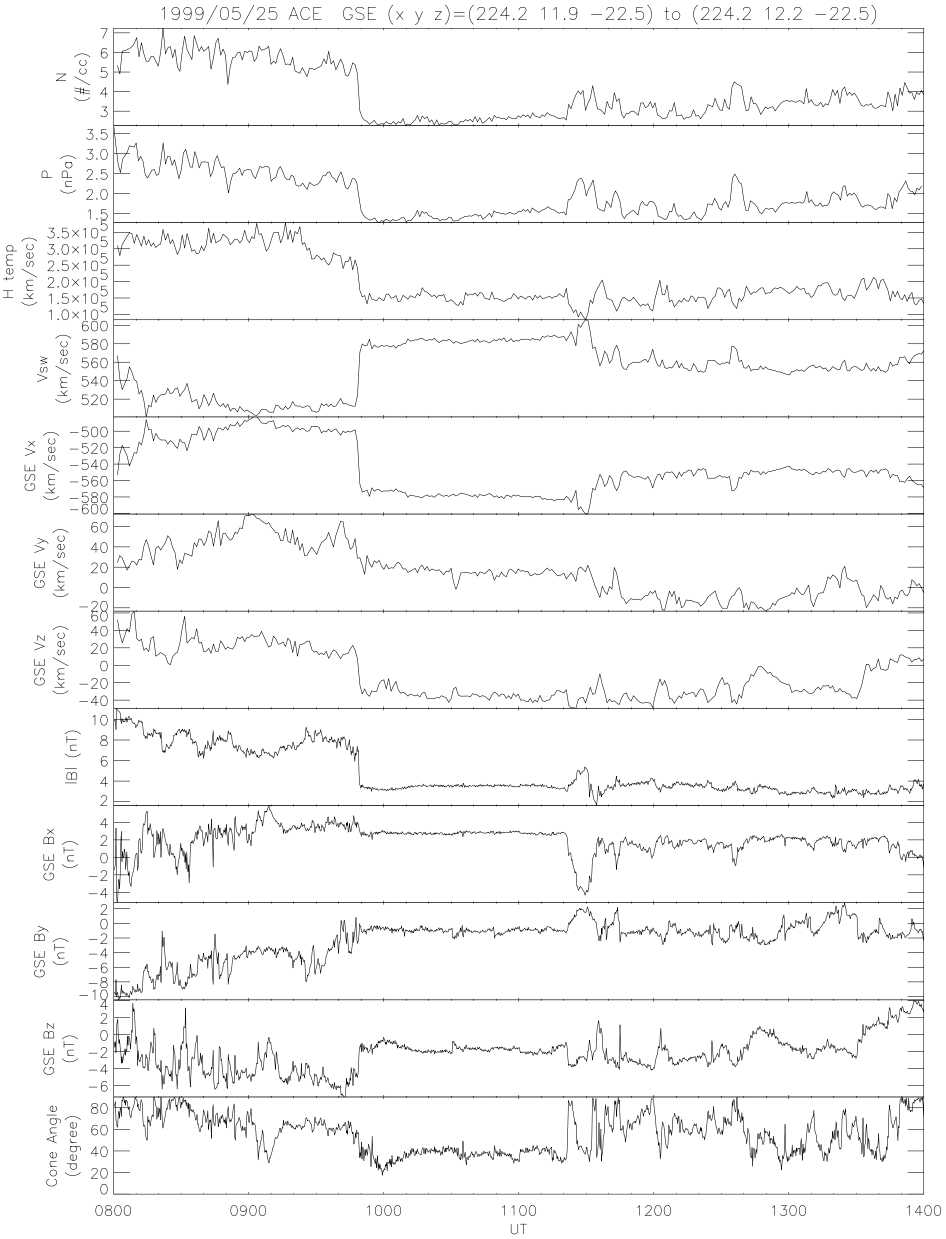

1999/05/25 ACE GSE (x y z)=(224.2 11.9 −22.5) to (224.2 12.2 −22.5)
N (#/cc)
P (nPa)
H temp (km/sec)
Vsw (km/sec)
GSE Vx (km/sec)
GSE Vy (km/sec)
GSE Vz (km/sec)
|B| (nT)
GSE Bx (nT)
GSE By (nT)
GSE Bz (nT)
Cone Angle (degree)
0800
0900
1000
1100
1200
1300
1400
UT

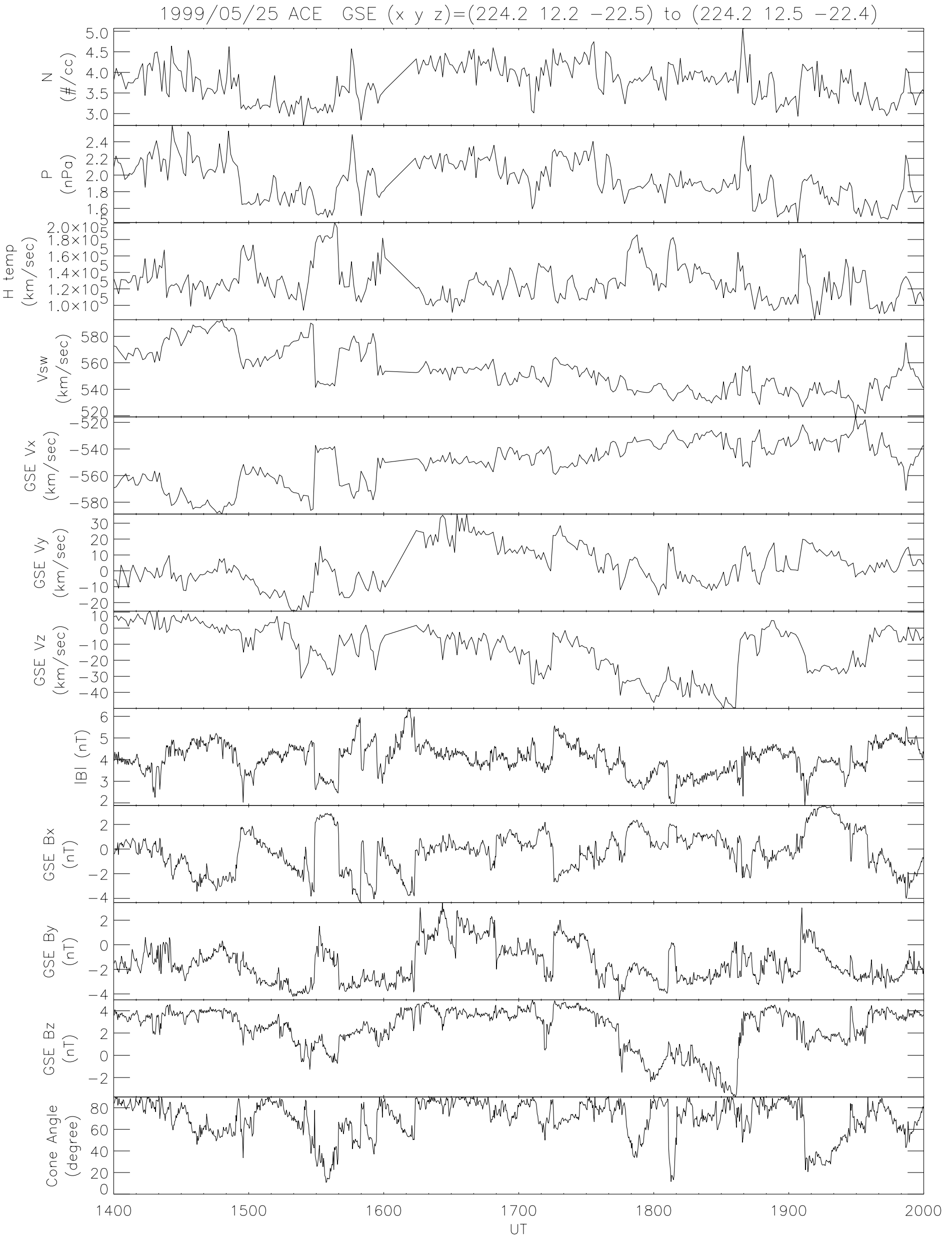
1999/05/25 ACE GSE (x y z)=(224.2 12.2 −22.5) to (224.2 12.5 −22.4)
N (#/cc)
P (nPa)
H temp (km/sec)
Vsw (km/sec)
GSE Vx (km/sec)
GSE Vy (km/sec)
GSE Vz (km/sec)
IBI (nT)
GSE Bx (nT)
GSE By (nT)
GSE Bz (nT)
Cone Angle (degree)
1400
1500
1600
1700
1800
1900
2000
UT

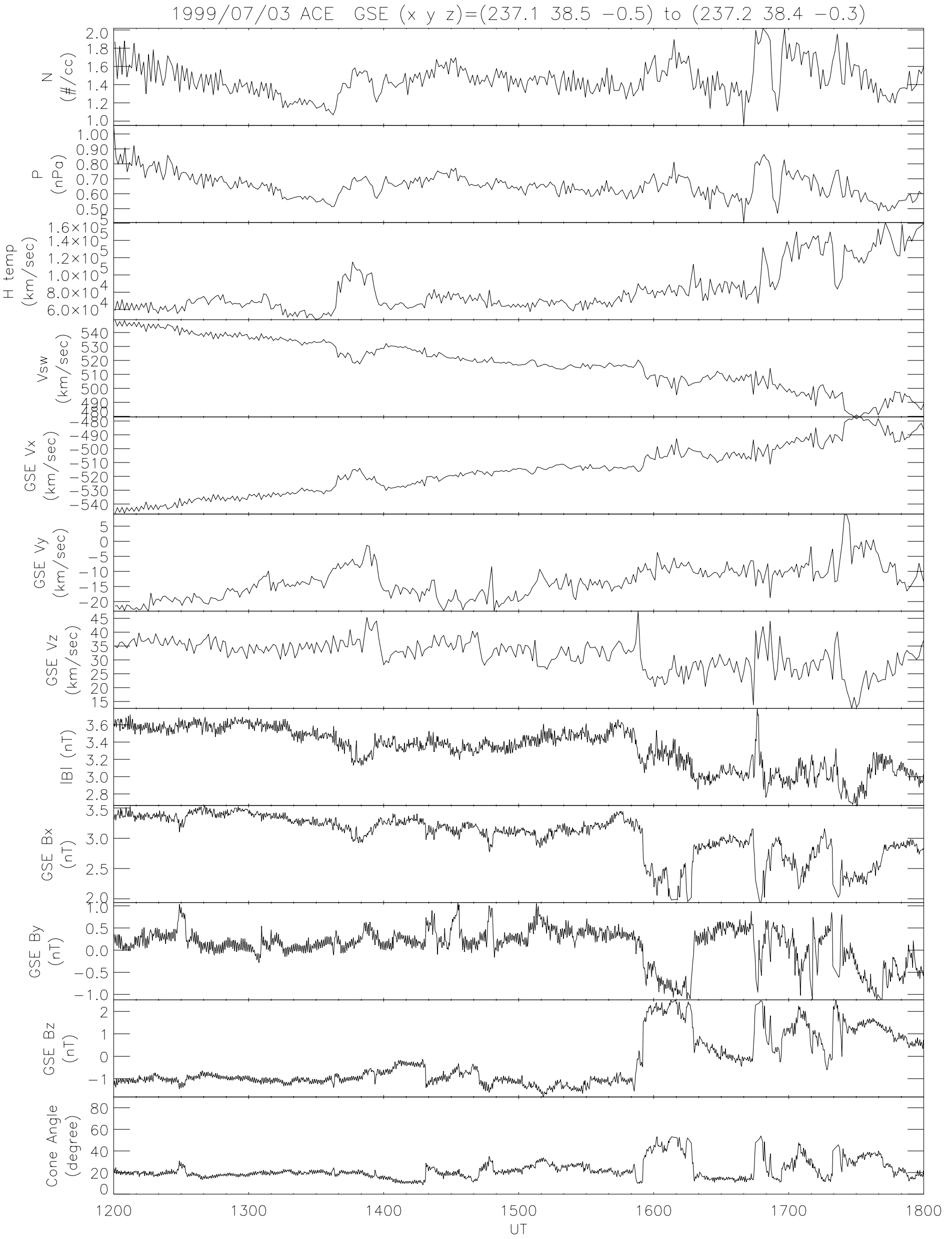

1999/07/03 ACE GSE (x y z)=(237.1 38.5 −0.5) to (237.2 38.4 −0.3)
N (#/cc)
P (nPa)
H temp (km/sec)
Vsw (km/sec)
GSE Vx (km/sec)
GSE Vy (km/sec)
GSE Vz (km/sec)
|B| (nT)
GSE Bx (nT)
GSE By (nT)
GSE Bz (nT)
Cone Angle (degree)
UT

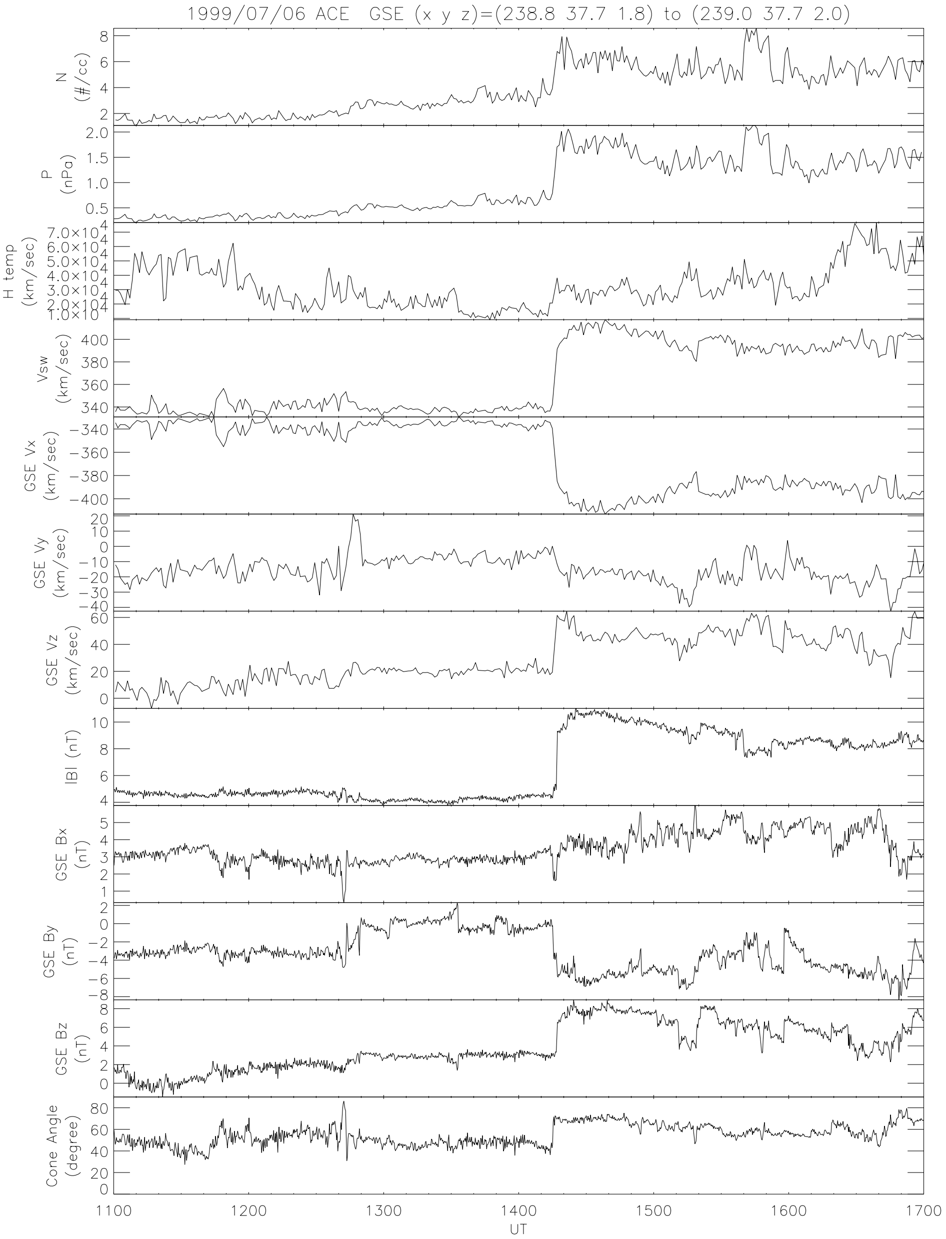
1999/07/06 ACE GSE (x y z)=(238.8 37.7 1.8) to (239.0 37.7 2.0)
N (#/cc)
P (nPa)
H temp (km/sec)
Vsw (km/sec)
GSE Vx (km/sec)
GSE Vy (km/sec)
GSE Vz (km/sec)
|B| (nT)
GSE Bx (nT)
GSE By (nT)
GSE Bz (nT)
Cone Angle (degree)
1100
1200
1300
1400
1500
1600
1700
UT

Bibliography

Araki, T., A physical model of geomagnetic sudden commencement, in Solar Wind Sources of Magnetospheric Ultra-Low-Frequency Waves, *Geophys. Monogr. Ser., vol. 81*, edited by M. J. Engebretson, K. Takahashi, and M. Scholor, pp. 183, AGU, Washington, D. C., 1994.

Bennett, L., M. G. Kivelson, K. K. Khurana, L. A. Frank, W. R. Paterson, A model of the Earth's distant shock, *J. Geophys. Res., 102*, 26927, 1997.

Bering E. A., L. J. Lanzerotti, J. R. Benbrook, Z.-M. Lin, C. G. Maclennan, A. Wolfe, R. E. Lopez, and E. Friis-Christensen, Solar wind properties observed during high-latitude impulsive perturbation events, *Geophys. Res. Lett., 17*, 579, 1990.

Bristow, W. A., D. G. Sibeck, C. Jacquey, R. A. Greenwald, G. J. Sofko, T. Mukai, T. Yamamoto, S. Kokubun, T. J. Hugshes, W. J. Hugshes, and M. J. Engebretson, Observations of convection vortices in the afternoon sector using the SuperDARN HF radars, *J. Geophys. Res., 100*, 19743, 1995.

Cable, S., and Y. Lin, Three-dimensional MHD simulations of interplanetary rotational discontinuities impacting the Earth's bow shock and magnetosheath, *J. Geophys. Res., 103*, 29551, 1998.

Chen, G. X.., Y. Lin, and S. Cable, Generation of traveling convection vortices and field-aligned currents in the magnetosphere by response to an interplanetary tangential discontinuity, *Geophys. Res. Lett., 27*, 3583, 2000.

Cramer, H., On the theory of stationary random processes, *Ann. Math., 41*, 215, 1940.

Dudeney, J. R., R. B. Horne, M. J. Jarvis, R. I. Kressman, A. S. Rodger, and A. J. Smith, British Antarctic Survey's ground-based activities complementary to satellite missions such as Cluster, in *Satellites - Ground Based Coordination Sourcebook*, edited by M. Lockwood, M. N. Wild, and H. J. Opgenooth, European Space Agency Special Publication SP-1198, 101,1997

Dudeney, J. R., R. I. Kresson and A. S. Rodger, Automated observatories for geospace research in polar regions, *Antarctic Science, 10*, 192,1998

Detrick, D. L., and T. J. Rosenberg, A phased-array radiowave imager for studies of cosmic noise absorption, *Radio Sci., 25*, 325, 1990.

Dungey, J. W., Interplanetary magnetic field and the auroral zone, *Phys. Rev. Lett., 6*, 47, 1961.

Eastman, T. E., L. A. Frank, W. K. Peterson, and W. Lennartsson, The plasma sheet boundary layer, *J. Geophys. Res., 89*, 1553, 1984.

Engebretson, M. J., D. J. Murr, W. J. Hugshes, H. Lühr, T. Moretto, J. L. Posch, A. T. Weatherwax, T. J. Rosenberg, C. G. Maclennan, L. J. Lanzerotti, F. Marcucci, S. Dennis, G. Burns, J. Bitterly, and M. Bitterly, A multipoint determination of the propagation velocity of a sudden commencement across the polar ionosphere, *J. Geophys. Res., 104*, 22433, 1999.

Fairfield, D. H., Average and unusual locations of the Earth's magnetopause and bow shock, *J. Geophys. Res., 76*, 6700, 1971.

Farrugia, C. J., M. P. Freeman, S. W. H. Cowley, D. J. Southwood, M. Lockwood, and A. Etemadi, Pressure-driven magnetopause motions and attendant response on the ground, *Planet. Space Sci., 37*, 589, 1989.

Friis-Christensen, E., M. A. McHenry, C. R. Clauer, and S. Vennerstrom, Ionospheric traveling convection vortices observed near the polar cleft: A triggered response to sudden changes in the solar wind, *Geophys. Res. Lett., 15*, 253, 1988.

Fukunishi, H., and L. J. Lanzerotti, Hydromagnetic waves in the dayside cusp region and ground signatures of flux transfer events, *Geophys. Monogr. Ser., Vol 53*, edited by B. Tsurutani and H. Oya, AGU, Washington, 1989.

Fukushima, N., Equivalence in ground geomagnetic effect of Chapman-Vestine's and Birkeland-Alfven's electric current-systems for polar magnetic storms, *Rep. Ionos. Space Res. Jpn. 23(3)*, 219, 1969.

Germany, G. A., M. A. Torr, D. G. Torr, and P. G. Richards, Use of FUV auroral emissions as diagnostic indicators, *J. Geophys. Res., 99*, 383, 1994.

Glassmeier, K.-H., M. Lester, W. A. C. Mier-Jedrzejowicz, C. A. Green, G. Rostoker, D. Orr, U. Wedeken, H. Junginger, and E. Amata, Pc5 pulsations and their possible source mechanisms: A case study, *J. Geophys. Res., 55*, 108, 1984.

Glassmeier, K.-H. M. Hönisch, and J. Untiedt, Ground-based and satellite observations of traveling magnetospheric convection twin vortices, *J. Geophys. Res., 94*, 2520, 1989.

Glassmeier, K.-H., and C. Heppner, Traveling convection twin vortices: Another case study, global characteristics, and a model, *J. Geophys. Res., 97*, 3977, 1992.

Goertz, C. K., E. Nielsen, A. Korth, K. H. Glassmeier, C. Haldoupis, P. Hoeg, and D. Hayward, Observation of a possible ground signature of flux transfer events, *J. Geophys. Res., 90*, 4069, 1985.

Greenstadt, E. W., and J. V. Olson, Pc3, 4 activity and interplanetary field orientation, *J. Geophys. Res., 81*, 5911, 1976.

Greenwald, R. A., K. B. Baker, J. R. Dudeney, M. Pinnock, T. B. Jones, E. C. Thomas, J.-P. Villain, J.-C.,Cerisier, C. Senior, C. Hanuise, R. D. Hunsucker, G. Sofko, J. Koehler, E. Nielsen, R. Pellinen, A. D. M. Walker, N. Sato, and H. Yamagishi, DARN/SuperDARN: a global view of the dynamics of high-latitude convection, *Space Sci. Rev., 71*, 761, 1995.

Gustafsson, G., N. E. Papitashvilli, and V. O. Papitashvili, A revised corrected geomagnetic coordinate system for Epochs 1985 and 1990, *J. Atmos. Terr. Phys., 54*, 1609, 1992.

Hugshes, W. J., and M. J. Engebretson, MACCS: Magnetometer array for cusp and cleft studies, in *Satellite - Ground Based Coordination Sourcebook*, edited by M. Lockwood et al., Eur. Space Agency Spec. Publ., SP-1198, 119, 1997.

Kivelson, M. G., and D. J. Southwood, Ionospheric traveling vortex generation by solar wind buffering of the magnetosphere, *J. Geophys. Res., 96*, 1661, 1991.

Konik, R. M., L. J. Lanzerotti, A. Wolfe, C. G. Maclennan, and D. Venkatesan, Cusp latitude magnetic impulse events, 2. Interplanetary magnetic field and solar wind conditions, *J. Geophys. Res., 99*, 14831, 1994.

Konik, R. M., L. J. Lanzerotti, C. G. Maclennan, A. Wolfe, and D. Venkatesan, Cusp latitude magnetic impulse events, 3. Associated low-latitude signatures, *J. Geophys. Res., 100*, 7731, 1995.

Korotova, G. I., and D. G. Sibeck, A case study of transient event motion in the magnetosphere and ionosphere, *J. Geophys. Res., 100*, 35, 1995.

Korotova, G. I., D. G. Sibeck, T. J. Rosenberg, C. T. Russell, and E. Friis-Christensen, High-latitude ionospheric transient events in a global context, *J. Geophys. Res., 102*, 17499, 1997.

Korotova, G. I., D. G. Sibeck, T. Moretto, and G. D. Reeves, Tracking transient events through geosinchronous orbit, *J. Geophys. Res., 104*, 10265, 1999.

Lanzerotti, L. J., L. C. Lee, C. G. Maclennan, A. Wolfe, and L. V. Medford, Possible evidence of flux transfer events in the polar ionosphere, *Geophys. Res. Lett., 13*, 1089, 1986.

Lanzerotti, L. J., R. D. Hunsucker, D. Rice, L. C. Lee, A. Wolfe , C. G. Maclennan, and L. V. Medford, Ionosphere and Ground-Based Response to Field-Aligned Currents Near the Magnetospheric Cusp Regions, *J. Geophys. Res., 92*, 7739, 1987.

Lanzerotti, L. J., Conjugate spacecraft and ground-based studies of hydromagnetic phenomenon near the magnetopause, *Adv. Space Res., 8*, 301, 1988.

Lanzerotti, L. J., A. Wolfe, and N. Trivedi, Magnetic impulse events at high latitudes: Magnetopause and boundary layer plasma processes, *J. Geophys. Res., 95*, 97, 1990.

Lanzerotti, L. J., R. M. Konik, and A. Wolfe, Cusp latitude magnetopause events, 1. Occurrence statistics, *J. Geophys. Res., 96*, 14009, 1991.

Le, G., C. T. Russel, and H. Kuo, Flux transfer events: spontaneous or driven?, *Geophys. Res. Lett., 20*, 791, 1993.

Lee, L. C., and Z. F. Fu, A theory of magnetic flux transfer at the earth's magnetopause, *Geophys. Res. Lett., 12*, 105, 1985.

Lemaire, J., Impulsive penetration of filamentary plasma elements into the magnetosphere of the Earth's and Jupiter, *Planet. Space Sci., 25*, 887, 1977.

Lin, Z. M., E. A. Bering, J. R. Benbrook, B. Liao, L. J. Lanzeroti, C. G. Maclennan, A. N. Wolfe, and E. Friis-Christensen, Statistical studies of impulsive events at high latitudes, *J. Geophys. Res., 100*, 7553, 1995.

Lin, Y., L. C., Lee, and M. Yan, Generation of dynamic pressure pulses downstream of the bow shock by variations in the interplanetary magnetic field orientation, *J. Geophys. Res., 101*, 479, 1996.

Lin, Y., Generation of anomalous flows near the bow shock by its interaction with interplanetary discontinuities, *J. Geophys. Res., 102*, 24265, 1997.

Lockwood, M., M. F. Smith, C. J. Farrugia, and G. L. Siscoe, Ionospheric ion upwelling in the wake of flux transfer events at the dayside magnetopause, *J. Geophys. Res., 92*, 231, 1987.

Lockwood, M., P. E. Sandholt, S. W. H. Cowley, and T. Oguti, Interplanetary magnetic field control of dayside auroral activity and the transfer of momentum across the dayside magnetopause, *Planet. Space Sci., 37*, 1347, 1989.

Lühr, H., and W. Blawert, Ground signatures of traveling convection vortices, in Solar Wind Sources of Magnetospheric Ultra-Low Frequency Waves, *Geophys. Monogr. Ser., vol 81*, edited by M. J. Engebretson, K. Takahashi, and M. Scholer, p. 231, AGU, Washington, D. C., 1994.

Lühr, H., M. Lockwood, P. E. Sandholt, T. L. Hansen, and T. Moretto, Multi-instrument Ground-based Observations of a Traveling Convection Vortices Event, *Ann. Geophys., 14*, 162, 1996.

Lühr, H., M. Rother, T. Iemori, T. L. Hansen, and R. P. Lepping, Superposed epoch analysis applied to large-amplitude traveling vortices, *Ann. Geophys., 16*, 743, 1998.

Lyatsky W. B., and D. G. Sibeck, Central plasma sheet disruption and the formation of dayside poleward moving auroral events, *J. Geophys. Res., 102*, 17625, 1997.

Lyatsky W. B., and D. G. Sibeck, Surface waves on the low latitude boundary layer inner edge and traveling convection vortices, *J. Geophys. Res., 102*, 17643, 1997.

Lyatsky, W. B. G. J. Sofko, A. V. Kustov, D. André, W. J. Hugshes, and D. Murr, Traveling convection vortices as seen by the SuperDARN HF radars, *J. Geophys. Res., 104*, 2591, 1999.

McHenry, M. A., and R. C. Clauer, Modeled ground magnetic signatures of flux transfer events, *J. Geophys. Res., 92*, 11231, 1987.

McHenry, M. A., R. C. Clauer, and E. Friis-Christensen, and J. D. Kelly, Observations of ionospheric convection vortices: Signatures of momentum transfer, *Adv. Space Res., 8(9-10)*, 315, 1988.

McHenry, M. A., R. C. Clauer, and E. Friis-Christensen, P. T. Newell, and J. D. Kelly, Ground observations of magnetospheric boundary layer phenomena, *J. Geophys. Res., 95*, 14995, 1990.

McHenry, M. A., R. C. Clauer, and E. Friis-Christensen, Relationship of solar wind parameters to continuous, dayside, high latitude traveling convection vortices, *J. Geophys. Res., 95*, 15007, 1990.

Mende, S. B., R. L. Rairden, L. J. Lanzerotti, and C. G. Maclennan, Magnetic impulse events and associated optical signatures in the dayside aurora, *Geophys. Res. Lett., 17*, 131, 1990.

Moretto, T., E. Friis-Christensen, H. Luhr, and E. Zesta, Global perspective of ionospheric traveling convection vortices: Case studies of two GEM events, *J. Geophys. Res., 102*, 11597, 1997.

Moretto, T. A. J. Ridley, M. J. Engebretson, and O. Rasmussen, High-latitude ionospheric response to a sudden impulse event during northward IMF conditions, *J. Geophys. Res., 105*, 2521, 2000.

Newell, P. T., and C.-I. Meng, Mapping the dayside ionosphere to the magnetoshpere according to particle precipitation characteristics, *Geophys. Res.Lett., 19*, 609, 1992.

Paschmann, G., G. Haerendel, N. Sckopke, E. Möbius, H. Lühr, and C. W. Carlson, Three-dimensional plasma structures with anomalous flow directions near the Earth's bow shock, *J. Geophys. Res., 93*, 11279, 1988.

Pinnock, M., Rodger, A. S., Dudeney, J. R., Greenwald, R. A., and Baker, K. B., An ionospheric signature of possible enhanced magnetic field merging on the dayside magnetopause, *J. Atmos. Terr. Phys., 53*, 201, 1991.

Potemra, T. A., L. J. Zanetti, K. Takahashi, R. E. Erlandson, H. Luhr, G. T. Marklund, L. P. Block, L. G. Blomberg, and R. P. Lepping, Multi-satellite and ground-based observations of transient ULF waves, *J. Geophys. Res., 94*, 2543, 1989.

Predo, M., J. A. Slavin, E. Mazurm, and S. A. Curtis, Three-dimensional position and shape of the bow shock and their variation with Alfvénic, sonic and magnetosonic Mach numbers and interplanetary magnetic field orientation, *J. Geophys. Res., 100*, 7907, 1995.

Ridley, A. J, T. Moretto, P. Ernström, C. R. Clauer, Global analysis of three traveling vortex events during the November 1993 storm using the assimilative mapping of ionospheric electrodynamics technique, *J. Geophys. Res., 103*, 26349 1998.

Roelof, E. C., and D. G. Sibeck, Magnetopause shape as a Bivarate function of interplanetary magnetic field B_Z and solar wind dynamic pressure, *J. Geophys. Res., 98*, 21421, 1993.

Rosenberg, T. J., and J. A. Doolittle, Studying the polar ionosphere and the magnetopause with automatic geophysical observatories: *The U. S. program in Antarctica*, Antarctic J. U. S., 29(5), 347, 1994.

Rosenberg, T. J., Polar experiment network for geophysical upper-atmosphere investigations (PENGUIn). Project description, in *Proposal to the National Science Foundation*, 1995.

Russel, C. T., and R. C. Elphic, Initial ISEE magnetometer results: Magnetopause observations, *Space Sci. Rev., 22*, 681, 1978.

Sandholt, P. E., M. Lockwood, T. Oguti, S. W. H. Cowley, K. S. C. Freeman, B. Lybekk, A. Egeland, and D. M. Willis, Midday auroral breakup events and related energy and momentum transfer from the magnetosheath, *J. Geophys. Res., 95*, 1039, 1990.

Sato, M., H. Fukunishi, L. J. Lanzerotti, and C. G. Maclennan, Magnetic impulse events and related Pc1 bursts observed by the Automatic Geophysical observatories network in Antarctica, *J. Geophys. Res., 104*, 19971, 1999.

Saunders, M. A., C. T. Russell, and N. Sckopke, Flux transfer events - Scale size and interior structure, *Geophys. Res. Lett., 11*, 131, 1984.

Schunk, R. W., L. Zhu, and J. J. Sojka, Ionospheric response to traveling convection vortices, *Geophys. Res. Lett., 21*, 1759,1994.

Schwartz, S. J., and D. Burgess, Quasi-parallel shocks: A patchwork of three-dimensional structures, *Geophys. Res. Lett., 18*, 373, 1991.

Shiokawa K., K. Yumoto, K. Hayashi, T. Oguti, D. J. McEwen, A statistical study of the motions of auroral arcs in high-latitude morning sector, J. *Geophys. Res.,100*, 21979, 1995.

Shiokawa K., K. Yumoto, N. Nishitani, K. Hayashi, T. Oguti, D. J. McEwen, Y. Kiyama, F. J. Rich, and T. Mukai, Quasi-periodic poleward motions of Sun-aligned auroral arcs in the high-latituide morning sector: A case study, J. *Geophys. Res.,101*, 19789, 1996.

Shiokawa K., K. Yumoto, N. Nishitani, K. Hayashi, T. Oguti, D. J. McEwen, Y. Kiyama, F. J. Rich, and T. Mukai, Quasi-periodic poleward motions of Sun-aligned auroral arcs in the high-latituide morning sector: A multi event study, J. *Geophys. Res.,102*, 24325, 1997.

Shu, J.-H., J. K. Chao, H. C. Hu, C. T. Russel, P. Song, K. K. Khurana, and H. J. Singer, A new functional form to study the solar wind control of the magnetopause size and shape, *J. Geophys. Res., 102*, 9497, 1997.

Shu, J.-H., P. Song, C. T. Russel, J. T. Steinberg, J. K. Chao, G.Zastenker, O. L. Vaisberg, S. Kokubun, H. J. Singer, T. R. Detman, and H. Kawano, Magnetopause location under extreme solar wind conditions, *J. Geophys. Res., 103*, 17691, 1998.

Sibeck, D. G., A model for the transient magnetospheric response to sudden solar wind dynamic pressure variations, *J. Geophys. Res., 95*, 3755, 1990.

Sibeck, D. G., Transient events in the outer magnetospher: Boundary waves or flux transfer events?, *J. Geophys. Res., 97*, 4009, 1992.

Sibeck, D. G., Transient magnetic field signatures at high latitude, *J. Geophys. Res., 98*, 4009, 1993.

Sibeck, D. G., and D. J. Croley, Jr., Solar wind dynamic pressure variations and possible ground signatures of flux transfer events, *J. Geophys. Res., 96*, 1669, 1991.

Sibeck, D. G., and G. I. Korotova, Occurrence patterns for transient magnetic field signatures at high latitudes, *J. Geophys. Res., 101*, 13413, 1996.

Sibeck, D. G., N. L. Borodkova, S. J. Schwartz, C. J. Owen, R. Kessel, S. Kokubun, R. P. Lepping, R. Lin, K. Liou, H. Luhr, R. W. McEntire, C.-I. Meng, T. Mukai, Z. Nemecek, G. Parks, T. D. Phan, S. A. Romanov, J. Safrankova, J.-A. Sauvaud, H. J. Singer, S. I. Solovyev, A. Szabo, K. Takahashi, D. J. Williams, K. Yumoto, and G. N. Zastenker, Comprehensive study of the magnetospheric response to a hot flow anomaly, *J. Geophys. Res.,104*, 4577, 1999.

Sitar, R. J., J. B. Baker, C. R. Clauer, A. J. Ridley, J.A. Cumnock, V. O. Papitashvili, J. Spann, M. J. Brittnacher, and G. K. Parks, Multi-instrument analysis of the ionsosphric signatures of a hot flow anomaly occuring on June 24, 1996, *J. Geophys. Res.,103*, 23357, 1998.

Sitar R. J., and C. R. Clauer, Ground response to sudden changes in the interplanetary magnetic filed orientation, *J. Geophys. Res.,104,* 28343, 1999.

Slepian, D., Prolate spheroidal wave functions, Fourier analysis, and uncertainty-5: The discrete case, *Bell Syst. Tech. J., 57*, 1371, 1978.

Slinker, S. P., J. A. Fedder, W. J. Hugshes, J. G. Lyon, Response of the ionosphere to a density pulse in the solar wind: simulation of traveling convection vortices, *Geophys. Res. Lett., 26*, 3549, 1999.

Sonnerup, B. U. O., and L. J. Curhill Jr., Magnetopause structure and attitude from Explorer 12 observations, *J. Geophys. Res.,72,* 171, 1967.

Sonnerup, B. U. O., and L. J. Curhill Jr., Explorer 12 observations of magnetopause current layer, *J. Geophys. Res.,73,* 1757, 1968.

Southwood, D. J., The hydrodynamic stability of the magnetospheric boundary, *Planet. Space Sci., 16*, 587, 1968.

Southwood, D. J., Theoretical aspects of ionosphere-magnetosphere-solar wind coupling, in Physics of the Ionosphere-Magnetosphere, *Adv. Space Res., 5*, 4, 1985.

Southwood, D. J., The ionospheric signature of flux transfer events, *J. Geophys. Res., 92*, 3207, 1987.

Spreiter, J. R., S. S. Stahara, A new predictive model for determining solar wind-terrestrial planet interactions, *J. Geophys. Res., 85*, 6769, 1980.

Stauning, P., Absorption of cosmic noise in the E-region during electron heating events. A new class of riometer absorption events, *Geophys. Res. Lett., 11*, 1184, 1984.

Strickland, D. J., R. E. Daniel Jr., J. R. Jasperse, and B. Basu, Transport-theoretic model for the electron-proton-hydrogen atom aurora, *J. Geophys. Res., 98*, 21533, 1993.

Takeuchi, T., T. Araki, R. P. Lepping, T. Yamamoto, S. Kokubun, T. Nagai, and T. Iyemori, A magnetic cloud with unusual structure and corresponding bow shock movement observed on May 13, 1995.

Takeuchi, T., T. Araki, H. Lühr, O. Rasmussen, J. Watermann, D. K. Milling, I. R. Mann, K. Yumoto, K. Shiokawa, and T. Nagai, Geomagnetic negative sudden impulse due to a magnetic cloud observed on May 13, 1995, *J. Geophys. Res., 105*, 18835, 2000.

Tamao, T., A Hydromagnetic Interpretation of Geomagnetic SSC*, Rep. Ionos. *Space Res. Jpn., 18*, 16-24, 1964.

Thomson, D. J., Spectrum estimation and harmonic analysis, *Proc. IEEE, 70*, 1055, 1982.

Tsyganenko, N. A., and D. P. Stern, Modeling the Global Magnetic Field of the Large-Scale Birkeland Current Systems, *J. Geophys. Res., 101*, 27187, 1996.

Uberoi, C., L. J. Lanzerotti, and A. Wolfe, Surface waves and magnetic reconnection at a magnetopause, *J. Geophys. Res., 101*, 24979, 1996.

Uberoi, C., and E. G. Zweibel, Alfven resonances and forced reconnection, *J. Plasma Phys., 62*, 345, 1999.

Uberoi, C., L. J. Lanzerotti, and C. G. Maclennan, Remarks on the intrinsic timescale for reconnection on the dayside magnetopause, *J. Geophys. Res., 104*, 25153, 1999.

Valladares, C. E., D. Alcayde, J. A. Rodriguez, J. M. Ruohoniemi, A. P. Van Eyken, Observations of plasma density structures in assosiation with the passage of traveling convection vortices and the occurrence of large plasma jets, *Ann. Geophysicae, 17*, 1020, 1999.

Vorobyev, V. G., V. L. Zverev, and G. V. Starkov, Geomagnetic impulses in the daytime high latitude region: Main morphological characteristics and association with the dynamics of the daytime aurora, *Geomagn. Aeronomy, Engl. Trans., 33*, 621, 1994.

Vorobjev, V. G., O. I. Yagodkina, and V. L. Zverev, Morphological features of bipolar magnetic impulse events and associated interplanetary medium signatures, *J. Geophys. Res., 104*, 4595, 1999.

Weatherwax, A. T., H. B. Vo, T. J. Rosenberg, S. B. Mende, H. U. Frey, L. J. Lanzerotti, and C. G. Maclennan, A dayside ionospheric absorption perturbation in response to a large deformation of the magnetopause, *Geophys. Res. Lett. 26*, 517, 1999.

Woch J., and R. Lundin, Signatures of transient boundary layer processes observed with Viking, *J. Geophys. Res., 97*, 1431, 1992.

Zesta, E., W. J. Hugshes, M. J. Engebretson, T. J. Hugshes, A. L. Lazarus, and K. I. Paularena, The November 9, 1993, traveling convection vortex event: A case study, *J. Geophys. Res., 104*, 28041,1999.

Zhu, L., R. W. Shunk, and J. J. Sojka, Effects of magnetospheric precipitation and ionospheric conductivity on the ground magnetic signatures of traveling convection vortices, *J. Geophys. Res., 104*, 6773,1999.